PROCEEDINGS

OF INTERNATIONAL CONFERENCE ON COMMUNICATIONS, ELECTROMAGNETICS AND MEDICAL APPLICATIONS (CEMA'08)

Organized by:

FACULTY OF TELECOMMUNICATIONS
TECHNICAL UNIVERSITY OF SOFIA, BULGARIA

NATIONAL TECHNICAL UNIVERSITY OF ATHENS, GREECE,
SCHOOL OF ELECTRICAL AND COMPUTER ENGINEERING

Athens, Greece
6th – 8th November, 2008

KING

Edited by Prof. Dr. Eng. **Dimiter Tz. Dimitrov**

ISBN 978-954-9518-58-0

Printed in Bulgaria

D. Dimitrov

Dear Colleagues,

It's my privilege to thanks to all of you for your contributions submitted at 3rd regular International Conference on 'Communication, Electromagnetics and Medical Applications' CEMA'08. This is one conference which should help future collaboration between engineering, especially communication technologies and medicine. This is an important scientific event not only in Balkan region, but in Europe, also. The International Conference on Communication, Electromagnetism and Medical Application CEMA'08 is dedicated to all essential aspects of the development of global information and communication technologies and their impact for medicine. The objective of Conference is to bring together lecturers, researchers and practitioners from different countries, working on the field of communication, electromagnetism and medical applications, computer simulation of electromagnetic field, in order to exchange information and bring new contribution to this important field of engineering design and application in medicine. The Conference will bring you the latest ideas and development of the tools for the above mentioned scientific areas directly from their inventors. The objective of the Conference is also to bring together the academic community, researchers and practitioners working in the field of Communication, Electromagnetics and Medical Applications, not only from all over Europe, but also from USA, Russia, China, Canada etc., in order to exchange information and present new scientific and technical contributions. Many well known scientists not only from Europe took part in conference preparation as members of International Scientific Committee or/and as reviewers of submitted paper. I would like to thanks to all of them for their efforts, for their suggestions and advices.

On behalf of the International Scientific Committee, I would like to wish you successful presentations of your papers, successful discussions and new collaborations for your future scientific investigations. Engineering and medicine should provide high level of live for all people.

Dimiter Tz. Dimitrov
Conference Chairman

SCIENTIFIC PROGRAM

6th November, 2008

09h30-10h, a.m.

Opening ceremony

Conference room in the 1st floor of
NTUA University Administration building

FIRST SESSION

10-12h, Conference room

Chairman: *Prof. L. Svilainis, Kaunas University of Technology, Lithuania*

---

1. *Charalampos G. Moschovitis[1], Hristos T. Anastassiu[2] and Panayiotis V. Frangos[1,]*
[1]National Technical University of Athens, School of Electrical and Computer Engineering, Division of Information Transmission Systems and Materials Technology,
Calculation results of scattering of electromagnetic waves from rectangular perfectly conducting plate using an extended three dimensional Stationary Phase Method which is based on Fresnel functions (SPM-F)

2. *Veselin Demirev*, Faculty of Telecommunications, TU–Sofia, Bulgaria,
Review of SCP Test Set-up and Results - I

3. *Veselin Demirev*, Faculty of Telecommunications, TU–Sofia, Bulgaria,
Review of SCP Test Set-up and Results – II

4. *Alexander Bekiarski, Snejana Pleshkova-Bekiarska*, Faculty of Telecommunications, Technical University–Sofia, Bulgaria,
Visual Design of Mobile Robot Audio and Video System in 2D Space of Observation

5. *Alexander Bekiarski, Snejana Pleshkova-Bekiarska* , Faculty of Telecommunications, Technical University-Sofia, Bulgaria,
Simulation of Audio Visual Robot Perception of Speech Signals and Visual Information

Lunch
12h -13h30
NTUA University building

SECOND SESSION

13h30–15h30, Conference room

Chairman: *Prof. P. Frangos,National Technical University of Athens, Greece*

---

1. *T. Kersys, R. Anilionis, D. Eidukas*, Kaunas University of Technology, Lithuania,
   Mathematical Simulation Program of Doped Si Oxidation in Nano-dimension Scale

2. *D. Andriukaitis, R. Anilionis,* Kaunas University of Technology, Lithuania,
   Investigation of Etching Process and Different Crystallographic Plane Orientation Dependence Mathematical Simulation in Nano Scale Structures

3. *L. Svilainis, V. Dumbrava,* Kaunas University of Technology, Lithuania,
   The complex AC response measurement with USB connectivity to PC

4. *Darius Jegelevicius[1,2], Vaidotas Marozas[1,2], Arunas Lukoševičius[1,2], Linas Svilainis[2]*, Kaunas University of Technology, Lithuania,[2]
   Acquisition and processing of photoplethysmographic signal for registration of heart rate of moving person

5. *Andrew Andreev, Anna Andonova, Ivo Iliev*, Bulgarian Academy of Sciences, Sofia, Bulgaria,
   Measurement of IR Temperature Deviation in Bio-Medicine

Break

15h30-16h

THIRD SESSION

16h – 17h30, Conference room

Chairman**:** *Prof. A. Bekiarski, Technical University-Sofia, Bulgaria*

---

1. *Dimiter Tz. Dimitrov*, Miglena D. Dontshewa***, Faculty of Telecommunications, Technical University of Sofia, Bulgaria*, University of Applied Sciences, Dornbirn, Austria**,
   Space configuration of low frequency magnetic field, generated by apparatus for magneto-therapy using girdle coil

2. *Viktor V. Mihaylov, Kalin L. Dimitrov, Dimitar Tz. Dimitrov,* Faculty of Telecommunications, Technical University of Sofia, Bulgaria,
   Research on the influence of permanent magnetic field during live tissue laser treatment

3. *Valentin Hristov, Mario Kanchev*, South-West University – Blagoevgrad, Bulgaria,
   Investigation of Triple Play Services

4. *Valentin Panchev Hristov, Ivaylo Veselinov Petrov*, South-West University – Blagoevgrad, Bulgaria,
Investigation of 802.11 n wlan throughput

5. *Dimitar Diakov, Mladen Milushev, & Vania Georgieva,* Technical University of Sofia, Bulgaria,
Hall sensor for the stepping contact force

Dinner in NTUA University building
18h-20h
(if wanted)

07.11.2008, Wednesday

FOUR SESSION

9h30- 11h30, Conference room

Chairman*: *Prof. V.Demirev, Technical University-Sofia, Bulgaria

---

1. *Nikola Dimitrov Ralev*, Faculty of Telecommunications, Technical University of Sofia, Bulgaria,
Movement of charged particle in alive tissues under external electrical field

2. *Nikola Dimitrov Ralev*, Faculty of Telecommunications, Technical University of Sofia, Bulgaria,
Transcutaneous electrical stimulation

3. *Hristo Damianov, Matei Gavrilov, Borislav Tonev,* Medical University of Sofia, Bulgaria,
Some results on clinical application of low frequency magnetic field created by apparatus for magnetotherapy

4. *Veska M. Georgieva*, Faculty of Telecommunications, Technical University of Sofia, Bulgaria,
Ultrasound Medical Images Enhancement on the base of Morphological Processing

5. *Boncho A. Bonchev*, Faculty of Telecommunications, Technical University of Sofia, Bulgaria,
Movement of ions in alive tissues under uniform magnetic field of apparatus for magnetotherapy and uniform electrical fields

6. *Boncho A. Bonchev*, Faculty of Telecommunications, Technical University of Sofia, Bulgaria,
Movement of ions in alive tissues under nonuniform magnetic fields created by apparatus for magnetotherapy

11h30 -12h Conference room
Conference Closing Ceremony

12h Lunch
NTUA University building

INTERNATIONAL CONFERENCE

on

Communications, Electromagnetics and Medical Applications

(CEMA'08)

Athens, Greece
6th – 8th November, 2008

Organized by:

Faculty of Telecommunications
of Technical University-Sofia, Bulgaria

NATIONAL TECHNICAL UNIVERSITY OF ATHENS, GREECE

SCHOOL OF ELECTRICAL AND COMPUTER ENGINEERING

INTERNATIONAL SCIENTIFIC COMMITTEE

***Honorary Chairman*:** Prof. NIKOLAOS K. UZUNOGLU,
National Technical University of Athens, Greece

***Chairman*:** Prof. D. Tz. DIMITROV,
Technical University of Sofia, Bulgaria

***Vice Chairman*:** Prof. P. FRANGOS,
National Technical University of Athens, Greece

MEMBERS:

I. ALIFERIS,	University of Nice, France
N. AMPILOVA,	University of Perersburg, Russia
Q. BALZANO,	University of Maryland, USA
A. BEKJARSKY,	Technical University of Sofia, Bulgaria
H. BERG,	Technical University of Jena, Germany
J. CATRYSSE,	Katholieke Hogenschool Brugge Oostende, Belgium
Ph. CONSTANTINOU,	National Technical University of Athens, Greece
J. DAUVIGNAC,	University of Nice, France
B. DEKERIS,	Kaunas University of Technology, Litvania
V. DEMIREV,	Technical University of Sofia, Bulgaria
M. DONTSCHEWA,	University of Applied Sciences, Dorbirn, Austria
V. DUMBRAVA,	Kaunas University of Technology, Litvania
D. EIDUKAS,	Kaunas University of Technology, Litvania
S. Ver HOEYE,	University of Oviedo, Spain
M. HOFMANN,	University of Ulm, Germany
V. HRISTOV,	University of Blagoevgrad, Bulgaria
I. ILIEV,	Technical University of Sofia, Bulgaria
R. KRIVICKAS,	Kaunas University of Technology, Litvania
G. MALLET,	University "Sophia Antipolis", Nice, France
R. De LEO,	Universita, Politecnica della Marche, Italy
V. MARINKEV,	Medical University of Plovdiv, Bulgaria
M.MARTINS,	Instituto Superior Técnico, Lisboa, Portugal
K. NIKITA,	National Technical University of Athens, Greece
M. NIKOLOVA,	High Naval School, Varna, Bulgaria
M. PASTORINO,	University of Genova, Italy
J. PETROVSKA,	Medical University of Sofia, Bulgaria
Ch. PICHOT,	University of Nice, France
F. PRATO,	University of Western Ontario, Canada
A.SAVOV,	Medical University of Sofia, Bulgaria
L.SVILAINIS,	Kaunas University of Technology, Litvania
H-P. SCHADE,	Technical University of Ilmenau, Germany
L. SONG,	Technical University of Harbin, China
K. VLADIMIROV,	Medical University of Sofia, Bulgaria

CONTACT US:
http://tu-sofia.bg/fktt/cema08/

GENERAL INFORMATION AND SUBMISSION OF CONTRIBUTIONS

Prof. Dr. Dimiter Dimitrov
Faculty of Telecommunications
Technical University of Sofia
8, Kliment Ohridsky str.
1756 Sofia, Bulgaria
Phone: ++359 2 9652278
Fax: ++3592 9741360
E-mail: dcd@tu-sofia.bg

HOTEL RESERVATION AND CULTURAL PROGRAM

Prof. P. Frangos
National Technical University of Athens
School of Electrical and Computer Engineering
9, Iroon Polytechniou Str.,
157 73 Zografou, Athens, Greece
Phone: 00 30 210 772 3694
Fax: 00 30 210 772 2281
E-mail: pfrangos@central.ntua.gr

GENERAL INFORMATION

Submission of contributions

Prof. Dr. Dimiter Dimitrov

Faculty of Telecommunication
Technical University of Sofia
8, Kliment Ohridsky str.
1756 Sofia, Bulgaria
Phone: ++359 2 9652278
E-mail: dcd@tu-sofia.bg

Prof. P. Frangos

National Technical University of Athens
School of Electrical and Computer Engineering
9, Iroon Polytechniou Str. ,
157 73 Zografou, Athens, Greece
Phone: 00 30 210 772 3694
Fax: 00 30 210 772 2281
E-mail: pfrangos@central.ntua.gr

REVIEWERS

M. DONTSCHEWA,	University of Applied Sciences, Dorbirn, Austria
V. MARINKEV,	Medical University of Plovdiv, Bulgaria
M. NIKOLOVA,	High Naval School, Varna, Bulgaria
J. PETROVSKA,	Medical University of Sofia, Bulgaria
A. SAVOV,	Medical University of Sofia, Bulgaria
K. VLADIMIROV,	Medical University of Sofia, Bulgaria
L. SONG,	Technical University of Harbin, China
S. Ver HOEYE,	University of Oviedo, Spain
E. BOEMO,	Technical University of Madrid, Spain
M. HOFMANN,	University of Ulm, Germany
F. KLETT,	Franhofer Institute, Ilmenau, Germany
H-P. SCHADE,	Technical University of Ilmenau, Germany
H. BERG,	Technical University of Jena, Germany
N. AMPILOVA,	University of Perersburg, Russia
Q. BALZANO,	University of Maryland, USA
A. USHEVA,	University of Boston, USA
G. MALLET,	University “Sophia Antipolis”, Nice, France
M. MARTINS,	Instituto Superior Técnico, Lisboa, Portugal

TABLE OF CONTENTS

CALCULATION RESULTS OF SCATTERING OF ELECTROMAGNETIC WAVES FROM RECTANGULAR PERFECTLY CONDUCTING PLATE USING AN EXTENDED THREE DIMENSIONAL STATIONARY PHASE METHOD WHICH IS BASED ON FRESNEL FUNCTIONS (SPM-F)

Charalampos G. Moschovitis[1], Hristos T. Anastassiu[2] and Panayiotis V. Frangos[1]

[1]National Technical University of Athens,
School of Electrical and Computer Engineering,
Division of Information Transmission Systems and Materials Technology
9, Iroon Polytechniou Str., GR-15780 Zografou, Athens, Greece
(phone: +30-210-772-3694; fax: +30-210-772-2281;
e-mail: pfrangos@central.ntua.gr).
[2]Hellenic Aerospace Industry,
PO Box 23, GR-32009
Schimatari - Tanagra / Viotia Greece

.

Abstract

Radiocoverage simulation tools require multiple scattering radio propagation calculations in urban outdoor areas. The simulation results, if performed numerically, are usually time consuming due to the multiple numerical calculations included in their core scattering formulas. The main goal of this paper is to present the calculation results of an extended three dimensional Stationary Phase Method which is based on Fresnel functions (SPM-F). In previous conferences we presented a novel three dimensional high frequency analytical method for the calculation of the scattered electromagnetic (EM) field from a Perfect Electric Conductor (PEC) plate, which is based on the Physical Optics (PO) approximation and the Stationary Phase Method (SPM) approximation. This method (SPM) showed fast and accurate results, nevertheless its accuracy around the area of the main scattering lobe could be further enhanced by utilizing higher order approximation terms, based on the use of Fresnel functions (SPM-F). Then, proximity of the stationary point to the edges of the scatterer does not constitute a problem anymore, since the troublesome vanishing denominators have now been removed.

1. INTRODUCTION

Radio coverage prediction models [1] require several calculations of scattering of electromagnetic waves. In references [2]-[3] we have developed and presented an enhanced three dimensional analytical formulation for the calculation of the vector potential and eventually the scattered electric field of a geometry presented in Fig. 1. The method is based on the Stationary Phase Method (SPM) and its novelty lies on the inclusion of the edge contribution to the resulting asymptotic expressions, a fact which was not documented in the literature for the case of a double integral. In this paper we present a higher order approximation term for the edge contribution, which is based again on the Stationary Phase Method, but also includes Fresnel functions (SPM-F). Vector potential and scattered electric field calculations appear in section 2, below, while the general idea of this new approach is presented in section 3 of this paper. The Fresnel functions in SPM analytical results have not been documented either in literature. In section 4, below, simulation results are compared to results obtained with standard numerical integration and SPM results that do not include

the Fresnel functions, for the case of single and double integrals and for small/large scatterers in the areas of Near field, Fresnel Zone and Far Field. SPM-F method presented here, is found to be equally fast to SPM, but more accurate in the area of the main scattering lobe, where proximity of the stationary point to the edges and vanishing denominators in edge contribution equations was causing some inaccuracies to the earlier derived SPM results.

The generalization of the method leads to a three dimensional model which works properly, if both transmitter and receiver are located below rooftop level and well above the ground. Then the three dimensional scattering could be modeled through the prerequisite problem of an electromagnetic (EM) wave which is assumed to be incident on a perfectly conducting rectangular plate of finite dimensions which in real life happens to be the road-side of a three dimensional building.

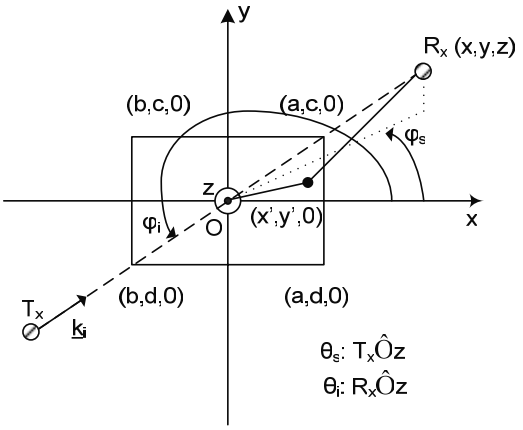

Figure 1 - 3D geometry xy plane projection

Let us consider the observation point $R_x(x,y,z)$ in a propagation problem layout of an electromagnetic (EM) wave with wavevector k_i, which is assumed to be incident on a perfectly conducting rectangular plate of finite dimensions (Fig.1).

This three dimensional scatterer is the necessary prerequisite in order to model propagation in an urban outdoor environment, which consists of three dimensional walls and obstacles that often pertain to modern high frequency communication wireless networks, such as GSM, UMTS, Wi-Fi and Wi-Max technologies. Should the rectangular plate lies on the xy plane, and since the operating frequency is considered to be 1GHz or higher, the following calculations regarding vector potential and scattered electric field hold.

2. VECTOR POTENTIAL $\vec{A}$ AND SCATTERED ELECTRIC FIELD $\vec{E}$

According to the layout in Fig. 1 the induced current density on the surface of the plate after applying P.O. theory yields the following expression:

$$\underline{J}_s^{P.O.}(x',y') = \frac{-2e^{jkh}}{\eta}[\hat{x}(E_{0\theta}\cos\phi_i - \\ -\mathrm{E}_{0\phi}\cos\theta_i\sin\phi_i) + \hat{y}(E_{0\theta}\sin\phi_i + \\ +E_{0\phi}\cos\theta_i\cos\phi_i)] \quad (1)$$

By utilising the three dimensional Green's function given below:

$$G(r,r') = \frac{\exp(-j\cdot k\cdot|r-r'|)}{4\pi\cdot|r-r'|} \quad (2)$$

the vector potential $\vec{A}$ at the observation point $R_x(x,y,z)$ is given by:

$$\underline{A}(x,y,z) = \mu_0\cdot\int_{y'=d}^{c}\int_{x'=b}^{a}\left[\vec{J}_s^{P.O.}(x',y')\cdot G(r,r')\right]\cdot dx'dy' \quad (3)$$

Substitution of total current density yields the following expression for the vector potential:

$$\underline{A}(x,y,z) = \frac{-\mu_0}{2\pi\cdot\eta}\cdot \\ [\hat{x}\cdot(E_{0\theta}\cdot\cos\phi_i - \mathrm{E}_{0\phi}\cdot\cos\theta_i\cdot\sin\phi_i) + \\ +\hat{y}\cdot(E_{0\theta}\cdot\sin\phi_i + E_{0\phi}\cdot\cos\theta_i\cdot\cos\phi_i)]\cdot \\ \cdot\int_{y'=d}^{c}\int_{x'=b}^{a}\frac{\exp\left\{j\cdot k\left[(x'\cdot K + y'\cdot L) - \sqrt{(x-x')^2+(y-y')^2+z^2}\right]\right\}}{\sqrt{(x-x')^2+(y-y')^2+z^2}}dx'dy' \quad (4)$$

since it is easily obtained from Fig. 1 that

$$|\underline{r}-\underline{r'}| = \sqrt{(x-x')^2+(y-y')^2+z^2} \quad (5)$$

and K, L constants which depend on the incident angles θ_i and φ_i satisfying Eqs. 6-7:

$$K = \sin\theta_i \cdot \cos\phi_i \quad (6)$$

$$L = \sin\theta_i \cdot \sin\phi_i \quad (7)$$

Finally, the scattered electric field is calculated from the formula:

$$\underline{E}_s(x,y,z) = \\ = -j\cdot\omega\cdot\underline{A} - j\cdot\frac{\omega}{k^2}\cdot grad\left(div\left(\underline{A}\right)\right) \quad (8)$$

3. SPM-F METHOD

Operating at the frequency of 1GHz or higher, scatterers that appear in the above networks are considered to be electrically large, and current density may be calculated with good accuracy using the physical optics (P.O.) approximation. Modifying appropriately Eq. 4 we can apply SPM approximations which result in calculating the vector potential and eventually the total scattered electric field at the observation point $R_x(x,y,z)$. The amplitude and phase functions we use are derived in Eqs. 9-10 respectively:

$$F(x',y') = \frac{1}{\sqrt{(x-x')^2+(y-y')^2+z^2}} \quad (9)$$

$$f(x',y') = x'K + y'L - \\ -\sqrt{(x-x')^2+(y-y')^2+z^2} \quad (10)$$

As described in [2]-[3], the inner integral terms of the three dimensional modified Stationary Phase Method which perform the calculation of the diffraction from the edges of the PEC plate (a, b) and (c ,d), should be replaced [4] by higher order approximation terms that imply the use of Fresnel functions, i.e. the substitution for term I_a should be:

$$\tilde{I}'_a = -\frac{1}{jk}\frac{F(a,y')}{\left.\frac{\partial f}{\partial x'}\right|_{x'=a,y'=y'}}\exp\{jkf(a,y')\} + O\left(k^{-2}\right)\leftrightarrow$$

$$\tilde{I}'_a = \varepsilon_1\cdot F(a,y')\exp\left\{jkf(a,y') \mp ju_a^2\right\}\times$$

$$\times\sqrt{\frac{2}{k\left|\left.\frac{\partial^2 f}{\partial x'^2}\right|_{x'=a,y'=y'}\right|}}F_{\pm}[u(a,y')] \quad (11)$$

where, in the above replacement, the new term represents a higher order approximation that includes a Fresnel function $F_{\pm}(u)$ [$F_{\pm}(u) = \int_u^{\infty}\exp\left(\pm jt^2\right)dt$] and

$$\varepsilon_1 = \mathrm{sgn}(a - x_o) \quad (12)$$

$$u_a = \sqrt{\frac{k}{2\left|\left.\frac{\partial^2 f}{\partial x'^2}\right|_{x'=a,y'=y'}\right|}}\left|\left.\frac{\partial f}{\partial x'}\right|_{x'=a,y'=y'}\right| \quad (13)$$

The replacement for term I_b is given by:

$$\tilde{I}'_b = -\frac{1}{jk}\frac{F(b,y')}{\left.\frac{\partial f}{\partial x'}\right|_{x'=b,y'=y'}}\exp\{jkf(b,y')\} + O\left(k^{-2}\right)\leftrightarrow$$

$$\tilde{I}'_b = \varepsilon_2\cdot F(b,y')\exp\left\{jkf(b,y') \mp ju_b^2\right\}\times$$

$$\times\sqrt{\frac{2}{k\left|\left.\frac{\partial^2 f}{\partial x'^2}\right|_{x'=b,y'=y'}\right|}}F_{\pm}[u(b,y')] \quad (14)$$

$$\varepsilon_1 = \mathrm{sgn}(b - x_o) \quad (15)$$

$$u_b = \sqrt{\frac{k}{2\left|\left.\frac{\partial^2 f}{\partial x'^2}\right|_{x'=b,y'=y'}\right|}}\left|\left.\frac{\partial f}{\partial x'}\right|_{x'=b,y'=y'}\right| \quad (16)$$

In the case of scattering from a rectangular plate in three dimensions, the above formulas will escalate accordingly to all eight terms of the modified Stationary Phase Method as described in [2],[3].

The idea of our calculation approach has been presented in [2], [3]. The initial integral is extended to infinite for both x' and y' variables. This extension primarily enables us to utilize the standard SPM formulas, well known for an infinite double integral. Since the plate is finite, additional correction terms should be included in the final SPM result. Those terms are obtained by subtracting the remaining areas around the finite plate. For those terms, the results are computed by utilizing a combination of SPM and edge contribution side formulas, that include the Fresnel functions and which have only been

documented for a single integral. By applying such calculations twice, we produce new amplitude and phase functions on which we re-apply SPM approximations, and finally result in analytical solutions for a double integral using Fresnel functions for the edge contribution.

4. SIMULATION RESULTS

The accuracy of our Fresnel asymptotic calculations can be evaluated by using, standard (e.g. Gaussian) numerical integration. We present here a set of results based on three different methods. SPM-F results are drawn in cyan line and include the Fresnel functions in edge contribution, SPM results drawn in red line (also presented in [2], [3]), and numerical integration results drawn in blue line. Due to the complexity of the functions on which SPM is applied, the calculations were carried out using MATLAB's symbolic toolbox. Analytical results derived from MATLAB calculations constitute an aggregation of complicated formulas. The total scattered electric field was calculated for distances in the Far Field, Fresnel Region and Near Field area. In Figs. 2–13 we compare SPM-F, SPM and numerical integration for the frequency of 1GHz and for the case of single and double integrals. Line segments (single integrals) and rectangular plates (double integrals) with side length equal from 20λ to 80λ were examined in our simulation results. Elevation and azimuth angles of incidence were assumed equal to 45 degrees.

4.1. Single Integral

4.1.1. Small Scatterer

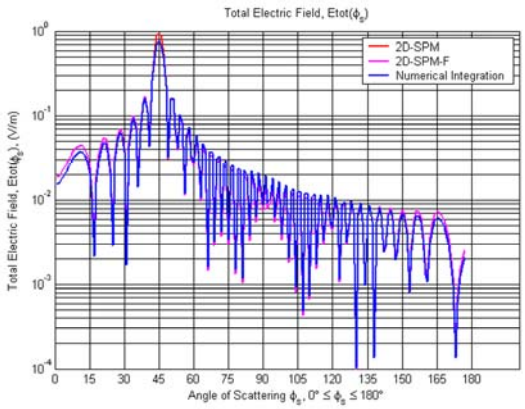

Figure 2. 20λ line segment, Far Field area

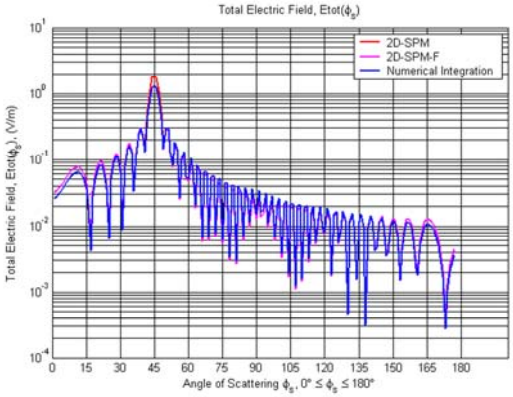

Figure 3. 20λ line segment, Fresnel area

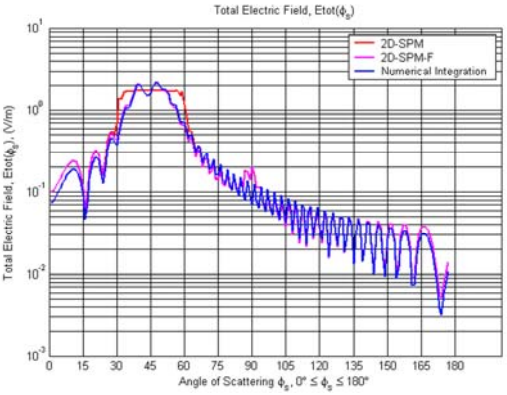

Figure 4. 20λ line segment, Near Field area

In Figs. 2–4 above, numerical results are shown for a rectangular line segment of dimension 20λ in the Far Field area (r=300m), the Fresnel area (r=100m) and the Near Field area (r=10m).

4.1.2.. Large Scatterer

In Figs. 5–7, we provide numerical results for the case of a larger scatterer of dimension 80λ in the Far Field area (r=4500m), the Fresnel area (r=1000m) and the Near Field area (r=100m).

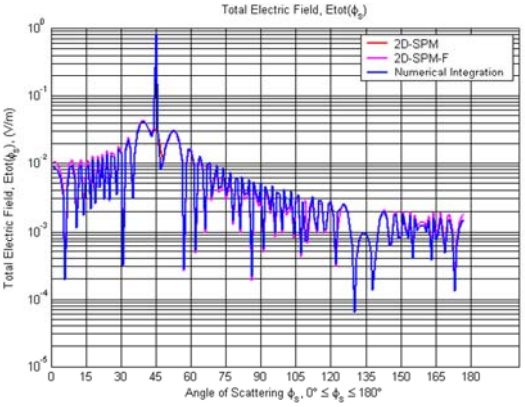

Figure 5. 80λ line segment, Far Field area

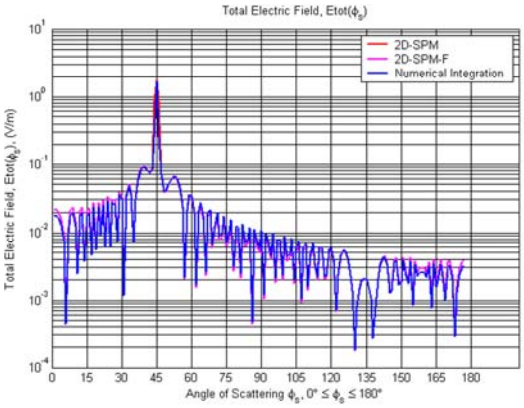

Figure 6. 80λ line segment, Fresnel area

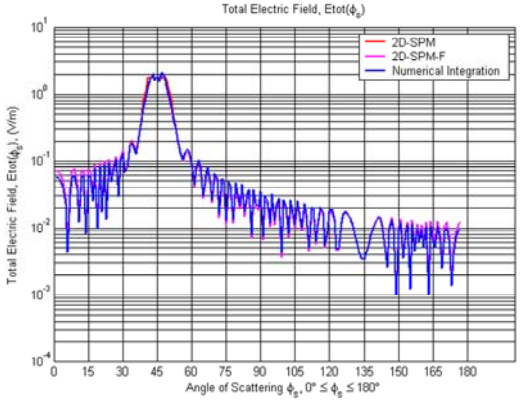

Figure 7. 80λ line segment, Near Field area

4.2. Double Integral

4.2.1. Small Scatterer

Scatterer of dimension 20λ in the Far Field area (r=600m), the Fresnel area (r=100m) and the Near Field area (r=25m) (Figs 8-10).

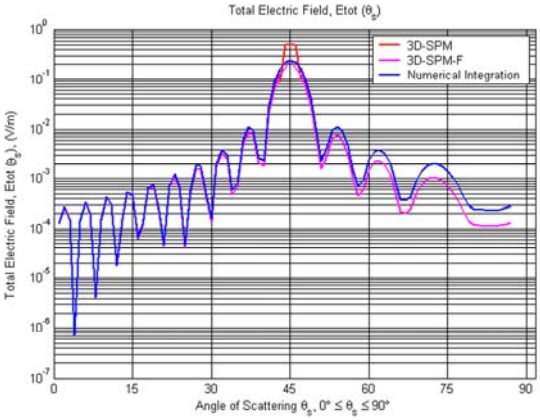

Figure 8. 20λ plate side, Far Field area

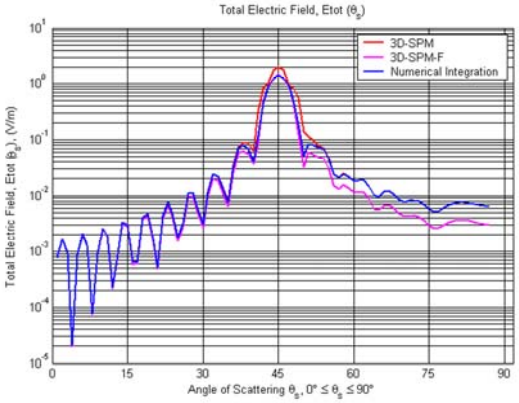

Figure 9. 20λ plate side, Fresnel area

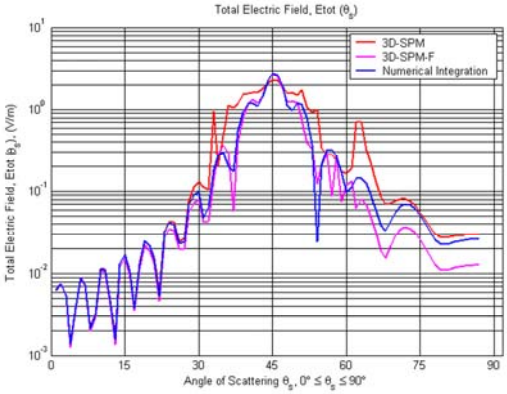

Figure 10. 20λ plate side, Near Field area

4.2.2.. Large Scatterer

Scatterer of dimension 80λ in the Far Field area (r=9000m), the Fresnel area (r=500m) and the Near Field area (r=200m) (Figs. 11-13).

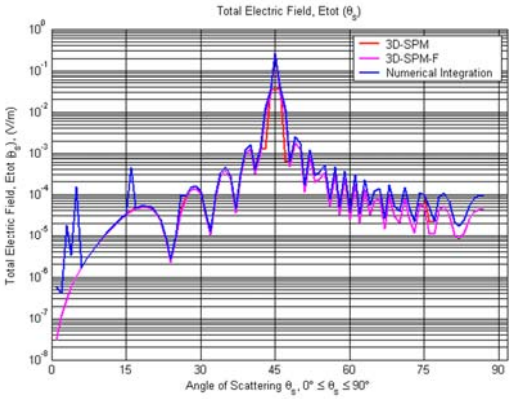

Figure 11. 80λ plate side, Far Field area

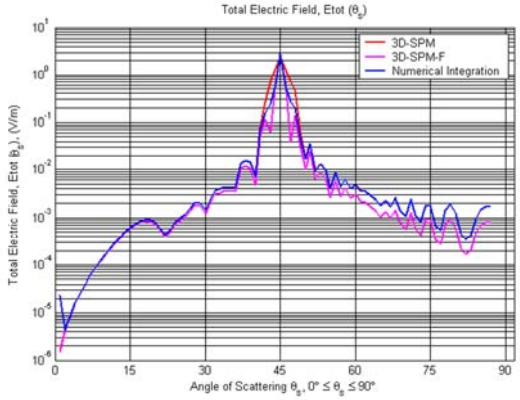

Figure 12. 80λ plate side, Fresnel area

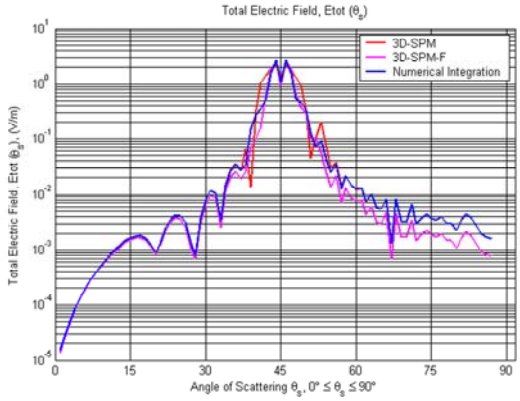

Figure 13. 80λ plate side, Near Field area

Comparison graphs in Figs. 2 – 13 above indicate the improved behaviour around the area of the main scattering lobe between the asymptotic results of the SPM and SPM-F methods. Note here that for large angles of scattering θ_s (θ_s>60^o) parameters u_a, u_b in Eqns. (13),(16) are larger than 3.0 (u_a,u_b>3.0) thus the replacement formulas in Eqns. (11),(14) are not uniform [4], and equations without Fresnel functions [2],[3] must be used for best accuracy (i.e. combination formulas, which are currently developed by our research group).

5. CONCLUSION

Even though rather complicated mathematical formulas are involved in the proposed SPM-F method, it is much faster than the numerical integration method (3-150 times faster). This is very important for a simulated propagation problem in an urban outdoor environment, in which case many scatterers (walls) and multiple reflection phenomena are present. Furthermore, SPM-F method presented here was found also to be very accurate for the calculation of vector potential $\vec{A}$ and electric field $\vec{E}$ in various radio propagation simulation tools.

References

[1] E. G. Papkelis, I. Psarros, I. Ch. Ouranos, Ch. G. Moschovitis, K. T. Karakatselos, E. Vagenas, H. T. Anastassiu and P. V. Frangos, 'A Radio Coverage Prediction Model in Wireless Communication Systems based on Physical Optics and the Physical Theory of Diffraction', IEEE Antennas and Propagation Magazine, vol. 49, no.2, pp. 156-165, April 2007.

[2] Ch. G. Moschovitis, E. G. Papkelis, H. T. Anastassiu, K. T. Karakatselos, I. Ch. Ouranos, N. G. Freskas, and P.V.Frangos, 'Asymptotic Calculation of the Scattered Electric Field from a Finite Rectangular Plate using an Enhanced Stationary Phase Method (SPM) Approximation', European Conference on Antennas and Propagation (EuCAP 2006), November 6-10, 2006, Nice, France.

[3] Ch. G. Moschovitis, E. G. Papkelis, Dr H. T. Anastassiu, K. T. Karakatselos, I. Ch. Ouranos, N. G. Freskas, Prof., P. V. Frangos "An application of an enhanced Stationary Phase Method (SPM) approximation for the asymptotic calculation of the scattered electric field from a finite rectangular plate", International Conference on Communications, Electromagnetics and Medical Applications (CEMA'06), October 19 -21, 2006, Sofia, Bulgaria

[4] Graeme L. James, Geometrical Theory Of Diffraction for Electromagnetic Waves, Peter Peregrinus Ltd. (IEE), pp. 30-42, 61, 90 and 117-123, United Kingdom, 2003.

REVIEW OF SCP TEST SET-UP AND RESULTS – I

D-r Veselin Demirev

Faculty of Telecommunications, TU – Sofia,
"Kl. Ohridsky" blvd. N8, 1756 – Sofia, Bulgaria, E-mail: demirev_v@tu-sofia.bg

Abstract

The specific test set-up equipment and the obtained experimental results of the proposed by the author SCP technology are given in the report. Special attention is given to the methods and equipment, suitable to perform SCP processing in the simplest way. Two analog schemes for SCP processing, as well as the obtained by them experimental results, are considered. The results supports the validity of the two main properties of the SCP technology – the spatial selectivity between different radio sources, as well as the obtained high antenna gain. The disadvantages of the used methods, leading to deep ripples of the spatial distribution of the system sensitivity, are mentioned too.

1. BASIC SCP CONCEPT

The block scheme of the basic SCP concept is shown in fig. 1. The objectives of this communication principle is to receive one or more radio signals coming from one or several spatially distributed sources (satellites), insuring high gain of the antenna systems, as well as to ensure spatial selectivity high enough to cancel the same frequency channel interference, coming from different space directions [1].

The objectives stated above are achieved by a patented method for radio communications, which proposes application of additional pilot signal transmitted in the band of information signals and available in the receiver by one of the known methods for access [2]. SCP receiver terminal is equipped with random phased antenna array. The phase shifts of the signals, coming from the antenna elements, are random at the antenna output regardless of the information source direction. These phase spread signals correlate with the recovered pilot signal, phase spread in the same manner, in a correlator. Since this pilot comes from the same direction and propagates in the same random environment to the antenna output, it should have the same phase spread as the information one. The result of the correlation process is the recovered information signal at low intermediate frequency or at baseband. The signals coming from other satellites will propagate in different random environment. Their phase spread will be different from those of the chosen pilot and will not correlate with it during the signal processing.

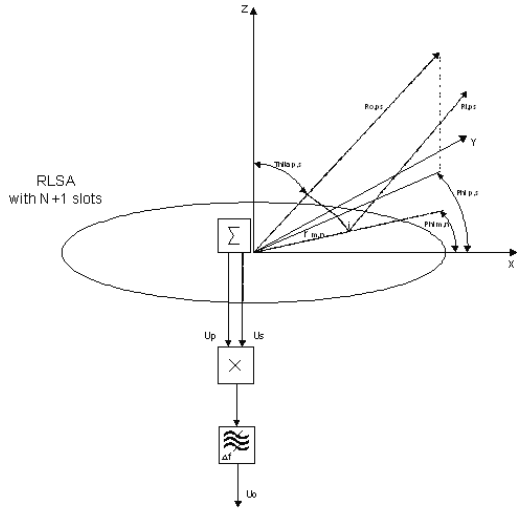

Figure 1. Basic SCP concept block scheme

2. FIRST SCP TEST SET-UP

The objectives of the first tests were to prove in experimental way the SCP approach with available standard equipment, as well as to test in anechoic chamber the shape of the SCP cooperative pattern of a random phased Radial Line Slot Antenna (RLSA) with diameter Φ 30 cm. The experiments were held in the following conditions:

- The tests were held in SkyGate (SG) anechoic chamber facility, the distance between transmit and receive antenna was 3,5 m.
- Two signal generators (simulated pilot and unmodulated information signals) were used (Fig.2).
- Standard detector mount HP 8470 A was used as mixer (correlator) at first IF=1,5 GHz.
- RLSA with diameter Φ=30 cm and with about 300 random distributed slots were used.

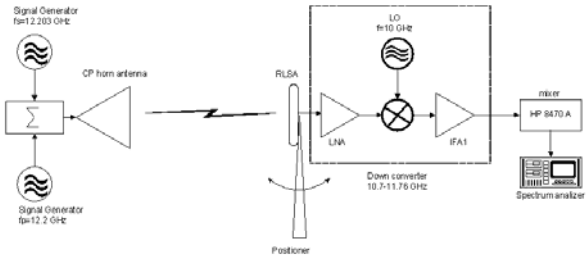

Figure 2. First SCP test set-up

Hundred tests were performed in order to meet the objectives, mentioned above. The variable parameters in the different tests were:

- Frequency
- Slots distributions, inclinations and numbers
- RLSA high and permittivity
- Polarizations and angles of the antenna pattern cuts

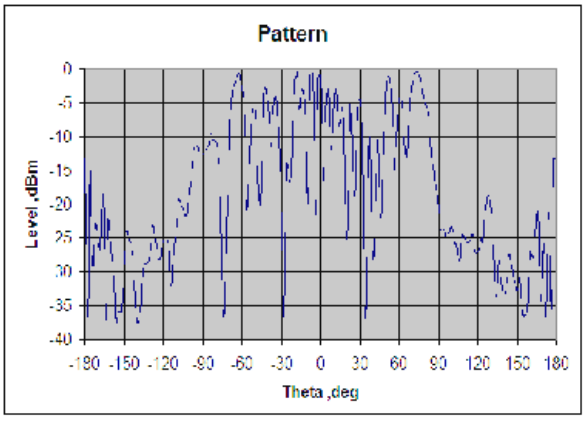

Figure 3. SCP cooperative pattern of RLSA with diameter 30 cm

A typical cooperative pattern of RLSA with Φ 30 cm is shown in fig. 3.

Conclusions, based on the first tests trials, could be summarized as follows:

- The tests proved the main SCP principle – the phase dispreading during the process of correlation, as well as the signal recovery.
- The obtained cooperative patterns are approximately uniform in the tilt angles of +-70 deg., which means that it is possible to use the RLSA in horizontal position as mobile receiving antenna in GSO satellite environment.
- The obtained cooperative patterns suffer from big ripples (up to 20-30 dB). It means that the system will have different sensitivity for different azimuth and elevation angles. As reasons for this ripples at the test time were considered:
  - The phase correlation among the neighbor slots, due to poor design.
  - The low number of slot radiators.

The solution, based on the above conclusions, was that the sensitivity of the equipment, as well as the number of the slot radiators should be increased significant.

3. SECOND SCP TEST SET-UP

The objectives of the second SCP test set-up and trials were to prove in experimental way the SCP approach in receive mode with improved (more sensitive) nonstandard equipment, as well as to test the shape of the SCP cooperative pattern of RLSA - Φ 30 cm and RLSA - Φ 57 cm at different polarizations and simulated satellite Effective Isotropic Radiated Powers (EIRP,s).

The specific conditions here were as follows:

- One RF generator for easy tuning in SG open range conditions was used. Pulse modulation with Fmod=10 KHz was used for 100% amplitude modulation of the RF carrier.
- Modified analog satellite receiver with correlator (analog multiplier) at second IF (480 MHz) was used to improve the sensitivity of the equipment in order to

be closer to the real satellite environment.

- The distance between transmitter and receiver was 3,5 m in anechoic chamber and about 70 m in the open range.

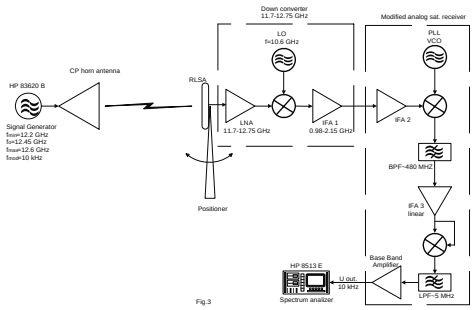

Figure 4. Second SCP test set-up

Hundred tests were performed in order to meet the objectives, mentioned above. The variable parameters in the different tests were:

- Frequency
- Slots distributions, inclinations and numbers
- RLSA high and permittivity
- Polarizations and angles of the antenna pattern cuts
- Satellites EIRP,s

Some of the test results, provided by the second SCP set test-up, are shown in the figures below, as follows:

- Fig. 5. SCP cooperative patterns - test set-up shown in fig.4, RLSA Φ 57 cm, four different cuts of the cooperative SCP pattern.
- Fig. 6. SCP cooperative patterns at differrent simulated EIRP - test set-up shown in fig.4, RLSA Φ 57 cm.
- Fig. 7. SCP cooperative patterns at Right Hand-Left Hand (RH-LH) Circular Polarization - test set-up shown in fig.4, RLSA Φ 57 cm.
- Fig. 8. SCP cooperative patterns - test set-up shown in fig.4, RLSA Φ 30 cm.

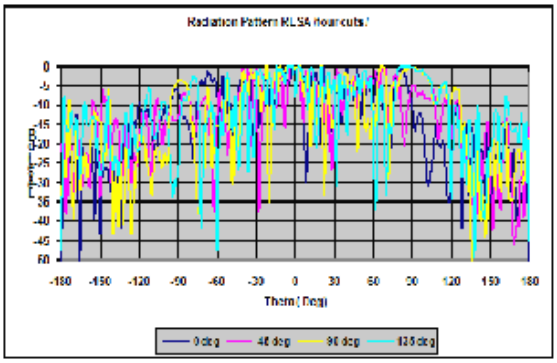

Figure 5. SCP cooperative pattern of RLSA with diameter 57 cm

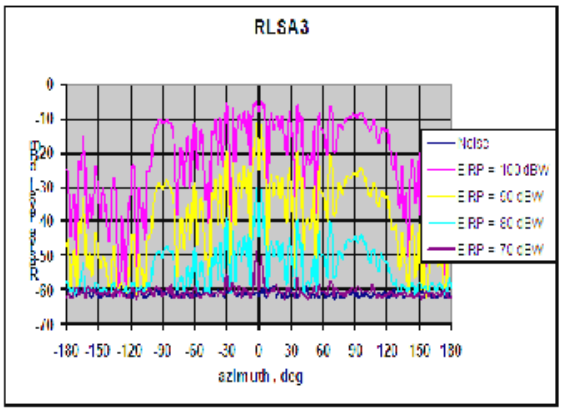

Figure 6. SCP cooperative pattern at different simulated EIRP - RLSA with diameter 57 cm

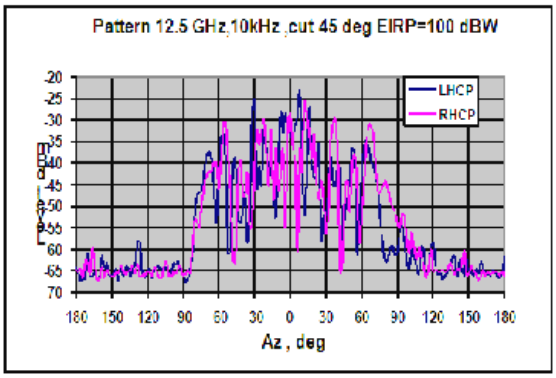

Figure 7. SCP cooperative pattern of RLSA with diameter 57 cm

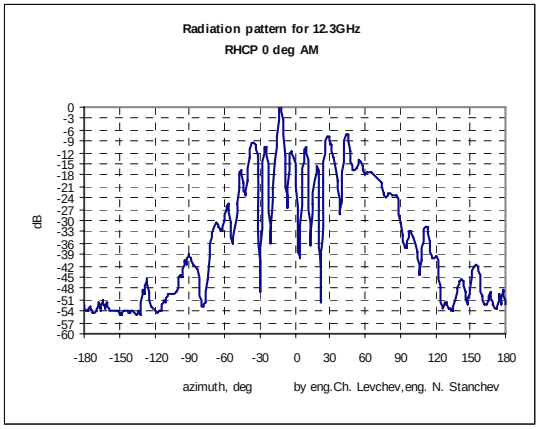

Figure 8. SCP cooperative pattern of RLSA with diameter 30 cm

Conclusions, based on the second tests trials, could be summarized as follows:

- The second generation tests proved again the main SCP principle – the phase dispreading during the process of correlation, as well as the signal recovery.

- The obtained cooperative patterns are approximately uniform in the tilt angles of +-70 deg., which means that it is possible to use the RLSA in horizontal position as mobile receive antenna in GSO satellite environment.

- The test results, shown in fig.6, are very important. They show that the SCP output signals depend on in square low from the EIRP levels (the used receiver is autocorrelation type). This results from the test set-up block-scheme too. In a real SCP-CDMA system the pilot signal will be noise free and his level can be chosen as big as it is necessary for the proper process of correlation. The last means that in such case the SCP output signal will depend linear from EIRP levels. If we reduce the cooperative 100 dBW pattern with 50 dB (EIRP=50 dBW), the computed new pattern will be several dB above the noise floor of the receiver. The last means that the equivalent gain of the RLSA – Φ 57 cm is more than 33 dB.

- The obtained cooperative patterns suffer from big ripples (up to 20-30 dB), which means that the system will have different sensitivity for different azimuth and elevation angles. As reasons for this ripples at the test time were considered:

  – Residual phase correlation among the neighbor slots, due to poor design. For this reason random inclined slots and CP were used in the latest RLSA designs, as well as improved algorithm for random slots distribution.

  – The used signals, as well as the signal processing (correlation) are not exactly the same as that in the proposed SCP system. A precise analysis of the processes in this test system showed that they differ with the proposed in the phase probability density function (in this particular case it is not uniform between 0 and 360 deg.). For this reason SCP test set-up, described in section II, was proposed.

References

[1] V. Demirev, "SCP technology – the new challenge in broadband satellite communications", *ICEST,04 Conference Proceedings,* pp.159-162, Bitola, Macedonia, 2004.

[2] V. Demirev, A. Efremov, "SCP-CDMA GSO,s system proposal", *ICEST,04 Conference Proceedings,* pp.163-166, Bitola, Macedonia, 2004.

REVIEW OF SCP TEST SET-UP AND RESULTS – II

D-r Veselin Demirev

Faculty of Telecommunications, TU – Sofia,
"Kl. Ohridsky" blvd. N8, 1756 – Sofia, Bulgaria, E-mail: demirev_v@tu-sofia.bg

Abstract

The specific test set-up equipment and the obtained experimental results of the proposed by the author SCP technology are given in the report. Special attention is given to the methods and equipment, suitable to measure the spatial interference suppression of the SCP technology. An improved analog scheme for SCP processing (BPSK modulated signal and residual unsuppressed carrier as pilot signal were used), as well as the obtained experimental results, are considered. The objectives of the near field set test-up and trials were to measure the amplitude distribution, as well as the phase distribution of RLSA with random distributed and oriented slots (tangential, inclined and radial, fed by probes).

1. SCP TEST SET-UP FOR SPATIAL INTERFERENCE SUPPRESSION

The objectives of the SCP test set-up and trials for spatial interference suppression are to prove in experimental way the SCP spatial interference rejection with nonstandard equipment, as well as to test in SG anechoic chamber the shapes of the SCP cooperative pattern and spatial interference patterns of RLSA with diameter Φ 30 cm. The test (fig.1) was held in the following conditions:

- In SG anechoic chamber, the distance between transmit and receive antenna was 3,5 m.
- Two signal generators (simulated pilot and information signals) were used. The frequency difference between them is 2 MHz, the term *same sense* in the applied figures means the same CP for information and pilot signals.
- Modified satellite receiver, shown in fig. 1 and [1] was used.
- RLSA with diameter Φ=30 cm and about 300 tangential random distributed slots were used.

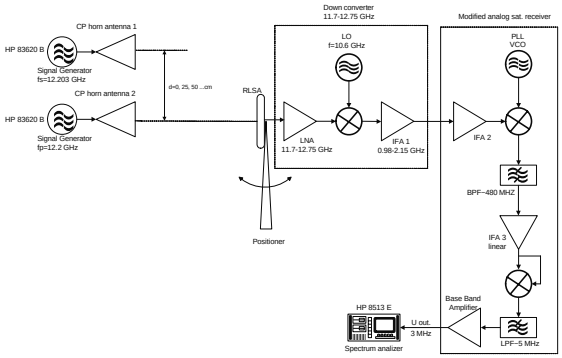

Figure 1. SCP test set-up for spatial interference suppression

The obtained tests results are very important, because the spatial resolution is the second in importance SCP objective. It was studied by means of matrix signal presentations by the author in [2]. Her the final evaluation parameter was named Spatial Cross-Correlation Function (SCCF). The practical measurement of SCCF in SG open test facility is not possible. It needs two points of transmission (one for the pilot and one for the information signal). The information signal transmission point should be shifted at small angles step by step in order the SCCF to be measured precisely. The spatial resolution of a SCP system was tested in anechoic chamber (Fig. 1) only to be proved as principle. The pilot and information sources were shifted in vertical direction at different distances, while the RLSA patterns were tested in the azimuth plane. The results, shown in fig. 2, proved the intuitive and theoretic resolution properties of the SCP approach.

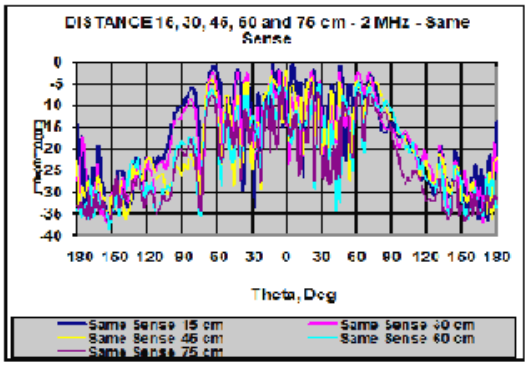

Figure 2. SCP cooperative patterns at different distances between information and pilot sources

2. SCP TEST SET-UP WITH BPSK MODULATED SIGNAL (UNSUPPRESSED CARRIER IS USED AS PILOT SIGNAL)

The objectives of the SCP test set-up and trials with BPSK modulated signal are to prove in experimental way the SCP approach with improved nonstandard equipment (BPSK modulated signal and residual unsuppressed carrier as pilot signal were used), as well as to test with this equipment the shape of the SCP cooperative pattern (RLSA – Φ 30 cm and Φ 57 cm with random distributed and inclined slots, RH-LH CP, V-H P) in SG anechoic chamber and open range test facilities. The test was held in the following conditions:

- The distance between transmit and receive antennas is 3,5 m in anechoic chamber and 20 m in open range.
- The correlation process was held at low First IF=38,9 MHz for simplicity.
- The modulation waveform was 5 MHz pulse signal instead test PN-code for better separation of pilot and information sidebands before the process of correlation in the receiver.

A lot of tests were performed in order to meet the objectives, mentioned above. The variable parameters in the different tests were:

- Frequency
- Slots distributions, inclinations and numbers
- Polarizations and angles of the antenna pattern cuts
- Satellites EIRP

Some of the test results, provided by the last SCP set test-up, are shown in the figures below, as follows:

- Fig. 3. SCP cooperative pattern (test set-up fig. 3, RLSA Φ 57 cm)
- Fig. 4. SCP cooperative patterns at different frequencies (test set-up fig. 3, RLSA Φ 57 cm)
- Fig. 5. SCP cooperative patterns at different EIRP (test set-up fig. 3, RLSA Φ 57 cm)

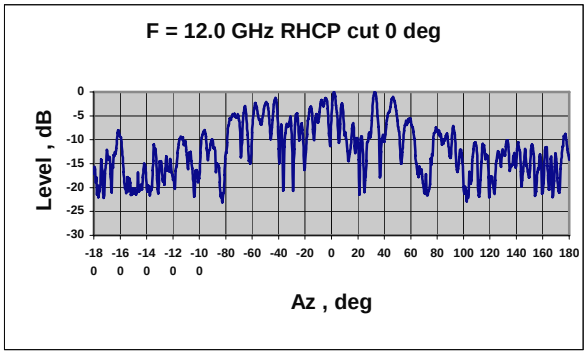

Figure 3. SCP cooperative pattern

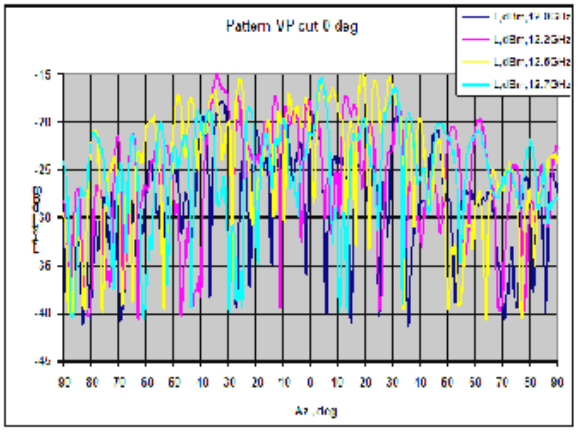

Figure 4. SCP cooperative pattern at different frequencies

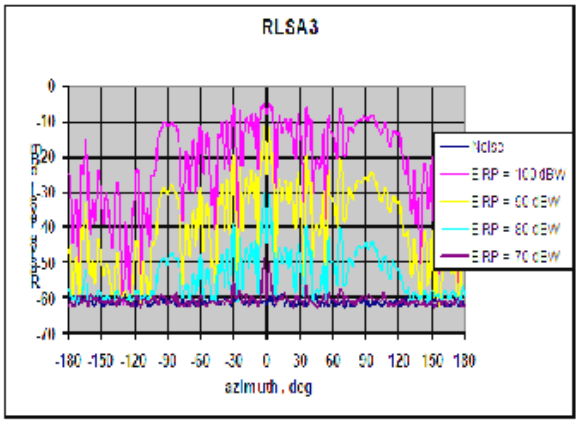

Figure 5. SCP cooperative pattern at different EIRP,s

The conclusions, based on the test results, could be summarized as follows:

- The cooperative pattern ripples are smaller than in the previous tests, but still they are significant. There were proposals for their origin, based on the existing strong mutual coupling phenomena among RLSA slots. Special investigation was held in SG for this reason. It included HFSS simulations and experimental tests of the mutual coupling between two slots in RLSA with different distances and mutual orientations. The results show that even in the worst case of parallel slots at distance half wavelength the coupling is low (-11 dB or lower).
- According to the paper [2], the SCP correlation matrix should be pure diagonal (which means smooth omnidirectional SCP cooperative pattern) in the case of AWGN channel environment. In the tests, described above, the level of the signal is several order higher that that of the receiver noise. For real satellite test it is necessary to support only several dB signal to noise ratio in the receiver, which is not convenient for measuring the shape of the cooperative pattern. The conclusion is that instead of the cooperative pattern, the system BER (at low signal to noise ratio and digital signal processing in the receiver) as function of the spatial angular coordinates should be measured. Such tests were not possible to be provided in SG test facilities.

3. NEAR FIELD TEST SET-UP

The objectives of the near field set test-up and trials were to measure the amplitude distribution, as well as the phase distribution of RLSA with random distributed and oriented slots (tangential, inclined and radial, fed by probes). The tests were performed in SG Near field test facility with standard equipment. The RLSA aperture – probe distance was 10 cm.

Hundred tests were performed in order to meet the objectives, mentioned above. The variable parameters in the different tests were:

- Frequency
- Slots lengths, coupling, distributions, inclinations and numbers
- RLSA high and permittivity

Some of the test results, provided by the Near Field set test-up, are shown in the figures below, as follows:

- Fig. 6. Near field amplitude distribution (LHCP, RLSA Φ 57 cm)
- Fig. 7. Near field phase distribution (LHCP, RLSA Φ 57 cm)

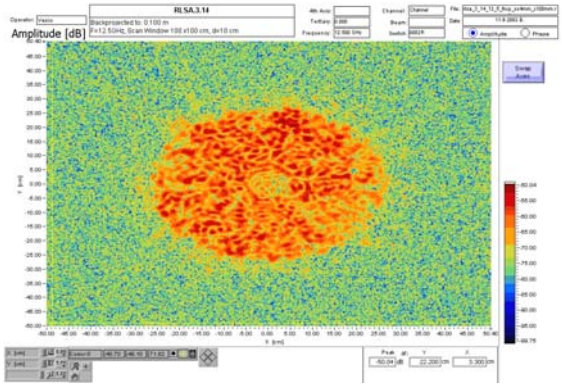

Figure 6. Near field amplitude distribution

The results, obtained in the last near field tests, show approximately uniform amplitude and random phase distributions in the RLSA aperture. The equipment resolution is less than half wavelength, which leads to not very correct results in the case of close distributed slots.

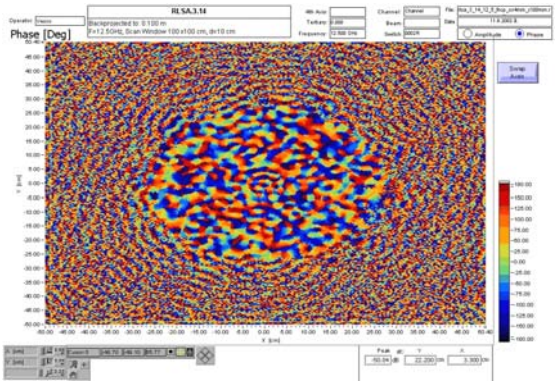

Figure 7. Near field phase distribution

References

[1] V. Demirev, "Review of SCP Test Set-up and Results - I", *CEMA,08 Conference Proceedings,* Athens, Grece, 2008.

[2] V. Demirev, A. Efremov, "SCP CDMA GSO,s system proposal", *ICEST, 04, Conference Proceedings,* pp.163-166, Bitola, Macedonia, 2004.

VISUAL DESIGN OF MOBILE ROBOT AUDIO AND VIDEO SYSTEM IN 2D SPACE OF OBSERVATION

Alexander Bekiarski, Snejana Pleshkova-Bekiarska

Technical University – Sofia, Bulgaria
St. Kliment Ohridski, 8
Tel.: +359 965 3300; E-mail: snegpl@tu-sofia.bg

Abstract

The mobile robot consists from a lot of subsystems. The main system is moving system, which is a combination of mechanical, electric and electronics parts. But the information, which control the movements the robot is collecting, processing from the sensors system. The most natural sensors in sense, that the mobile robot is similar to people, are audio and visual sensors. They are most informative between all mobile robot sensors, but it is very difficult to process and to separate with these sensors only the information useful for the movement of the robot.

This difficulty increase, if it is necessary to add the conditions and characteristics of the area or space of observation of the mobile robot. Therefore the goal of this article is to facilitate the design of audio and visual robot system with the developing a user friendly tool as a visual interface in the steps of simulation and modeling the audio and video robot system.

1. INTRODUCTION

The mobile robots perform the audio and visual information from the corresponding sensors [1], [6]. Most popular audio and video sensors are microphone arrays and video cameras. They are placed on the mobile robot moving device and collect the sounds and images from the robot space of observation respectively. Sounds are transformed from each of the microphones in the array as sound signals [2] and images from the video camera (or cameras in case of stereo robot vision) as video signals [3]. The main goals in the processing of sound and video signals are:

- to separate the signal of interest (SOI) from the combination of sound signals, received from microphone array (usually this signal is speech signal from a speaker talking to the robot in area or space of observation;
- to calculate or estimate the sound or speech signal direction of arrival (DOA) (this is a kind of sound localization);
- to separate the visual object from the received pictures (usually the speaker in space of observation);
- to calculate the position of separated visual object from the received pictures;
- finally, to joint the information as co-ordinates of speaker, calculated from audio and video system, and use this joined information for choosing the right direction for the control of the robot moving system.

Some or all of these mentioned tasks can be simulated separately or in combination, but in all cases exist the problem of a fast and simple modification of the characteristics of space or area of observation, room dimensions, mobile robot position, speaker places, etc. This mean, that it is necessary to have a tool in computer simulation programme, which gives a visual representation of robot space of observation with the possibility to interactive changes of room dimensions, robot and speakers places, etc. The simple case for design a visual interactive tool in simulation of a robot audio visual system is to represent the robot space of observation as a empty rectangle, i.e. as a 2D space of observation and then place in this rectangle the initial robot and speaker positions. This is the goal in this article.

2. VISUAL 2D REPRESENTATION OF ROBOT SPACE OF OBSERVATION

In general case the robot space or area of observation can be arbitrary, but here it is chosen to use an empty room as a concrete space of robot observation. It is also accepted to consider the room only in 2D dimensions length "l" and width "w". This assumption is applicable, because in most the cases the robot movements are on the room floor.

The proposed visual design of 2D space of observation of the robot is presented in Fig.1 as an algorithm of steps, which can be used first for the initial states settings and then as an interactive work in the current simulation of the audio and visual situation in area or space of robot observation. In the Fig.1 are shown only initial steps of the algorithm.

The first step of the algorithm is for the input of the room dimensions length "l" and with "w", which here are present as variables "roomI" and "roomw" in the algorithm. Then, for the visual representation on a screen, it is necessary to calculate the resolutions Nx and Ny of display in direction x and y (related for example with room length and width respectively). For these calculation, one of these relative and discrete dimensions Nx or Ny can be chosen, for example Nx = = 1024 to guaranty a good and precise resolution in x direction. Then it is defined the coefficient Kx as a relation between metric and discrete room dimensions:

$$K_x = \frac{roomI}{Nx}. \qquad (1)$$

The equation (1) can be used in the calculation of discrete room dimension Ny in direction y:

$$N_y = \frac{roomw}{Kx}. \qquad (2)$$

The chosen and calculated Kx from equations (1) and (2) discrete room dimensions Nx and Ny can be used for room drawing and displaying as an rectangle. The next step in the algorithm shown in Fig.1 allows interactive to choose the position of the robot in the room space, i.e. in the rectangle, which is already drawn. The interactive chosen robot position is represented in rectangle room space as robot co-ordinates xr and yr, respectively.

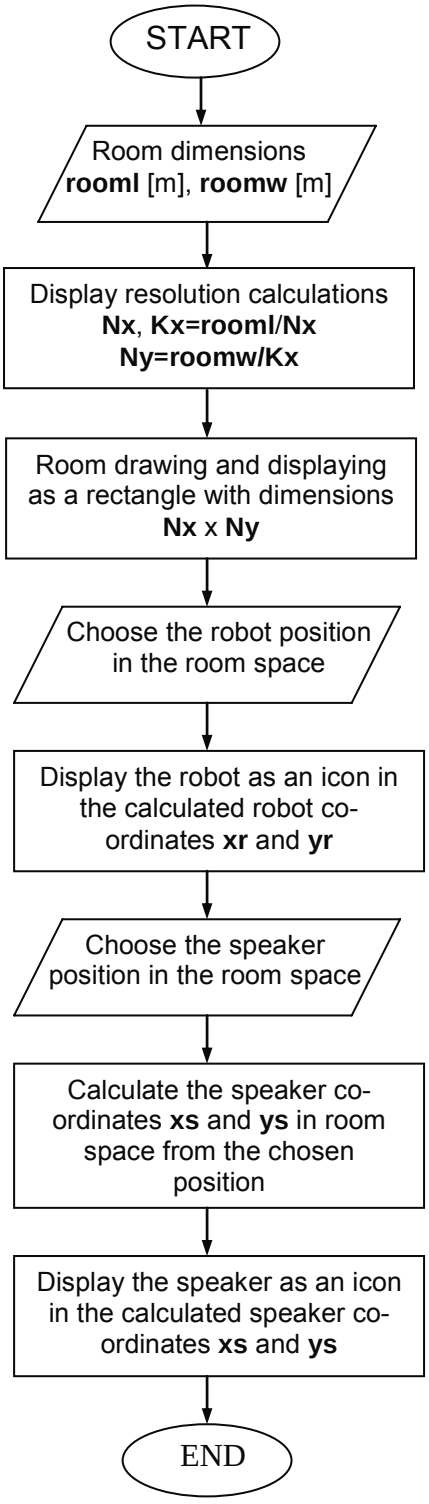

Fig.1. Initial state of algorithm

The visualization of the robot place in the area of room rectangle is made with an icon of an stylize and simplified image of a robot.

In the similar way the next steps of the algorithm shown in Fig. 1, are for an interactive choosing the speaker position in the space of rectangle of robot observation. Then this position is transformed after some calculations to the absolute speaker co-ordinates xs and ys in the space of robot observation. This is necessary to display the speaker as an initial place in the space of observation and on an appropriate distance from the robot position.

The results of the visual design algorithm in the steps of initialization are shown in Fig. 2.

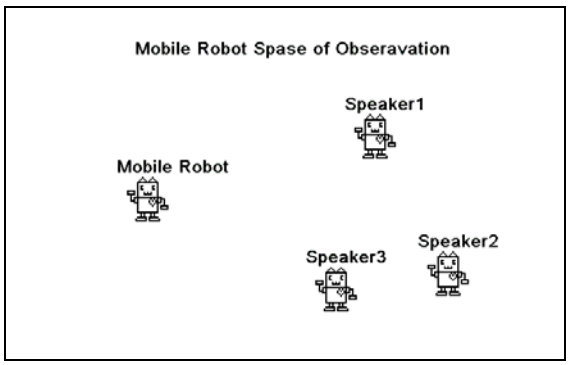

Fig. 2. Mobile robot space of observation

Of course, it is possible to extend the initial audio and visual situation in space of observation with more than one speaker (Speaker1, Speaker2, speaker 3 in Fig.2), choosing the additional positions for other speakers in the area robot observation. Also it is necessary to define the co-ordinates xm, ym of microphone array and the visual sensor xv, yv or video camera to be equal of the robot co-ordinates xr and yr in 2D space of observation representation:

$$xm=xr;\ xv=xr$$
$$ym=yr;\ yv=yr. \qquad (3)$$

When preparations of the initial stages are finished, the steps for preparing and calculating the audio and video system characteristics are performed.

For an audio robot system these characteristics are the number of microphones nmic in microphone array, the distance dm between microphones and length lmicar of microphone array, if it is chosen a linear array. The relations of these characteristics are expressed as:

$$Dm=lmicar/nmic. \qquad (4)$$

Also for a video robot system it is important to choose the type of video system: mono or stereo, the focus distance, the ability to change direction of observation, etc.

The initial step is followed by a concrete simulation or testing the work of the audio and video robot system. Each of two robot systems – audio and video execute at the same time different tasks. Audio system performs sound localization and calculates direction of talk to the robot. Video system, also process the images of the room to separate the place of the speaker. The results of the operation of audio and video systems are the direction of arrival and the co-ordinates of the speaker, which are calculated both from audio system [4]:

$$\theta_d = \frac{\sum_{\theta=1^0}^{360^0} R_{ij}\left[k(\theta)\right] x\theta}{\sum_{\theta=1^0}^{360^0} R_{ij}\left[k(\theta)\right]} \qquad (5)$$

and video system [5]

$$xs = \frac{\sum_{i=1}^{n} a_i x_i}{\sum_{i=1}^{n} a_i};\quad ys = \frac{\sum_{i=1}^{n} a_i y_i}{\sum_{i=1}^{n} a_i}, \qquad (6)$$

where

Θ_d is the angle of direction of arrival;

$R_{ij}[k(\Theta)]$ – cross correlation in received microphone array speech signals in relation to angle $\Theta=1^o \div 360^o$;

xs and ys – speaker coordinates, calculated from visual system;

x_i and y_i – current image co-ordinates;

a_i – the brightness value of current image point.

The equation (5) and (6) gives the final results from the work of audio and video system. They serve as audio and video information for the proposed here visual design and representation of moving robot audio and video system.

The interactive part of the visual design with simulation of audio and visual system operation is shown in Fig. 3.

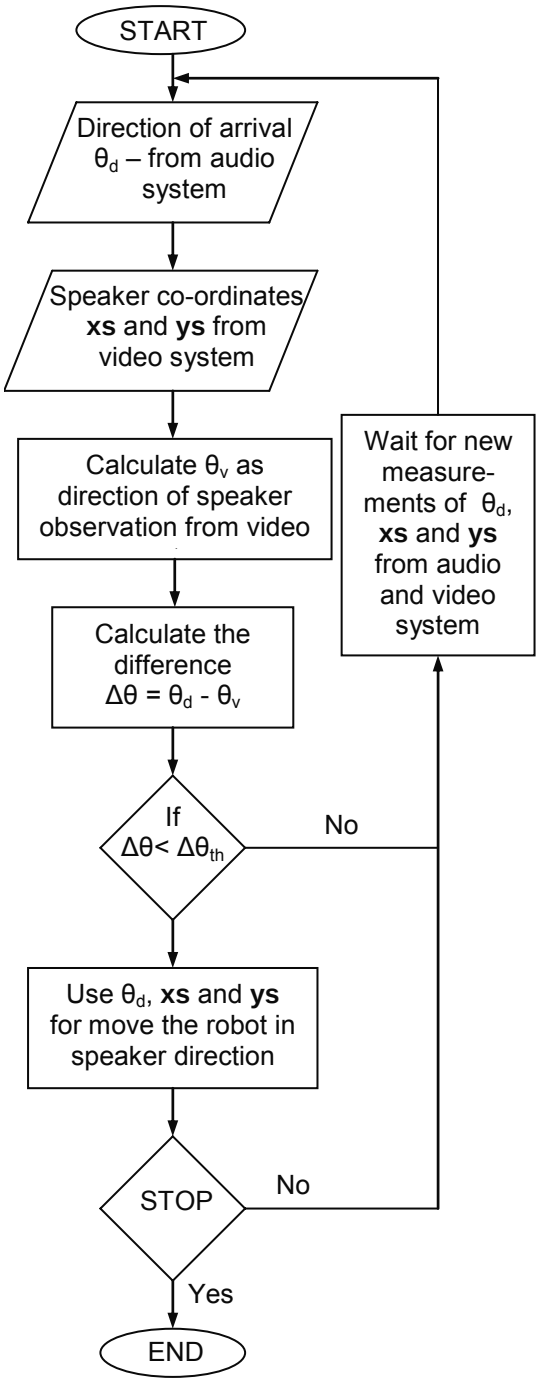

Fig. 3. Interactive state of algorithm

This part of algorithm start after the initial steps, described and shown in Fig.1.The current direction of arrival as angle θ_d is inputted as a result of work of audio robot system in the first step of algorithm in Fig. 3. Also the current speaker co-ordinates xs and ys are entered, which are derived form visual robot system. From these co-ordinates it is possible to calculate the speaker direction θ_v as:

$$\theta_v = \arcsin\frac{xs - xr}{ys - yr}. \qquad (7)$$

Two directions θ_d, calculated from audio system (equation (5)) and θ_v, calculated from video robot system (equation (6)), must be equal if both audio and video systems determine the exactly speaker position as a direction of robot observation. But in a real situation, each of these systems can calculate the direction with an error from the precise speaker position. Therefore, it is necessary to choose which of these two directions to use for move the robot or two directions are so much different, that it is not possible to use them.

This is shown in the next steps of algorithm in Fig. 3, when the difference $\Delta\theta$ between two angles θ_d and θ_v is calculated:

$$\Delta\theta = \theta_d - \theta_v. \qquad (8)$$

The decision of using or not the appropriate angles θ_d and θ_v in the action to move the robot in speaker direction is made after a comparison of difference $\Delta\theta$ with some practically chosen threshold $\Delta\theta_{th}$:

$$\Delta\theta < \Delta\theta_{th}. \qquad (9)$$

If the condition (9) is satisfied, then the step to move the robot in speaker direction is executed. This is accomplished first with an averaging to directions θ_d and θ_v:

$$\theta_{av} = \frac{1}{2}(\theta_d + \theta_v), \qquad (10)$$

to calculate an average direction $\Delta\theta_{av}$, and then to use this average direction in the action to move robot. This proposition can reduce or average the two possible existing errors of θ_d and θ_v determination from audio and video robot system, respectively.

If the condition (9) is not satisfied, then it is necessary to wait until a new measurement of

θ_d, xs and ys are performed from the audio and video robot system, respectively.

The iterative process to calculating the speaker direction and its co-ordinates from audio and visual system and moving the robot can be stop in a chosen moment for ending of the simulation.

3. RESULTS AND CONCLUSION

As an example of the work of the algorithm in Fig. 3 it is shown a situation in room with a robot and three speakers, when the Speaker1 is talking. The results of audio and video system actions are shown with different line styles for clearly separation of real direction (solid line), audio system direction of arrival determination (dashed line) and observation from video system the direction of Speaker1 (dotted line). Also in Fig. 4 are shown the values of angle (theta=60^o) calculated from equation (3) and Speaker1 co-ordinates xs1 and ys1, calculated from equation (4).

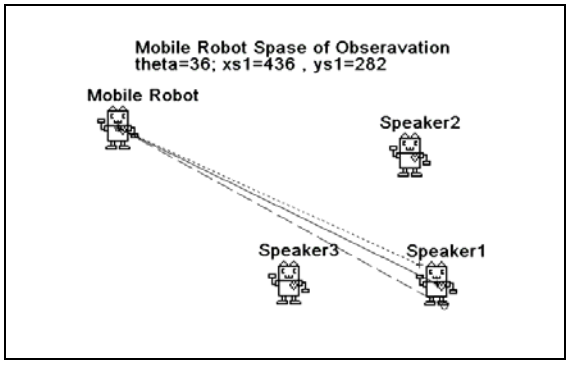

Fig. 4. Mobile robot space of observation after initial state

A full sequence of robot movement simulation in direction of the Speaker1 is shown in Fig. 5, where it is seen, as a sequence of points, some of the current robot positions, calculated from audio and video system in the movement of the robot to the Speaker1. These points are near as possible to the real direction to the Speaker1.

The presented work of the proposed visual design tool or interface for simulation and testing the ability of audio and video robot system shows, that this visual tool give good possibilities to express all steps: initial, interactive and final of the algorithm, in a very convenient form. Also this visual tool allows analysing the results for the working, capacity and efficient of the audio and video robot system. In the future works it is expected to extend the view and the capabilities of this tool for visual representation and interactivity in the real time working robot audio and visual system.

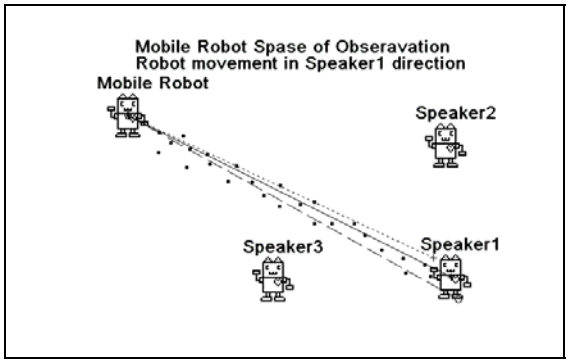

Fig. 5. Robot movement in Speaker1 direction

4. ACKNOWLEDGMENTS

This work was supported by National Ministry of Science and Education of Bulgaria under Contract BY-I-302/2007: "Audio-video information and communication system for active surveillance cooperating with a Mobile Security Robot".

References

[1] J. Fritsch, M. Kleinehagenbrock, S. Lang, G.A. Fink, and G. Sagerer. Audiovisual Person Tracking with a Mobile Robot. Proceedings of Biefeld University, Faculty of Technology, pp.207-216, Biefeld, Germany, 2007.

[2] D. Giuliani, M. Omologo, and P. Svaizer. Talker localization and speech recognition using a microphone array and a cross-power spectrum phase analysis. In Proc. Int. conf. on Spoken Language Processing, volume 3, pages 1243-1246, Yokohama, Japan, 1994.

[3] S. McKenna, Y Raja, and S. Gong. Tracking color objects using adaptive mixture models. Image and Vision Computing, 17, pp. 225-231, March 2006.

[4] Sn. Pleshkova, Al. Bekiarski. Sound Propagation Model for Sound Source Localization in Area of Observation of an Audio Robot. WSEAS.2008.

[5] M. Grau, Al. Bekiarski, P. Venkov, I. Nacheva. Robot Contol with Camera Eye. CEMA'07,Sofia, 2007.

[6] Milushev M., S. Hecht, T. Djamiykov Design of a Sensor for the Stepping Contact Force of a Walking Machine 53rd Internationales Wissenschaftliches Kolloquium - Technische Universität Ilmenau (53. IWK), 08 – 12 September, 2008 pp. 77-79.

SIMULATION OF AUDIO VISUAL ROBOT PERCEPTION OF SPEECH SIGNALS AND VISUAL INFORMATION

Alexander Bekiarski, Snejana Pleshkova-Bekiarska

Technical University – Sofia, Bulgaria
Kliment Ohridski, 8
Tel.: +359 965 3300; E-mail: snegpl@tu-sofia.bg

Abstract

Audio visual robots are intelligent robots that require many researches to gain the desired performance. An obligatory and necessary stage of these researches is simulation. In many articles for the moving robots there are simulations, but most of them investigate a small part of entire robot action or robot system. The goal in this article is to propose tests and simulation of the audio perception robot system with conjunction to the received visual information from the moving robot visual sensors. The achieved results from these simulations can be used in the future works to combine and improve the overall moving robot performances.

1. INTRODUCTION

Intelligent robots must involve audio and video sensors for perceiving the sounds in the area of observation [1] and also visual information [2]. The sound sources can be speech signals from the speakers. The robot perceives the speaker sounds, process them and determine the speaker localization or only determination of the direction of arrival (DOA) of sound [3]. Another more complicated task is the speech recognizing or speaker identification, performed from the robot to identified or recognized the talker and then to choose the moving direction [4] and [5].

The moving robot system must be designed correctly after multiple experiments and tests using real robot systems as designed tool, but in the beginning of tests it is suitable to use simulations of the proposed ideas, concepts and algorithms. In this article is proposed a method of simulation of moving robot audio perception system in conjunction with received video information. The steps of the proposed simulation are:

- speech source signal simulation as isolated words;
- speech sound waves propagation in area of robot observation taken as a room space;
- 2D room area of space of robot observation simulation;
- simulation of the types and the characteristics of robot audio and video sensors (linear, 2D microphone arrays, mono or stereo video cameras);
- simulation and test of speaker localization;
- calculation of speaker co-ordinates from video information;
- combining two information from speech signal localization and speaker co-ordinates etc.

2. SPEECH SOURCE SIGNAL SIMULATION

For the simulations of the received from the robot audio system speech signal are used speech source signals as words and sentences pronounced from the speakers man or woman. One of these chosen source signals is presented in Fig. 1 as an example of speech source signal of the pronounced word “Five”, part of the speech signals collected as a specific data base used these tests presented in this article for determine the best characteristics for audio system of a real moving robot with audio and video sensors.

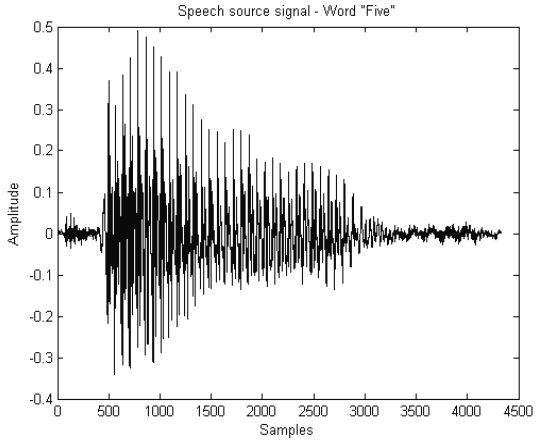

Fig. 1. Speech source signal – Word "Five"

For the simulation of speech signals, received from a set of microphones, which serves as robot audio sensors, it is necessary to define the space relations between speaker position S_p, the center "0" of the robot co-ordinate system and also the number and places of microphones situate on the moving robot.

3. SIMULATION OF 2D ROOM AREA OF SPACE OF ROBOT OBSERVATION

In the presented simulation it is chosen to use a circular 2D arrangement of microphone array. The number of the microphones is "n", chosen here as n=3, the simplest case (microphones M_1, M_2 and M_3), but can be more than n=3. Places of the microphones M_1, M_2 and M_3 are chosen with the appropriate 2D co-ordinates x_{M1}, y_{M1}; x_{M2}, y_{M2}; x_{M3}, y_{M3}. The co-ordinates and the positions of the microphones must be defined in a way that they are placed in the appropriate corners of an equilateral triangle, inside of a circle, and the place of the microphone M_1 is chosen to be in front of microphone array, i.e. in the direction of speaker source. The distance between speaker place S_p and the center of robot "0", defined as l_0, is placed in the center of gravity of the equilateral triangle. This distance is variable and depend from the current place and movements of the robot, but here it is and is kept constant, for example l_0=1 m. Only the angle between speaker position S_p and center of robot "0" is changed in the time of simulations.

4. SIMULATION AND CALCULATION OF SPEAKER LOCALIZATION

The angle θ_d between axis "y" and l_0 define the direction of speech sound source and can be calculated as:

$$\theta_d = \frac{\sum_{\theta=1^\circ}^{360^\circ} R_{i,j}[k(\theta)] \times \theta}{\sum_{\theta=1^\circ}^{360^\circ} R_{i,j}[k(\theta)]}, \quad (1)$$

where

$R_{i,j}[k(\theta)]$ - is the relation coefficient;

k – the number of actual delay smples between the speech signals received from microphones i and j respectively;

θ – the current value of the angle.

The relation coefficient $R_{i,j}[k(\theta)]$ can be calculated as correlation between appropriate pairs of speech signals S_i and S_j (i and j = 1,2,3), received from micro-phones M_1, M_2 and M_3 in the 2D circular microphone array placed in the moving robot:

$$R_{i,j}(k) = \frac{\sum_{m=0}^{N} S_i(m-k).S_j(m)}{\sqrt{\sum_{m=0}^{N} S_i(m-k)^2}.\sqrt{\sum_{m=0}^{N} S_m(m)^2}}, \quad (2)$$

where

N is the number of speech signal samples in a frame, defined usually as $N = 240$;

m – the current number of each speech signal sample.

5. SIMULATION OF THE RECEIVED MICROPHONE SIGNALS

Simulation of the speech signals S_i and S_j (i and j = 1,2,3) is made as a modification of the source speech signal from the talker. This modification means, that the speaker source speech signal is delayed with the different values for producing each microphone speech signal.

The values of the delays and displacements for each received from microphone speech signals are different and are calculated in discrete form or number of samples as:

$$n_1 = \frac{l_1}{c}.f_s;\ n_2 = \frac{l_2}{c}.f_s;\ ...; n_n = \frac{l_n}{c}.f_s;\ n_0 = \frac{l_0}{c}.f_s\ . \quad (3)$$

$$n_{1,2}=\frac{l_{1,2}}{c}.f_s;\ \ n_{2,3}=\frac{l_{2,3}}{c}.f_s;...;n_{n-1,n}=\frac{l_{n-1,n}}{c}.f_s;\ \ n_{n,1}=\frac{l_{n,1}}{c}.f_s;\quad (4)$$
$$n_{d_m}=\frac{d_m}{c}.f_s,$$

where

$n_1, n_2, ... n_n, n_0$ are the delays in discrete form for each microphone;

$l_1 = l_2 = ... = l_n = l_0$ - the corresponding distances of microphones from speaker;

$l_{1,2} = l_{2,3} = ... = l_{n-1,n} = l_{n,1} = d_m$ are the distances between each pair of microphones;

c - velocity of sound in the air;

f_S - speech signal sampling frequency.

Equations (3) and (4) are presented in general form, i.e. multiple microphones, but in this simulation it is considered the case for n=3 as the number of microphones. Also, without breaking the defined space conditions, in the beginning of each simulation, it is possible to vary be distances between three microphones $l_{1,2}$, $l_{2,3}$ and $l_{3,1}$, defined in equation (4), but keep them equal, i.e. $l_{1,2}=l_{2,3}=l_{3,1}=d_m$. Here in Fig. 2. are shown the simulations for the received microphone signals with the distance d_m =0,2 m between three microphones, but it can be changed, for example between 0,1 and 0,6 m, or more.

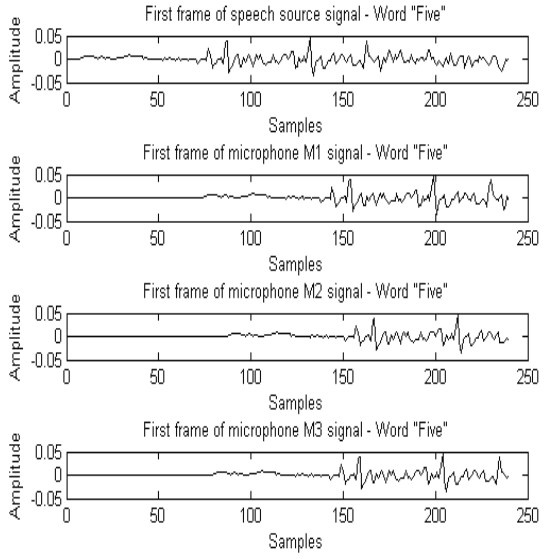

Fig. 2. First frames of speech signals of the pronounced word "Five" in appropriate places of the space of robot area of observation

From equation (4) it is clear, that increasing distance d_m leads to large value on $n_{1,2}=n_{2,3}=n_{3,1}=d_m$, representing the distance between the microphones as number of samples. Finally this gives more precision in simulation, when calculating the angle θ_d, which represent the sound direction of arrival.

6. RESULTS OF ROBOT AUDIO SYSTEM SIMULATIONS

The described parts of an audio system are first simulated separately for verify their correct works.

Then all of these parts are connected together in an simulation algorithm to test and simulate the whole work of the audio robot system. In this simulation are used the equations presented here. The main goal is to prove with the appropriate measurements and calculation in the time of simulation the proposed method for speech source localization.

Here are presented some conditions for these simulation.

As an area of robot observation is used a 2D model of a room with following dimensions: length of the room larea = 10 m and width of the room varea = 5 m. The speaker position S_p is defined and varied with choosing the coordinates x_{sp} and y_{sp}, according to the origin of the coordinate system placed at the center of robot "0". There are simulated many concrete situations of 2D area of robot observation space or room. In this space it is chosen an 2D (x,y) coordinate system with origin point "0" in the center of an 2D microphone array M_1, M_2, M_3,…, M_n, placed on the moving device of the robot.

One of the most important goal of an audio robot system is to find and estimate the sound source direction and localization. In most practical cases it is enough to estimate the sound source direction of arrival of speech from speaker or talker. In a chosen situation of simulation it is necessary to choose the range of variation of k (equation 1), for calculated the relation coefficients $R_{1,i}$ (k). Here it is chosen the changes of angle θ between axis y and the direction l_0 of sound source or speaker place from 0^0 to 360^0 and to keep the distance between robot center "0" and speaker place constant (l_0=const). In this

case the range of variation of actual delay k as number of samples depend on actual differences between distance l_1 and each distance l_2, l_3, …, l_n of the microphones M_1, M_2, M_3, …, M_n from speaker place S_p. For changes of angle $\theta=0^0 \div 360^0$ these distance range from:

$$l_{1d}^{\min} = \min\left(-l_{1,i}\right) \text{ to } l_{1d}^{\max} = \max\left(l_{1,i}\right), \quad (5)$$

for i=1,2,…, n, which correspond to earlier/later sounds enters for microphones M_2, M_3, …, M_n toward microphone M_1. Actually for this simulation n=3.

More precisely, from equations (3) and (4), it is possibly to represent the range of variations of actual delay k as number of samples:

$$k_{\min} = \frac{l_{1d}^{\min}}{c}.f_s = \frac{\min\left(-l_{1,i}\right)}{c}.f_s \quad (6)$$

$$k_{\max} = \frac{l_{1d}^{\max}}{c}.f_s = \frac{\max\left(l_{1,i}\right)}{c}.f_s \quad \text{for } i = 1,2,...,n. \quad (7)$$

Under these circumstances, the range of variations of k from k_{min} to k_{max} can be described as a function of angle θ k(θ), for $\theta=0^0 \div 360^0$.

The last representation of k gives the reason to describe the relation coefficients $R_{1,i}(k)$ from equation (5) also as a function of angle θ in the range of $0^0 \div 360^0$, that means $R_{1,i}$ [k(θ)]. Therefore, the sound or speaker direction can be estimated from the matrix of cross correlation of $R_{1,i}$ [k(θ)] and $R_{1,j}$ [k(θ)]:

$$R_{i,j}\left[k(\theta)\right] = R_{1,i}\left[k(\theta)\right].R_{1,j}\left[k(\theta)\right] \quad (8)$$

$$\text{for } i = 1,2,...,n;\ i \neq j \ \text{ and } \theta = 1^\circ, 2^\circ, ..., 360^\circ.$$

From the equation (8) it is possible to find the maximum of cross correlation:

$$R_{\max} = \max\left\{R_{i,j}\left[k(\theta)\right]\right\}. \quad (9)$$

Also it is proposed to define a threshold value R_t from the maximum of cross correlation:

$$R_t = 0{,}99 \,.\, \max\left\{R_{i,j}\left[k(\theta)\right]\right\}. \quad (10)$$

The threshold R_t from equation (10) is used to perform normalization to the cross correlation $R_{i,j}$ [k(θ)]:

$$R_{i,j}\left[k(\theta)\right] = 0, \text{ if } R_{i,j}\left[k(\theta)\right] < R_t$$

$$R_{i,j}\left[k(\theta)\right] = \frac{R_{i,j}\left[k(\theta)\right] - R_t}{R_{\max} - R_t},$$

$$\text{If } R_{i,j}\left[k(\theta)\right] \geq R_t \quad (11)$$

for θ = 1°, 2°,…, 360°

These conditions and calculations are used in simulation and allow to perform a weighted average to the $R_{i,j}$ [k(θ)] from equation (11), which allow to find from equation (1) the correct value of angle θ_d as a sound or speaker direction. for the cases, where there are not reverberations, noise signals or words with consonants, that have weakly periodic signals. But these cases are not a real situation for the moving robot. Therefore, in order to find accurate determination of sounds direction of speech signals, it is possible to determine and calculate sound direction only at the speech signal frame that has the maximum energy within a period of speech signal.

The lots of simulations with the proposed robot audio system shown, that on the range of all angles ($1^0 \div 360^0$), the difference between magnitudes of the cross correlation is very informative to assist in finding reliable detection of the sounds direction.

After these definitions and presentation of some equations, from which it is possible to find, in the time of simulation, the direction of arrival of the sounds from the speaker it is possible to use them to make the tests and examinations to confirm the correctness of the proposed moving robot audio system simulation. If this correctness existed, there are the reasons to apply these methods and operations in a real moving robot system.

Each simulation is then executed, after the definitions of all of these necessary conditions. Some results are shown here and they represent the steps of testing the chosen operations for speaker direction finding, using the proposed moving robot audio system. On the Fig.2 are presented the time relations between speech source signal and the simulated signals S_1, S_2 and S_3 from the microphones M_1, M_2 and M_3. Comparing the first frames of each of four sig-

nals, it can be seen, that in the simulation it is realized a suitable time delay between speech source signal and the simulated received microphone signal.

The signal from microphone M_1 have some time delay, measured toward source speech signal, the signal from microphone M_3 some additional time delay, toward signal from microphone M_1 and the signal from the microphone M_2 have the time delay, toward the signal from microphone M_3. This means, that the speaker place in this simulation is chosen in such a way, that the distance of microphone M_3 to speaker place is smaller, than the distance of microphone M_2. In the next step of simulation are calculated, using the equations (2), two relation coefficients $R_{1,2}$ and $R_{1,3}$ between speech signal from microphones M_1, M_2 and between speech signal from microphones M_1, M_3, respectively.

These relation coefficients are presented on Fig. 3. On the Fig. 3 are seen the maximum values in each of the relation coefficients. These maximums confirm the existing of peaks in the correlation coefficients, which depend from the relative time delay between signal from microphones M_2 and M_3, respectively.

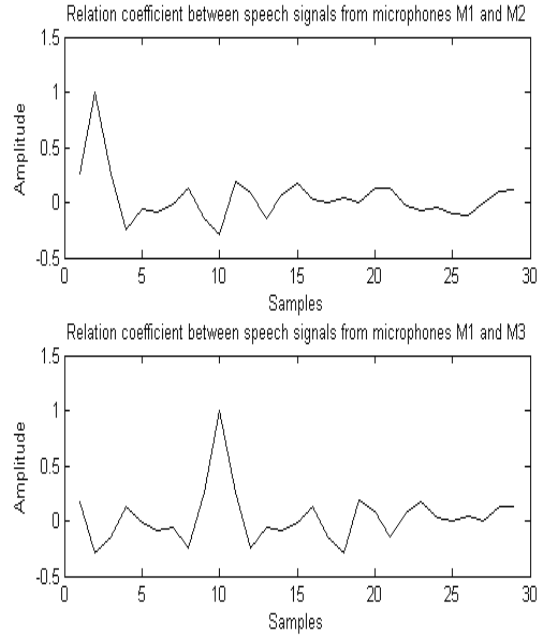

Fig. 3. Relation coefficients between speech signals from microphones

This gives the reason to calculate the matrix of cross correlation $R_{i,j}$ using equation (8) and then to make the normalization of the cross correlation using equations (9), (10) and (11). The results from these operations are shown in Fig. 4.

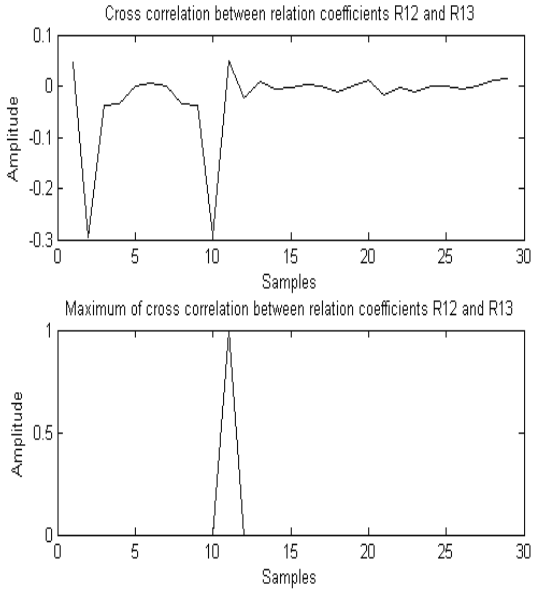

Fig. 4. Cross correlation between relation coefficients

The maximum value, which can be determined from the Fig.5, is equal to 11 and it is expressed as number of samples. Using equation (12) in the simulation it is possible to transform this value from the number of samples to value in degrees, i.e. to determine the value of angle θ_d, which gives the direction of sound arrival. Using value 11, calculated as number of samples, gives after transformation with equation (12) an angle $\theta_d = 23^0$.

7. CONCLUSION

The proposed simulation and the results, presented as the steps of simulation, using some proposed equations demonstrate the correct work of the operations and calculations of each step of the simulation to determine the angle θ_d, describing the direction of arrival of the sounds from the speaker to the robot. All of these steps are simulated and tested separately and then as an entire algorithm to test the relation between each step.

In the future works these results will be combined with the results from the simulation of the video sensor robot system, which give as the results the co-ordinates of speaker or talker

calculated after their visual identification from the visual robot perception system.

ACKNOWLEDGMENT

This work was supported by National Ministry of Science and Education of Bulgaria under Contract BY-I-302/2007: "Audio-video information and communication system for active surveillance cooperating with a Mobile Security Robot".

References

[1] W.K. Ma, B. N. Vo, S. Singh, "Tracking in Onknown Time-Varying Number of Speakers using TDOA Measurements: A Random Finite Set Approach", IEEE Trans. on Signal Proc., vol.54, No9, 1993, pp. 3291–3296, Sept. 2006.

[2] J. Fritisch, M. Kleinehagenbrock, S. Lang "Audiovisual person tracking with a mobile robot", in Proc. Int. Conf. on Intelligent Autonomous System, pp. 898-906, IOS Press, 2004.

[3] H. Savada, R. Mucai, S. Araki,"Direction of arrival estimation for multiple source signals using independent component analysis", Proc. ISSPA, Paris, France, 2003.

[4] J. M. Valin, F. Michaud, B. Hadjou, "Localization of simultaneous moving sound sources for mobile robot using a frequency-domain steered beam former approach", IEEE Proc. Robotics and Automation, pp.236-242, 2002.

[5] A. Master, "Speech spectrum modeling from multiple sources", Master Thesis, Cambridge University, Engineering Department Cambridge, England, 2005.

MATHEMATICAL SIMULATION PROGRAM OF DOPED SI OXIDATION IN NANO-DIMENSION SCALE

T. Kersys, R. Anilionis, D. Eidukas

Department of Electronics Engineering, Kaunas University of Technology,
Studentu str. 50, LT-51368 Kaunas, Lithuania
Fax.+37037454498; E-mail. danielius.eidukas@ktu.lt.

Abstract

Micro and nano-electronic structures are the main components of all electronic devices today. Requirements of precision and reliability are applying for medicine electronics. Therefore micro and nano-semiconductor structures must be formed with high accuracy.

The fabrication of microelectronic structures vitally depends on the thermal oxidation for the formation of gate dielectrics, device isolation. Particularly, the precise control of silicon dioxide thickness as device geometries continues to scale to nano dimensions [1].

In semiconductor manufacturing process observed that thickness of SiO_2 layer getting uneven when oxidizing doped Si areas by various dopants. It was defined that boron, phosphorus, arsenic determinate SiO_2 formation in thermal oxidation technological process [2].

Dimension is very important parameter in nano-technologies therefore doping dependent oxidation makes additional problems when forming nano-structures.

By using mathematical simulation program ATHENA was performed mathematical simulation of Si thermal oxidation, and was evaluated the Si substrate doping dependent oxidation.

1. DOPING DEPENDENT OXIDATION

Experimental results explain that SiO_2 formation on highly-doped n-type and p-type substrates can be enhanced compared to SiO_2 formation on lightly-doped substrates. The dependence of silicon dioxide growth kinetics on doping concentration is manifested as part of the linear rate constant, where the physical significance of the high doping levels has been explained primarily as an electrical effect. This factor in the linear rate constant is given by:

$$\left(\frac{B}{A}\right)_{doping} = \left[1 + B_{K0} \cdot \exp\left(\frac{-B_{FE}}{k_b T}\right) \times \left(V^* \frac{V^*}{V_i^*}\right)\right] \quad (1)$$

where V* is the equilibrium vacancy concentration in silicon at the Si/SiO_2 interface. Vi* is the equilibrium vacancy concentration in intrinsic silicon. B_{K0} and B_{KE} relates to the doping dependence of the oxidation rate.

The equilibrium vacancy concentration, composed of vacancy defects in different charged states, depends on the Fermi level location and is given by:

$$V^* = V_i^* \left\{ \frac{1 + \left(\frac{n_i}{n}\right)\phi^+ + \left(\frac{n_i}{n}\right)^2 \phi^{++}}{1 + \phi^+ + \phi^{++} + \phi^- + \phi^=} + \right. \quad (2)$$
$$\left. + \frac{\left(\frac{n}{n_i}\right)\phi^- + \left(\frac{n}{n_i}\right)^2 \phi^=}{1 + \phi^+ + \phi^{++} + \phi^- + \phi^=} \right\}$$

where n is the electron concentration and n_i is the intrinsic carrier concentration, and φ+, φ++, φ−, and φ= are fractions of the vacancy concentration which are positively, double positively, negatively, and double negatively charged respectively.

Figure 1 shows a plot of at for common silicon dopants. Notice that for n-type dopants

(V^*/V_i^*) increases as the doping concentration increases, but V^*/V_i^* remains essentially constant for the p-type dopant. The increase in V^*/V_i^* for n-type dopants increases the linear rate constant. This ultimately leads to thicker oxides when oxidizing highly-doped n-type substrates due to a higher availability of unoccupied silicon lattice sites (vacancies) for oxidant molecules to be incorporated.

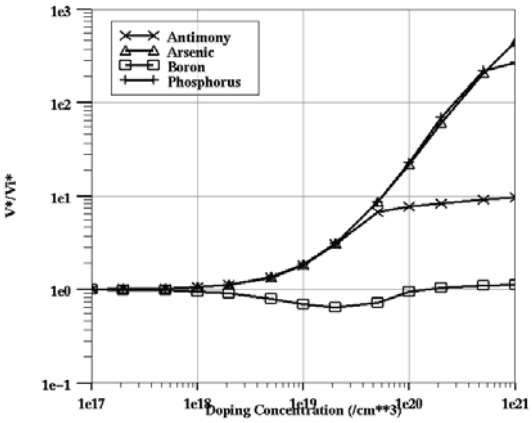

Figure 1. Simulated V/V_i ratio versus doping concentration

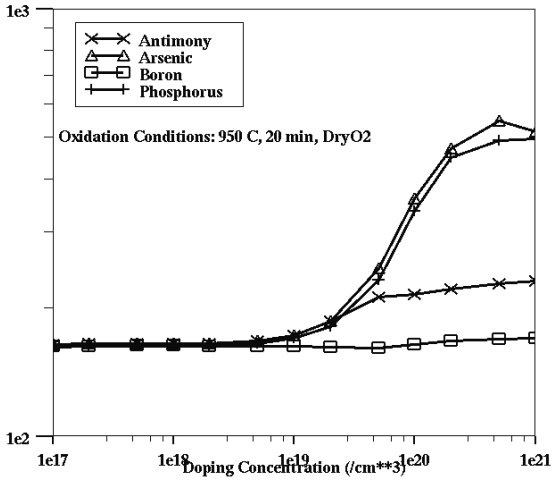

Figure 2. Simulated silicon dioxide thickness vs. doping concentration for common silicon dopants

The oxide thickness trend is shown in figure 2, where the SiO_2 thickness is plotted versus doping concentration for common silicon dopants [3].

2. OXIDATION OF EQUAL SI SUBSTRATE

By using mathematical simulation program ATHENA was performed mathematical simulation of oxidation technological process of undoped Si substrate and phosphorus doped Si substrate. Mathematical simulation results presented at 3 – 6 figures.

Ion implantation technology was used to dope Si by phosphorus. To analyze dopants influence to SiO_2 formation, it was doped one side of Si substrate by using Si_3N_4 mask. Ion implantation dose is $3 \cdot 10^{15}$ C/cm^2, energy – 10 keV. Ion implantation mathematical simulation results presented at figure 4. Mathematical simulation results (Fig. 4) demonstrate that phosphorus dopants concentrate at right corner of Si substrate.

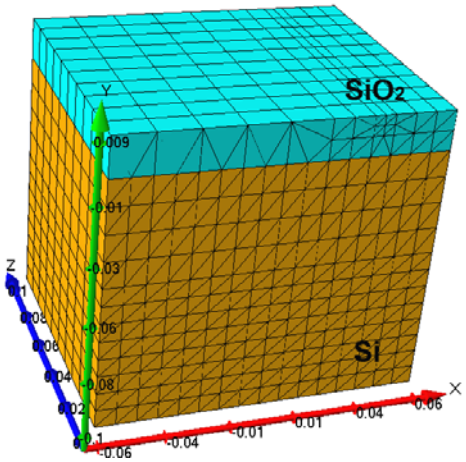

Figure 3. Undoped Si oxidation: oxidation time – 1min., temperature - 1000 ^oC, ambient – wet O_2

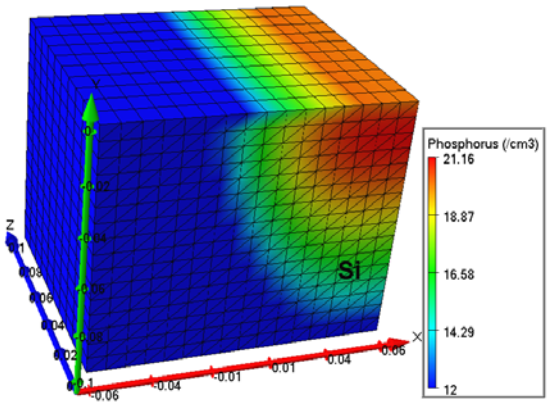

Figure 4. Phosphorus implantation in to Si substrate: ion implantation dose – $3 \cdot 10^{15}$ C/cm^2, energy – 10 keV

Next step – Si surface oxidation in wet O_2 ambient. Oxidation reaction time is 1 min., temperature – 1000 °C. Mathematical simulation results presented at figure 5.

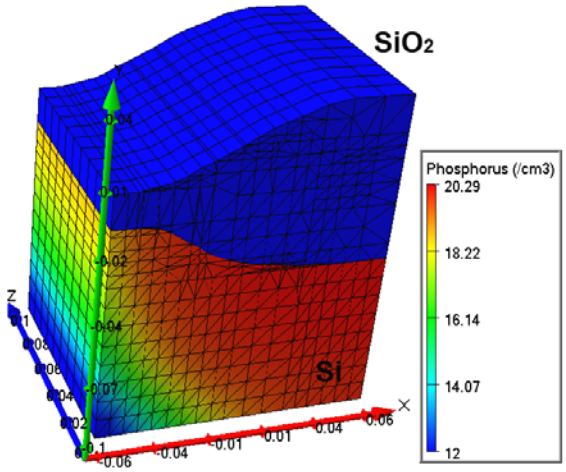

Figure 5. Phosphorus doped Si oxidation: oxidation time – 1min., temperature - 1000 °C, ambient – wet O_2

Figure 6 demonstrate comparison of mathematical simulation results of phosphorus doped and undoped silicon oxidation.

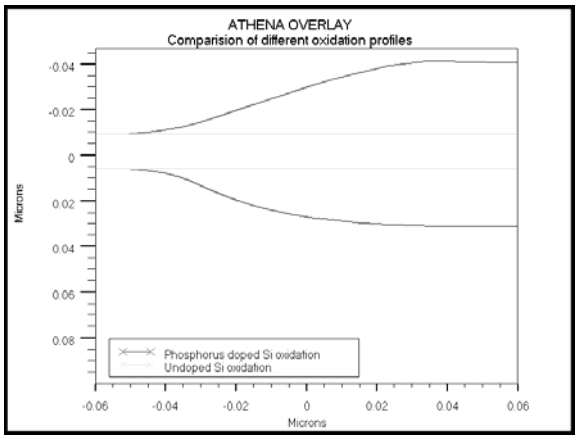

Figure 6. Undoped and phosphorus doped Si oxidation results comparison

During oxidation growing SiO_2 expand up and deep in to Si substrate. This effect is very important in integral elements forming technological process.

Mathematical simulation results demonstrate (Fig. 3-6), that dopant in Si substrate influent to SiO_2 growing form and to SiO_2 layer thickness – very important parameter. After phosphorus doped Si oxidation process formed SiO_2 thickness is ~ 60nm bigger than oxidizing undoped Si.

3. OXIDATION OF SI SUBSTRATE WITH Si_3N_4 MASK

Local oxidation of silicon (LOCOS) is using to isolate one integral element from another. By using Si_3N_4 mask LOCOS oxide is forming in the certain areas of Si substrate. In the course of Si oxidation oxygen molecules penetrate under the masking Si_3N_4 layer, therefore surface becomes uneven. Irregularities are rather high, up to 0.3-0.6 μm. Irregularities themselves do not increase metallization defects, however, they lift Si_3N_4 causing cracks in it as well as impede the photolithography deposition process [5].

Inequalities of the surface getting very important in nano dimension scale because thickness of deposited layers is very small and in this case arising number of defects in the deposited layer (Fig. 7)

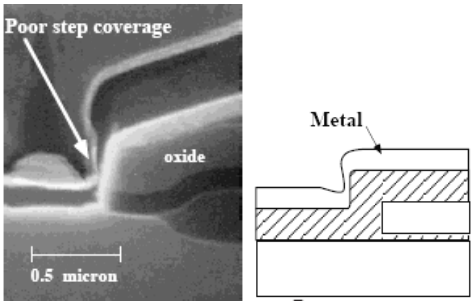

a) b)

Figure 7. Metal deposition defect [5]

Simulation of oxidation technological process of Si substrate with Si_3N_4 mask it was performed by using mathematical simulation program ATHENA. In first of all it was performed undoped Si oxidation (Fig. 8) and then phosphorus doped Si oxidation (Fig. 10) to investigate the Si dopants influence to oxidation.

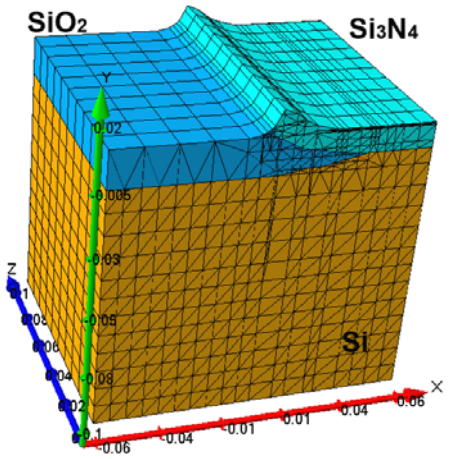

Figure 8. Boron doped Si substrate oxidation with Si_3N_4 mask: oxidation time – 1min., temperature - 1000 °C, ambient – wet O_2

Ion implantation technology was used to dope Si by phosphorus (Fig. 9). Ion implantation dose is $3 \cdot 10^{15}$ C/cm^2, energy – 10 keV. The less ion implantation energy is using to form nano-structures.

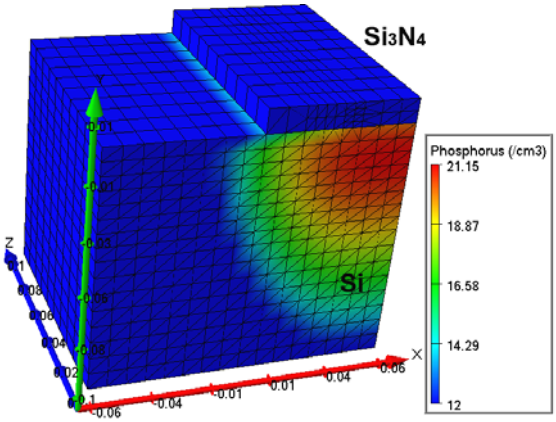

Figure 9. Phosphorus implantation in to Si substrate: ion implantation dose – $3 \cdot 10^{15}$ C/cm^2, energy – 10 keV

Impurities diffuse from high-doped regions to adjacent layers then performing oxidation. Mathematical simulation results in figures 9 and 10 demonstrate that phosphorus diffuse in to adjacent areas of Si substrate. This effect is very important when need to form p-n junctions in the particular depth [6].

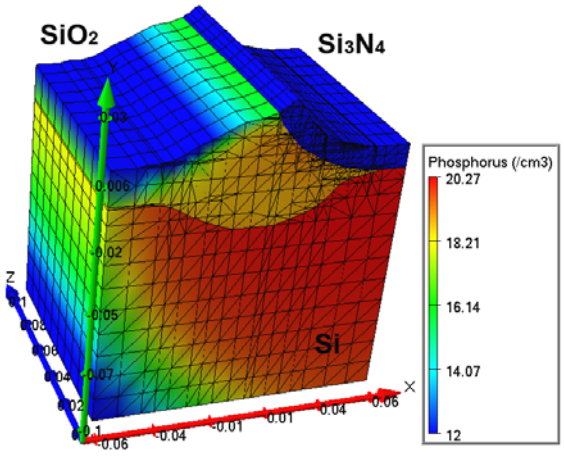

Figure 10. Phosphorus doped Si oxidation with Si_3N_4 mask: oxidation time – 1min., temperature - 1000 °C, ambient – wet O_2

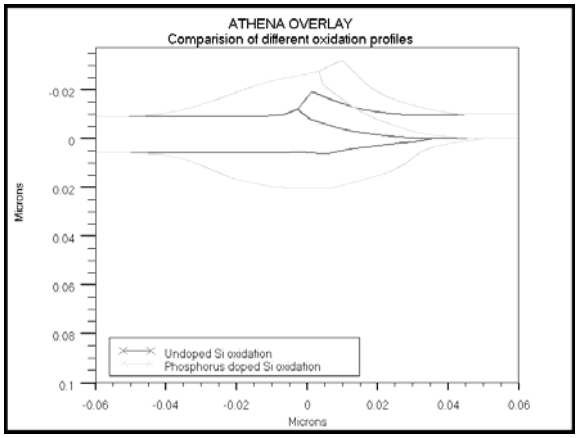

Figure 11. Undoped and phosphorus doped Si with Si_3N_4 mask oxidation results comparison

Mathematical simulation results of doped and undoped Si with Si_3N_4 layer oxidation (Fig. 11) demonstrate that dopants in the Si substrate accelerate SiO_2 forming process and also accelerate SiO_2 drift under the Si_3N_4 mask. Therefore growing SiO_2 form is changing markedly, surface becomes uneven. Irregularities of surface can reach ~ 40nm.

To prevent thermal diffusion of impurities it is purposeful in first of all to use thermal oxidation and then Si doping. In first of all Si substrate was oxidized in wet O_2 ambient 1 min at 1000 °C temperature. After that it was performed phosphorus doping by using ion implantation. Mathematical simulation results presented at figure 12.

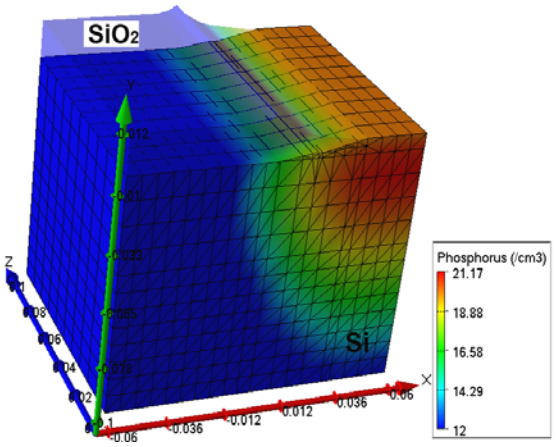

Figure 12. Phosphorus doped regions forming in to oxidized Si substrate: ion implantation dose – $3 \cdot 10^{15}$ C/cm^2, energy – 10 keV

Comparison of simulation results in figures 8, 9, 10 and 14 demonstrate that more acceptable results obtaining then in first of all are using thermal oxidation and doping process after that. It is avoiding thermal diffusion of impurities and dopants influence to SiO_2 forming process. The surface of formed structure is smoother, therefore number of defects in deposited layer decreasing.

4. CONCLUSIONS

Inequalities of the surface are very important in nano dimension scale because thickness of deposited layers is very small and in this case arising number of defects in the deposited layer.

Dopant in Si substrate influent to SiO_2 growing form and to SiO_2 layer thickness – very important parameter. Dopants in the Si accelerate SiO_2 forming. After phosphorus doped Si oxidation process formed SiO_2 thickness is ~ 60nm bigger than oxidizing undoped Si. Surface of the structure becomes uneven and irregularities of surface can reach ~ 40nm.

To prevent dopants influence to SiO_2 growing and thermal diffusion of dopants it is purposeful in first of all to use thermal oxidation and then Si doping. The surface of formed structure obtaining smoother, therefore number of defects in deposited layer decreasing.

References

[1] Marcinkevičius A. J. Integral elements design. Vilnius Gediminas Technical University. - Vilnius: Technique, 2004.

[2] Stephen A. Campbell. The Sciences and Engineering of Microelectronic Fabrication. New York: Oxford University Press; 2001. p. 83 - 86.

[3] ATHENA user manual. Official Website of SILVACO International. Internet. ttp://www.silvaco.com [02/02/2008]

[4] Eidukas D, Anilionis R, Kersys T. Simulation of LOCOS Technology // Proceedings of the 18-th International Conference on Production Research; 2005 July 29 – August 2; Fisciano [SA], Italy. Salerno: University of Salerno; 2005. p. 163.

[5] Physics and Modelling of VLSI Fabrication Courses. Internet. http://dunham.ee. washington.edu [02/02/2007]

[6] Keršys T., Andriukaitis D., Anilionis R. VMOS, UMOS Technology Simulation // 28-th International Conference Information Technology Interfaces (ITI 2006). - University of Zagreb, University Computing Centre, Cavtat / Dubrovnik, Croatia. – 06 19 – 06 22 2006.

INVESTIGATION OF ETCHING PROCESS AND DIFFERENT CRYSTALLOGRAPHIC PLANE ORIENTATION DEPENDENCE MATHEMATICAL SIMULATION IN NANO SCALE STRUCTURES

D. Andriukaitis, R. Anilionis

Department of Electronics Engineering, Kaunas University of Technology,
Studentu str. 50, LT-51368 Kaunas, Lithuania
E-mail: darius.andriukaitis@ktu.lt

Abstract

Problems of etching process, related with MOS transistors separation in SOS technology was researched. Integral circuit and their elements must be released with high precision. After a photo mask has been created a layer under the resist is etching. Wet Etching provide a higher degree of selectivity than dry etching techniques. In isotropic etching materials are removed uniformly from all directions. A vertical profile can be easily made using anisotropic etching and it solves the problem of lateral etching. Using dry etching it is much easier to start and stop than simple immersion wet etching and less lateral encroachment is achieved. The main avantage of ion milling is directionality. That's why less lateral encroachment during region formation could be achieved using ion milling according to wet and dry etching process simulation results. Also relationship between etching process and crystallographic planes orientation are analyzed, because etch rate is different using different crystallographic planes orientations.

1. INTRODUCTION

Integral circuit (IC) and their elements must be released with high precision. The IC made modern day information processing and communications systems possible. It's basic functional element is the transistor, most commonly a silicon metal oxide semiconductor field-effect transistor (MOSFET). In MOS/CMOS structures regions between the active elements must be isolated [1]. That's why etching process is important to IC formation. Choosing correct type of etch is possible to avoid disasters like: lateral encroachments, undesirable dislocations, bird's beak (in thermal oxidation).

Etching process described by etch rate – dimension of thickness per unit. A large etch rate is like advantage in technological process. Too high an etch rate is treat like lack, because it is difficult to control etching process. Etch process rate can reach hundreds nanometers per minute by common way [2, 3, 4].

Every technological process holds on MOS transistors or IC less or more. Every technological process related with past one (for example: diffusion depends on wafer (crystal lattice) quality, which depends on technological process temperature) [5].

2. VERY-LARGE-SCALE INTEGRATION

Early ICs of the late 1950s consisted of about 10 components on a chip 3 mm square. Very large-scale integration (VLSI) vastly increased circuit density, giving rise to the microprocessor. The first commercially successful IC chip (Intel, 1974) had 4,800 transistors; Intel's Pentium (1993) had 3.2 million, and more than a billion are now achievable [3]. VLSI is the process of creating integrated circuits by combining thousands of transistor-based circuits into a single chip [6]. The microprocessor is a VLSI device.

In micro/nanofabrication, in addition to thin film etching, very often the substrate also needs to be removed in order to create various mechanical micro-/nanostructures. Two important figures of merit for any etching process are selectivity and directionality. Selectivity is the degree to which the etchant can differentiate between the masking layer and the layer to be etched. Directionality has to do with the etch

profile under the mask. In an isotropic etch, the etchant attacks the material in all directions at the same rate, creating a semicircular profile under the mask. In an anisotropic etch, the dissolution rate depends on specific directions, and one can obtain straight sidewalls or other non-circular profiles. Also it is possible divide the various etching techniques into wet and dry categories.

3. ETCHING TECHNIQUES

3.1. Wet Etching

Wet etchants are by and large isotropic and show superior selectivity to the masking layer compared to various dry techniques. In addition, due to the lateral undercut, the minimum feature achievable with wet etchants is limited. Silicon dioxide is commonly etched in a dilute. Photoresist and silicon nitride are the two most common masking materials for the wet oxide etch. Nitride wet etch is not very common, due to the masking difficulty and unrepeatable etch rates.

Anisotropic and isotropic wet etching of crystalline and non-crystalline substrates are important topics in micro/nanofabrication.

For short etch times, silicon dioxide can be used as the masking material. However, one needs to use silicon nitride if a longer etch time is desired.

3.2. Dry Etching

Most dry etching techniques are plasma-based. They have several advantages compared with wet etching. These include smaller undercut (allowing smaller lines to be patterned) and higher anisotropicity (allowing high-aspect-ratio vertical structures). However, the selectivity of dry etching techniques is lower than the wet etchants, and one must take into account the finite etch rate of the masking materials.

The three basic dry etching techniques, namely, high-pressure plasma etching, reactive ion etching (RIE), and ion milling utilize different mechanisms to obtain directionality.

4. MOS TECHNOLOGICAL PROCESS

To improve MOS structure parameters parasitic capacities: gate-source, gate-drain has to be returned to minimum. In order to reduce parasitic capacities we must avoid lateral diffusion, the size of gate electrode must be the same during all technological processes in order to avoid source-drain channel shortening. The area of element formation must be the same during all technological processes. Separation of MOS elements can be produced using local oxidation [7] and silicon on sapphire technologies.

Thermical grown silicon oxide separates semiconductor elements. It is necessary to get hole with less lateral etched side wall. The lateral oxidation can be formed during local oxidation. Therefore length of the source-drain channel decreases, because source and drain regions can be moved under the gate. A large attention must be paid to this process.

Silicon on Sapphire (SOS) technology have recently attracted more and more interest in the development of next-generation high-performance VLSI circuits and systems. The absence of latch-up, the reduced parasitic capacitance, the transparency of the substrate, the isolation and multi-threshold devices are just a few of the advantages of this technology.

Silicon on sapphire is an integrated circuit manufacturing technology. It is a hetero-epitaxial process that consists of a thin layer of silicon grown on a sapphire (Al_2O_3) wafer and this epitaxial layer etching (Fig. 2).

Created silicon regions are isolated by wafer from bottom and from the side by air space. It is necessary to avoid lateral encroachment during region formation, because "active" length of region can be reduced, where transistors are formed.

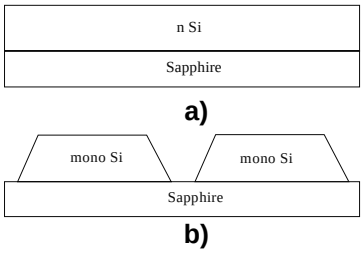

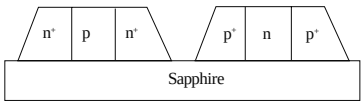

c)

Φιγυρε 2. ΣΟΣ τεχηνολογψ: α □ επιταξιαλ οφ σι λιχον; β □ σεπαρατεδ ρεγιονσ οφ σιλιχον χρεατ ιον; χ □ φορματιον οφ ΝΜΟΠ ανδ ΠΜΟΠ τρανσ ιστορσ

MOS transistor characterized by the output characteristic ($I_D(U_{DS})$). It is connected by common-source scheme. The inversion layer charge density varies in the channel between the source and the drain from 0 to L, channel voltage varies from 0 to U_{DS}:

$$\int_0^L I_D dy = -\mu C_{ox} B \int_0^{V_{SI}} (U_{GS} - U_S - U_C - U_T) dU_C, \quad (1)$$

$$I_D = -\mu C_{ox} \frac{B}{L}((U_{GS} - U_T)U_{DS} - \frac{U_{DS}^2}{2}),$$

$$when \ \ U_{DS} < U_{GS} - U_T, \quad (2)$$

where μ – the mobility, cm²/V; C_{ox} – capacitance per unit area, μF; B – gate width , nm; L – gate length , nm; U_{GS} – gate-source voltage, V; U_S – drain-source voltage, V; U_C – inversion channel voltage, V; U_T – threshold voltage, V. Output current direct proportional channel length (2). In this we got, that decreases channel length increases escarpment of transistor output characteristics, threshold voltage and drain current.

5. PROCESS SIMULATION

Etch process is simulated with ATHENA. ATHENA is a simulator that provides general capabilities for numerical, physically – based, two – dimensional simulation of semiconductor processing.

The ELITE module of ATHENA allows the use of sophisticated models for etch process. This process is modeled by defining a machine and invoking the machine to perform etch [8].

For all models except Monte Carlo Etching, ELITE uses a string algorithm to describe topographical changes that occur during etching process.

As micro/nanofabrication technology becomes more complex, modeling each step of the manufacturing process is increasingly important for predicting the performance of the technology.

Etching is a step that is universal in micro/nanofabrication. It may take place as the dissolution of a photoresist by an organic solvent, the etching of an oxide by an alkali, or the plasma etching of an electron resist. Whatever its physical details, the etching process can in many cases be modeled as a surface etching phenomenon. Etching simulation starts from an initial profile that moves through a medium in which the speed of etching propagation can be a function of position and other variables that determine the final profile.

Main task of etching process simulation is avoid lateral encroachment during region formation.

Wet Etching can provide a higher degree of selectivity than dry etching techniques. In isotropic etching (Fig. 3a) materials are removed uniformly from all directions and it is independent of the plane of orientation of the silicon (crystal lattice). Anisotropic etching presents presents the opposite behavior of isotropic etching. Anisotropic etchants remove materials based on the crystal plane and do not etch uniformly in all directions (Fig. 3b)

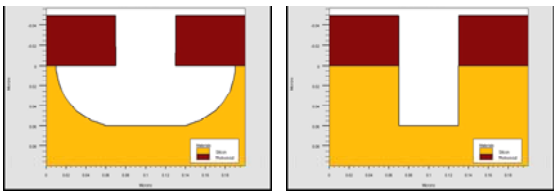

a) b)

Φιγυρε 3. Ωετ ετχηινγ τψπεσ: α □ ισοτροπιχ ετχ η; β □ ανισοτροπιχ ετχη

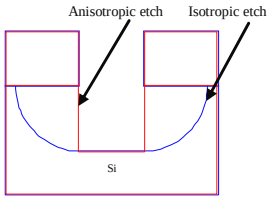

Φιγυρε 4. Χομπαρισον ωετ ετχηινγ τψπεσ: βλυε λινε □ ισοτροπιχ; ρεδ λινε □ ανισοτροπιχ

Anisotropic etching solves the problem of lateral control. The laterally masked geometry of

the planar surface can be etched and a vertical profile can be easily made. Although it solves the problem of lateral etching, the process is not problem-free. The process is slow even in the fast etching direction of the plane (100) and consumes more time.

Despite its simplicity in controlling the etching, wet etching is not flexible and reliable process. A dry etching process is an alternative choise (Fig. 5)

Dry Etching has several significant advantages compared with wet etching: it is much easier to start and stop than simple immersion wet etching; less undercutting; better process control. Ion milling (Fig. 5) has two significant advantages compared to high–pressure plasmas: directionality and applicability. With RIE can be achieved much higher selectivity compared with with ion milling.

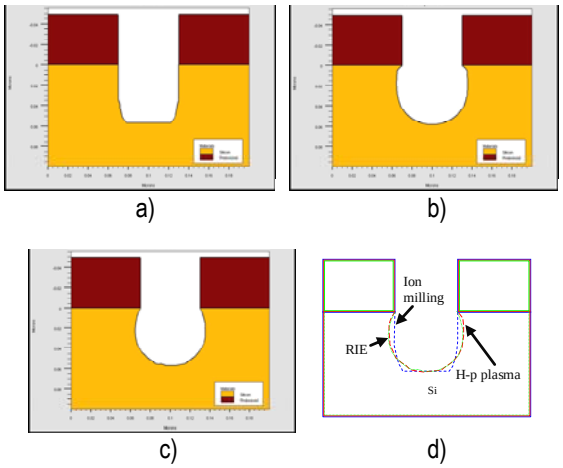

Φιγυρε 5. Δρψ ετχηινγ τψπεσ: α □ ιον μιλλινγ ετχη, β □ ηιγη–πρεσσυρε πλασμα ετχη, χ □ PIE ετχη; δ □ χομπαρισον δρψ ετχηινγ τψπεσ: βλυε λινε □ ιον μιλλινγ; ρεδ λινε □ πλασμα, γρεεν λινε □ PIE

Etching process is simulated in silicon depending on crystallographic planes orientation. Only (100), (110) and (111) crystallographic planes orientation are recognized in process simulator – ATHENA. Every etching process simulated 10 times and average time values is given in Table 1 and Fig. 6.

According to wet and dry etching process simulation results less lateral encroachment during region formation could be achieved using dry etching technology – ion milling. It has better directionality and time of etching process is less (~3s). The highest etching rate is reached in substance with crystallographic planes orientation (100). The lowest etching rate is reached in substance with crystallographic planes orientation (111), because there are 8 planes in substances with crystallographic planes orientation (111), which suspend etching process.

Ταβλε 1. Ετχηινγ προχεσσ ανδ τιμε δεπενδενχε ον χρψσταλλογραπηιχ πλανεσ οριεντατιον

	Crystallographic planes orientation			Etching type
	<100>	<110>	<111>	
Time, s	31,62	35,4	37,26	Anisotropic
	36,82	38,12	39,16	Isotropic
	2,81	2,97	3,56	Ion milling
	287,35	293,7	301,7	H-p plasma
	202,37	203,8	204,78	RIE

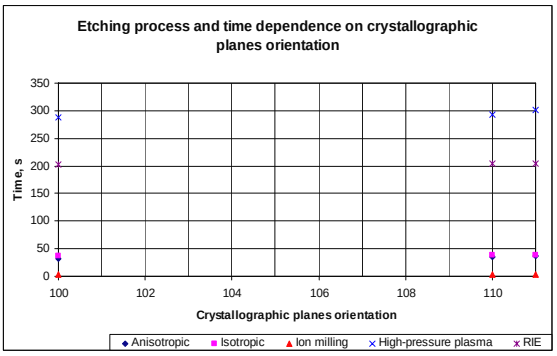

Φιγυρε 6. Ετχηινγ προχεσσ ανδ τιμε δεπενδενχε ον χρψσταλλογραπηιχ πλανεσ οριεντατιον

6. CONCLUSION

Unavoidable problems associated with wet etching process are: difficulties in etching at convex corners; difficult in preparing the mask with high precision; etch rate is very sensitive, it difficult to control both lateral and vertical geometries of the structure.

Using dry etching: it is possible to get less undercutting; better process control, directionality (Ion milling).

Less lateral encroachment could be achieved using dry etching technology – ion milling during region formation in MOS/CMOS technology.

The highest etching rate is reached in substance with crystallographic planes orientation (100). The lowest etching rate is reached in substance with crystallographic planes orientation (111).

References

[1] S. Dimitrijev. Understanding Semiconductor Devices. – ISBN 0-19-513186-X. – New York: Oxford University Press, 2000. – 574 P.

[2] N.P. Mahalik. Micromanufacturing and Nanotechnology. – ISBN 3-540-25377-7. – Germany: Springer-Verlag Berlin Heidelberg, 2006. – P. 107–125

[3] Stephen A. Campbell. The Sciences and Engineering of Microelectronic Fabrication. – ISBN 0-19-513605-5. – New York: Oxford University Press, 2001. – P. 258–286.

[4] Britannica encyclopedia. Website of Britannica. Internet.http://www.britannica.com/ebc/article-9368038 [2008 03 02].

[5] D. Andriukaitis, R. Anilionis, T. Kersys. LOCOS CMOS Process Simulation // Proceedings of 28th International Conference on INFORMATION TECHNOLOGY INTERFACES ITI 2006, June 19-22, 2006, Cavtat/Dubrovnik, Croatia. ISSN 1330-1012. - P. 489–494.

[6] B. Bhushan. Springer Handbook of Nanotechnology. – ISBN 3-540-01218-4. – Spinger-Verlag, Berlin, Germany, 2004. – 1258 P.

[7] Wikipedia encyclopedia. Website of WIKIPEDIA International. Internet. http://en.wikipedia.org/wiki/Silicon_on_sapphire [2008 03 02].

[8] Mathematical simulation program ATHENA. Official Website of SILVACO International. Internet. http://www.silvaco.com [2008 03 05].

THE COMPLEX AC RESPONSE MEASUREMENT WITH USB CONNECTIVITY TO PC

L. Svilainis, V. Dumbrava

Signal processing department, Kaunas University of Technology
Studentu str. 50, LT-51368 Kaunas, Lithuania
T, +370 37 300532; F, +370 37 753998;E, linas.svilainis@ktu.lt / vytautas.dumbrava@ktu.lt

Abstract

Design of the portable acquisition module for AC parameters measurement is presented. Module has USB connectivity and is operated by host PC. The application of sine wave correlation technique for complex amplitude measurement together with direct digital synthesis for excitation signal and same reference clock allow for significant accuracy improvement and processing simplification. The availability of two simultaneous ADC channels enables complex impedance and gain and phase measurements. Application examples for insertion gain and phase, power stage output amplitude and complex impedance measurement are presented.

1. INTRODUCTION

The AC response is one of the essential parameters of an electronic system [1]. The frequency response of the electrical properties of material is used in medicine [2], biosensors [3] development. Electrical impedance spectroscopy is used even in food industry [4] and the ionic conductivity studies [5].

Numerous publications [1-7] indicate the need for such systems. The performance of commercially available equipment is sufficient but the price is high and such devices are bench instruments which are dedicated for particular tasks. Therefore researchers have turned to customized equipment design. The analog-to-digit (ADC) converters [1] are applied for amplitude and phase measurement. Sine wave fitting technique is used for amplitude, phase and frequency extraction [6]. This technique have inherent error source since the test and ADC sampling frequency ratio is not exactly known. Therefore fitting procedure requires the frequency estimation. Uncertainty in frequency estimation is causing the magnitude and phase error.

In this paper we present the design of the portable AC parameter measurement system which is free from the mentioned shortcoming. A direct-digital-synthesis (DDS) is used for excitation signal generation. Same reference frequentcy source is used for DDS and ADC clocking. Such combination eliminates the excitation and sampling frequencies ratio estimation error. Module has the USB connectivity and is dedicated for ultrasonic equipment amplitude and phase AC response measurement.

2. AC PHASOR ESTIMATION

The frequency response of device under test (DUT) at certain frequency can be determined by probing the system input with a single frequency sine signal while measuring the input/output amplitude ratio and phase difference.

The application of the sine-fitting techniques [6] can largely reduce the influence of noise in the final results. If harmonic signal is used for excitation, the resulting waveform can to be fit as:

$$u(t) = U_c \cos(2\pi ft) + U_s \sin(2\pi ft) + U_{DC}\,, \quad (1)$$

where U_c and U_s are the orthogonal harmonic signal components of the sine wave, U_{DC} is the DC component and f is the excitation signal frequency (Figure 1).

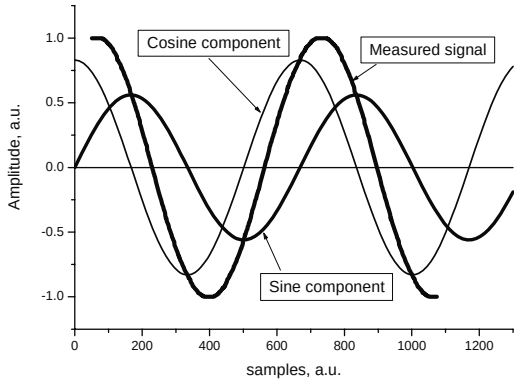

Figure 1. Phasor approximation

Fitting this function to the sampled signal $y_1 \ldots y_M$, acquired at a frequency f_s at time instances $t_1 \ldots t_M$, is accomplished by minimising:

$$\varepsilon_{RMS} = \sqrt{\frac{1}{M}\sum_{m=1}^{M}\left[y_m - u(t_m)\right]^2} . \quad (2)$$

The procedure is iterative, e.g. consuming a lot of computational time and has the inherent error related to frequency estimation. Sine wave correlation (SWC) technique is proposed for signal amplitude and phase measurement [7]. It is suggested to use common reference frequency source for excitation generator and sampling. Then frequency instability errors can be disregarded. In such case non-iterative fitting is used:

$$U_c = \frac{\sum_{m=1}^{M}\left[\cos(2\pi f t_m)\cdot y_m\right]}{\sum_{m=1}^{M}\left[\cos(2\pi f t_m)\right]^2}, \quad (3)$$

$$U_s = \frac{\sum_{m=1}^{M}\left[\sin(2\pi f t_m)\cdot y_m\right]}{\sum_{m=1}^{M}\left[\sin(2\pi f t_m)\right]^2}, \quad (4)$$

$$U_{DC} = \frac{\sum_{m=1}^{M} y_m}{M} . \quad (5)$$

Then the magnitude and phase:

$$U = \sqrt{U_c^2 + U_s^2}\ , \varphi = \arctan\left(\frac{U_s}{U_c}\right). \quad (6)$$

The SWC technique has been implemented for measured signal amplitude and phase estimation in data acquisition module.

3. EXCITATION GENERATOR

In order to have fixed ratio of excitation signal and ADC sampling frequency DDS technique was proposed.

The DDS structure is presented in Figure 2. The DDS output frequency depends upon three parameters: tuning word value ($0<D<2^{N-1}$), clock frequency (F_s) and accumulator capacity 2^N. Output frequency can be expressed as $f=d\varphi/dt$. Time step dt is dependant upon clock frequency and can be expressed as $dt=1/F_s$.

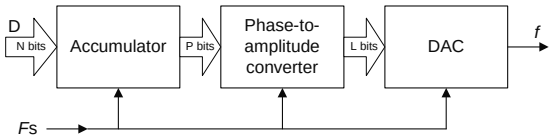

Figure 2. DDS generator structure

The phase increment $d\varphi$ is the angle which is accumulated at every clock dt. The value $d\varphi$ is the ratio of the tuning word D and accumulator capacity. Then the output frequency:

$$f = \frac{F_s \cdot D}{2^N} . \quad (7)$$

Only P accumulator bits are used for phase-to-amplitude conversion. The amount of P bits defines the jittering of output signal. Furthermore, only L bits of phase-to-amplitude converter output are used for DAC. The DDS generator output signal frequency, amplitude and phase can be controlled digitally. It was decided to use DDS as it is getting more popular for its simplicity, flexibility and good performance results. Essential, that using DDS the ratio of DDS reference frequency and the harmonic signal output signal is fixed. This fixed ratio is demanded for SWC technique implementation.

4. ACCURACY ESTIMATION

The SWC processing of the signal can be treated as narrowband signal filtering and leads to improved processing gain thanks to significant signal oversampling [8]:

$$PG = 10\log_{10}\left(\frac{f_s}{2 \cdot B}\right), \qquad (8)$$

where f_s is a sampling frequency and B is digital processing filter bandwidth. Digitization noise RMS:

$$U_{ADCnRMS} = \frac{U_{FS}}{2^K \sqrt{12}}, \qquad (9)$$

where K is ADC bits number, U_{FS} is the ADC full-scale range.

Treating the reference signal as gated sine wave corresponds to a *sinc* filter in frequency domain. The filter bandwidth expressed as function of length M of the sampled array obtained using frequency f_s

$$B = \frac{f_s}{M}. \qquad (10)$$

Then resulting digitization noise RMS value

$$U_{nRMS} = \frac{U_{\mathrm{Re}\,f}}{2^K \sqrt{12}} \cdot \sqrt{\frac{2B}{F_s}} = \frac{U_{\mathrm{Re}\,f}}{2^K \sqrt{12}} \cdot \sqrt{\frac{2}{M}}. \qquad (11)$$

The theoretical analysis, numerical simulation and experimental results have been presented in [7].

5. MEASUREMENT SYSTEM

The system (Figure 3) contains both the excitation and the receiving units.

The excitation channel and the receiving part are connected DUT according to the needed measurement scheme. The driving channel is built using the DDS generator AD9851 from Analog Devices. The AD9851 contains a reference clock multiplier which eliminates the need for a high speed reference oscillator. The DDS's output waveform phase is time-continuous in case of the frequency change. The output signal after filtering and amplification is attenuated by smooth attenuator and two fixed 20dB attenuation blocks. The receiving part consists of the high input impedance preamplifier (optional) and the programmable gain amplifier (PGA), controlled via I2C interface which in turn is tied to a host PC via USB core. The PGA is AD8367 from Analog Devices with 45 dB of variable gain with a linear-in-dB gain. Gain control voltage is derived from AD5321. The AD5321 is a single 12-bit buffered voltage-output DAC. It uses a I2C interface that is derived from the USB controller core. The conditioned signal is supplied to the acquisition unit. The high speed dual channel data acquisition consists of two high speed 10-bit ADC AD9214 operating at 100MS/s conversion rate. The DAC output data is streamed to the high speed SRAM IS61LV25616 from Integrated Silicon Solution, Inc. organized as 256k words by 16 bits. The latching, synchronization and control state machine is organized by 3 Complex Programmable Logic Device (CPLD) chips M4A3-128/64 from Lattice. The CPLD also performs the PC104 bridge functions. PC104 bus is used for main control. It is emulated by the low-power USB2.0 microcontroller EZ-USB FX2LP IC CY7C68013A from Cypress Semiconductor Corporation's. The GPIF bridge, mimicking the PC104 bus is used for connection to USB.

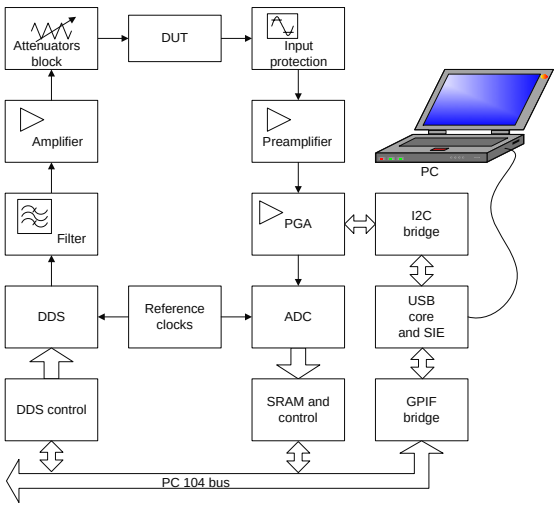

Figure 3. Measurement system

Acquisition module PC-104 stack photo is presented in Figure 4. The top PCB is the exci-

tation DDS with optional RMS detector channel. Middle PCB is the dual channel ADC card. The bottom card is the USB interface and PC104 bridge.

Figure 4. PC-104 stack

Such configuration ensures that up to 256k samples of analog signal can be captured on two acquisition channels at highest 100Ms/s rate.

6. APPLICATION

Figure 5 presents the conventional setup of the module for the DUT AC response measurement. Gain and phase can be calculated since complex signal amplitudes for circuit input and output are available thanks to dual ADC channel acquisition capability.

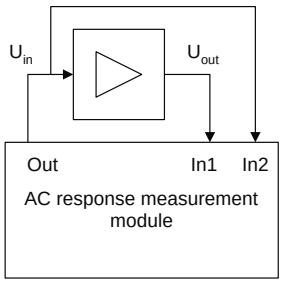

Figure 5. Amplifier AC response

The obtained insertion loss can be stored in a computer memory for compensation of results obtained using the investigated amplifier. The diagram presented in Fig 6 demonstrates the result of ultrasonic preamplifier AC response measurement. Obtained results are presented as gain in dB and phase in degrees.

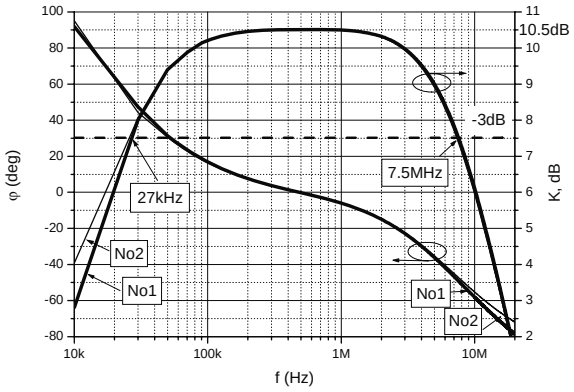

Figure 6. Two channels AC response

Results for high voltage amplifier several configurations measurement are presented in Figure 7.

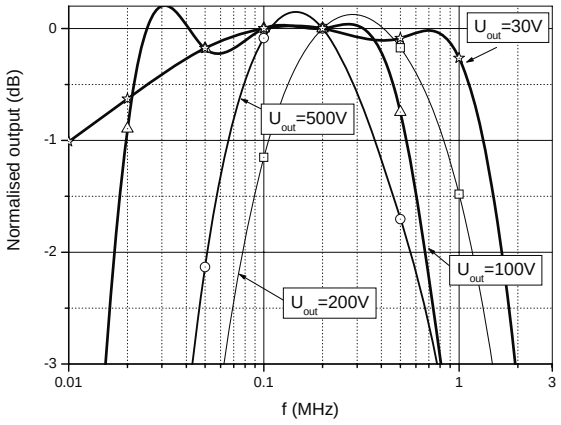

Figure 7. High voltage AC response

The module can be configured for electrical impedance measurement [19]. Necessary setup, using I-V method is presented in Figure 8. The since single-ended implementation is offering the lowest complexity of implementation.

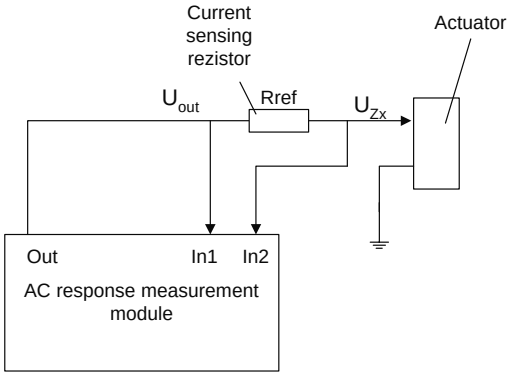

Figure 8. Impedance measurement

Current is calculated using the voltage measurement across an accurately known resistor, R_{ref}.

$$Z_x = \frac{U_{Zx}}{I} = \frac{U_{Zx}}{U_{out} - U_{Zx}} R_{ref} . \quad (12)$$

The complex impedance can be presented as real and imaginary parts or as magnitude and phase. As an example of the dynamic range available, ultrasonic actuator impedance was examined. Actuator impedance investigation results example is presented in Figure 9.

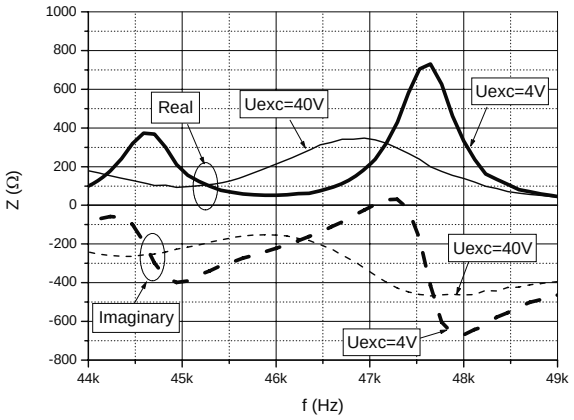

Figure 9. Impedance vs. excitation

The real and imaginary of parts of electrical impedance variation when actuator excitation voltage is changing can be observed. More experimental results of ultrasonic transducers measurement can be found in [9].

7. CONCLUSIONS

The presented module for AC parameters investigation is universal. It can be applied for various AC parameters investigation. It has USB connectivity and is operated by host PC. The application of sine wave correlation technique for complex amplitude measurement together with direct digital synthesis for excitation signal and same reference clock allow for significant accuracy improvement and processing simplification. The availability of two simultaneous ADC channels enables complex impedance and gain and phase measurements.

References

[1] J. Castello, et.al., "A PC-based low cost impedance and gain-phase analyzer," Measurement, vol.41, 2008, pp.631-636.

[2] B.A. Shanholtzer and S.M. Patterson. Use of bioelectrical impedancenext term in hydration status assessment: reliability of a new tool in psychophysiology research. International Journal of Psychophysiology, vol.49, 2003, pp.217-226.

[3] M.F. Diouani et.al. Miniaturized biosensor for avian influenza virus detection. Materials Science and Engineering C. vol.28, 2008, pp.580–583.

[4] J.Damez, et.al., "Beef meat electrical impedance next term spectroscopy and anisotropy sensing for non-invasive early assessment of meat ageing," Journal of Food Engineering, vol. 85, 2008, pp.116-122.

[5] D.P. Almonda, B. Vainas, N.F. Uvarov, "A new analysis of the bulk ac electrical response of ionic conductors," Solid State Ionics, vol. 111, 1998, pp.253–261.

[6] P.M. Ramos, A.C.Serra, "A new sine-fitting algorithm for accurate amplitude and phase measurements in two channel acquisition systems," Measurement, vol.41, 2008, pp.135–143.

[7] L. Svilainis, V. Dumbrava, "Amplitude and phase measurement in acquisition systems," Matavimai, 2006, vol.38, pp.21-25.

[8] W.Kester, *Analog-digital conversion*, Analog devices, 2004.

[9] L. Svilainis, V. Dumbrava, "Measurement of complex impedance of ultrasonic transducers," Ultragarsas, vol.62, 2007, pp.26-29.

ACQUISITION AND PROCESSING OF PHOTOPLETHYSMOGRAPHIC SIGNAL FOR REGISTRATION OF HEART RATE OF MOVING PERSON

Darius Jegelevicius[1,2], Vaidotas Marozas[1,2], Arunas Lukoševičius[1,2], Linas Svilainis[2]

[1]Biomedical engineering institute, Kaunas University of Technology, Kaunas, Lithuania
[2]Signal processing department, Kaunas University of Technology
Studentu str. 65-111, LT-51369, Kaunas, Lithuania
T. +370 37 407119; F. +370 37 407119; E. darius.jegelevicius@ktu.lt

Abstract

Investigation of photoplethysmo-graphic sensors application for subjects' heart rate monitoring for in-situ conditions is presented. Inertial acceleration sensor mounted together with PPG sensor was used for estimation of motion intensity. The sensor signal was acquired by placing it on the subject's: forehead, breastbone and wrist in the rest and active moving conditions. ECG sensor was used as a reference source. The most accurate results were obtained from the forehead. Analysis showed that time - frequency representation of PPG signal is the superposition of two time - frequency representations: noise free heart rate signal and motion intensity signal. This observation suggests possibility to remove motion induced noise from the PPG signal.

1. INTRODUCTION

Photoplethysmographic (PPG) sensors [1] are widely used in monitoring of blood oxygenation and heart rate (HR) of the subjects in clinical bed rest conditions [2, 3]. PPG sensors are attractive due to compactness, noninvasiveness and functionality. Application of PPG sensors would be very attractive in telemedicine applications [4].

When patient motion intensity is relatively low, there is a good correlation between ECG and PPG signals in heart rate measurement (Figure 1). Then PPG sensor has an advantage against the multielectrode based ECG sensor. However subject movement introduces a large noise component into PPG signal.

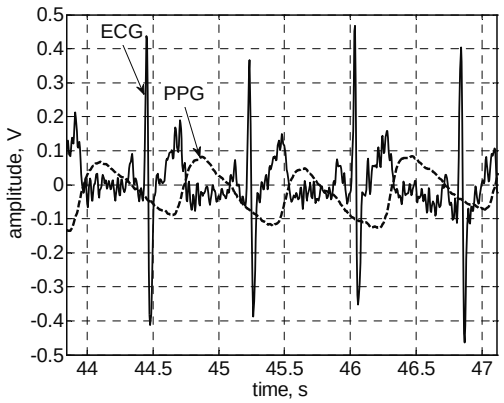

Figure 1. EKG and PPG signals while subject in rest

The subject movement induces displacements of the sensor-to-tissue and tissue-to-bone conditions which in turn cause PPG signal distortion (Figures 2, 3).

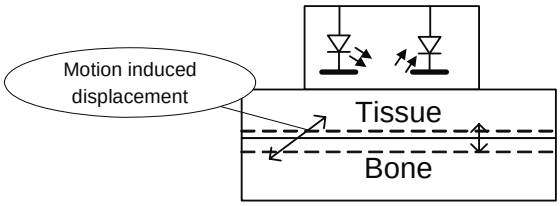

Figure 2. PPG signal registration

Subject motion influence on PPG signal is shown in Figure 3.

Figure 3 shows that subject motion causes significant PPG signal distortion which subsequently leads to heart rate estimation errors.

Thus the ability to extract accurate physiological data from PPG sensor during subject

activity remains a significant challenge [5]. Several attempts have been taken to search for the best PPG sensor placement on the body: it has been suggested to use a finger-wearable sensor in [6]; yet another study [7] investigated possibility to place the sensor on a wrist. Our research was undertaken in order to systematically investigate the aspects of PPG based estimation of heart rate in three different sensor positions on human body under different motion intensity.

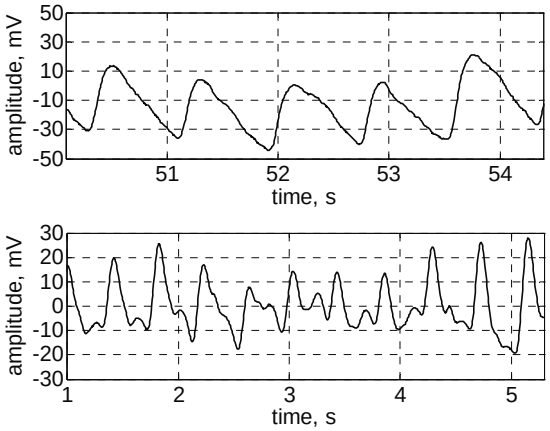

Figure 3. Subject motion influence on PPG signal. Top: PPG signal in rest; bottom: PPG signal in motion

2. ACQUISITION SETUP

An experimental infrared light sensor based on reflection was used for PPG signal registration (Figure 5).

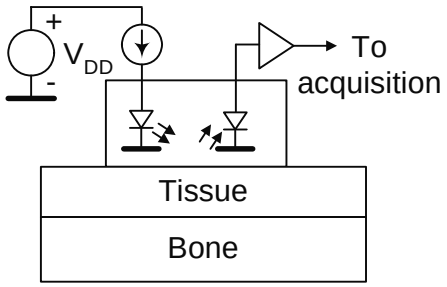

Figure 5. PPG sensor

Two TSMS3700 infrared LEDs with the excitation current 30 mA have been used to generate the luminous flux. The BPW34 photodiode was used for the reception. Signal was conditioned using operational amplifier AD8047. Motion intensity was estimated using two axes accelerometer ADXL202 with 1kHz cut-off frequency filter mounted together with PPG sensor (Figure 6).

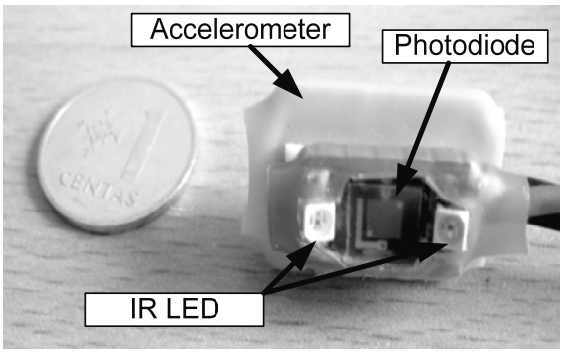

Figure 6. PPG and acceleration sensors fusion

The PPG signal was acquired (Figure 7) by placing the sensor on the subject's: a) forehead, b) breastbone, c) wrist in the rest and active moving (walking, running, jumping and elliptical cross trainer) conditions. As the reference source of heart rate the ECG chest strap (Polar Oy) was used.

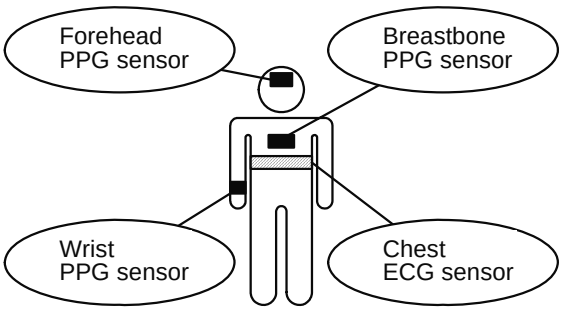

Figure 7. Sensor placement

PPG, acceleration and ECG signals were digitized (Figure 8) by using the biosignals' acquisition system MP35 from Biopack Inc. It has four isolated, human-safe, universal biopotential or transducer input amplifiers with 24bit AD converters. The sampling rate was chosen to be 1kHz. High sampling rate prevents from missing short pulses coming from heart rate monitoring strap. Raw signals were passed via USB interface to personal computer and stored for offline processing. Signal processing algorithms were developed in MATLAB.

For heart rate calculations from PPG signal, low frequency filtering, signal derivation and searching for peaks was used. Calculated HR

then was filtered with moving average filter with a cut of frequency of 0.11 Hz.

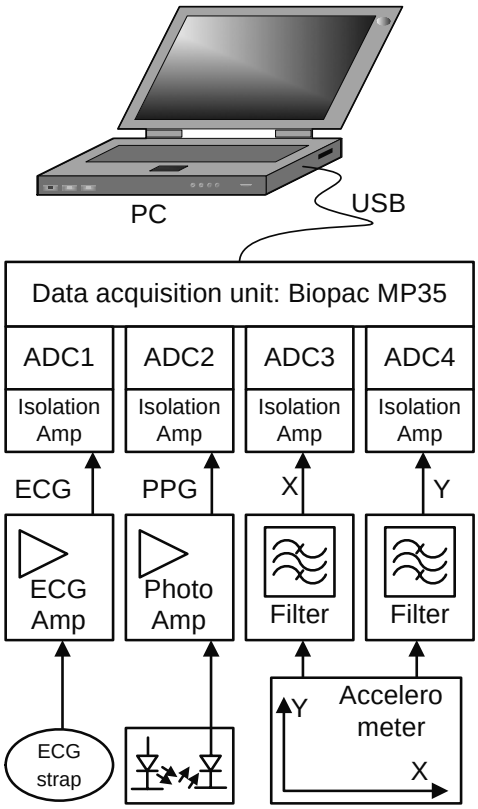

Figure 8. Acquisition system

Three performance indexes were used for the evaluation of heart rate estimated from PPG signals under different registration conditions:

a) correlation coefficient:

$$\rho = \frac{\sum_{n=1}^{N}\left[r_{\overline{PPG}}[n]\cdot r_{\overline{ECG}}[n]\right]}{\sqrt{\sum_{n=1}^{N}\left(r_{\overline{PPG}}[n]\right)^2\cdot\sum_{n=1}^{N}\left(r_{\overline{ECG}}[n]\right)^2}} \quad (2),$$

where $r_{\overline{PPG}}[n] = r_{PPG}[n] - \bar{r}_{PPG}$ and $r_{\overline{ECG}}[n] = r_{ECG}[n] - \bar{r}_{ECG}$;

b) mean of the difference $\Delta r[n] = r_{PPG}[n] - r_{ECG}[n]$:

$$\overline{\Delta r} = \frac{1}{N}\cdot\sum_{n=1}^{N}\Delta r \quad (3);$$

c) standard deviation of the Δr:

$$\sigma = \sqrt{\frac{1}{N}\cdot\sum_{n=1}^{N}\left[\Delta r[n] - \overline{\Delta r}\right]^2} \quad (4).$$

3. RESULTS

Figure 9 shows an example of the set of raw signals registered during cyclical motion.

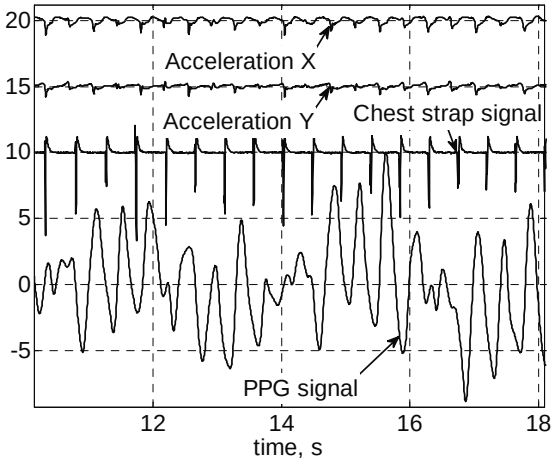

Figure 9. Registered signals

It can be observed that even at a moderate motion intensity PPG signal significantly differs from normal signal shown in Figure 1 and the heart rate is hardly discernable.

Figure 10 is presenting the correlation coefficient between the heart rate obtained from ECG and PPG sensors acquired in different physiological activity conditions. The placement of the sensor (positions are indicated in Figure 7) was varied and is indicated by three different curves.

It can be seen that forehead placement is exhibiting the best results even for complicated conditions. It can be explained that human anatomy is designed in such way that vision system that is placed in the head receives the least motion. The wrist sensor, though is most technologically desirable can be characterized as the worst performer.

The HR estimation accuracy based on ECG as a reference is presented as box-and-whisker plot in Figures 11-13. The box encloses 50% of the data (the interquartile range, IQR), a line in the box represents the median. Whiskers are 1.5 IQR. Dots represent the values out of this range.

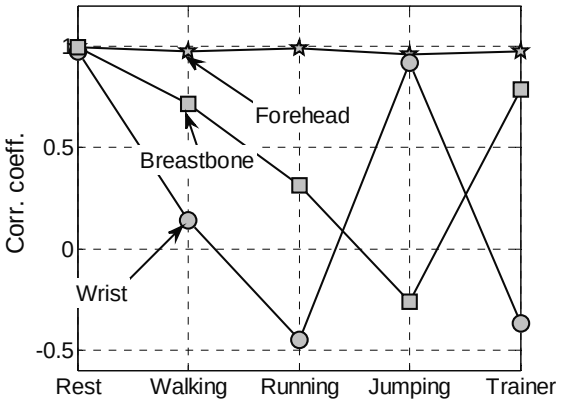

Figure 10. Correlation coefficients between ECG and PPG based heart rate estimation for different sensor positions and motion intensity

Figure 11. HR on forehead estimation

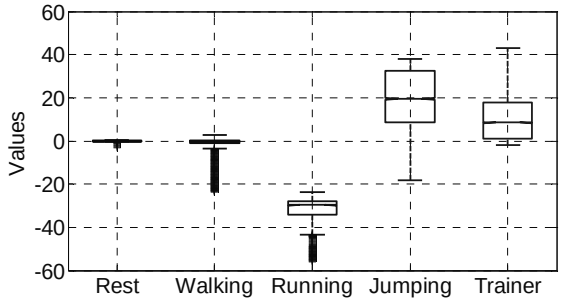

Figure 12. HR estimate on breastbone

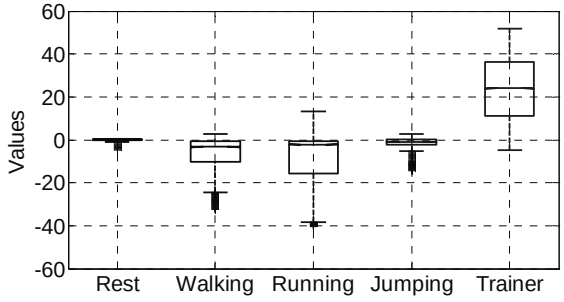

Figure 13. HR estimate on the wrist

The range of y axes in Figure 11 to Figure 13 was chosen the same in order to allow the results comparison.

Whisked diagrams again confirm that PPG sensor placement on forehead is the best position among all investigated.

The Table 1 presents numerical results of sensor performance for forehead position. Even strong motion, e.g. jumping, does not increase the heart rate estimation error beyond limits as it was the case in other body places.

Table 1. Heart rate estimation performance using PPG signal when sensor was placed on the forehead

Movement condition	Corr. coeff.	Mean	Std
Rest	0.9964	-0.0069	0.1621
Walking	0.9723	-0.0904	0.8928
Running	0.9899	-0.2686	1.3289
Jumping	0.9562	1.5969	4.5568
Elliptical cross trainer	0.9735	-4.7784	3.4786

Investigation has been done in order to evaluate the ability to separate the errors sources. Signals from the wrist sensor were taken for the running subject case. Since it was assumed that there is no significant influence of motion axis on the clutter as explained in Figure 2, the accelerometer x and y axes were combined taking their geometrical mean vector for calculation. Short Fourier transform was used on the acquired signals in order to evaluate the spectral content variation in time. Frequency scale was recalculated into cycles/min in order to relate it to HR measurement units (beat/min).

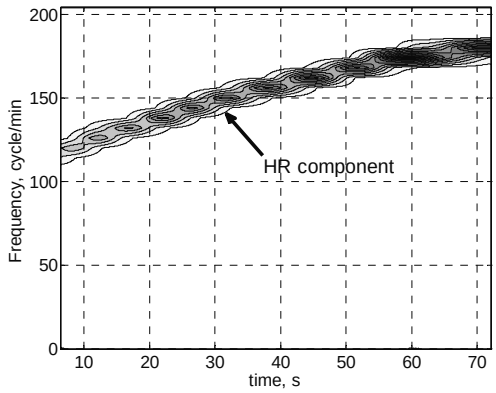

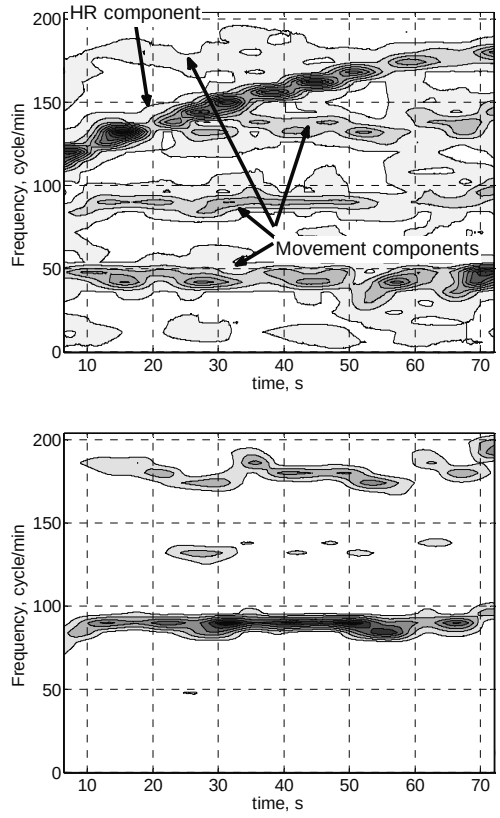

Figure 14. Temporal behavior of signals spectrum for running subject. Top: ECG, center: PPG, bottom: acc

It can be seen that there is a great correlation in spectral content between the acceleration and the PPG sensor signal. Though it can be concluded that heart rate is changing smoothly, there is an intersection of the HR and motion induced frequencies. This is clearly seen on 30'th and 60'th second of the experiment.

4. CONCLUSIONS

Analysis showed that spectrum of motion activity signal overlaps with the PPG signal. Heart rate computed from moving subject's PPG signal has significant high frequency component if we compare it with heart rate obtained using ECG chest strap. The most accurate results were obtained from the forehead PPG signal: lowest systematic error and the standard deviation of the random error were obtained. Though results for forehead placement are encouraging, it is worth trying to apply tracking phase filters or adaptive signal processing methods for wrist placement implementation of the sensor. There good candidates would be methods used in [8, 9].

ACKNOWLEDGMENTS

The study was partially supported by Lithuanian State Science and Studies Foundation, reg. Nr. B-07018, project "Development of Methods and Equipment for Human Active Motion Monitoring".

References

[1] M.J. Hayes, et al., "Quantitative Investigation of Artifact in Photo-plethysmography and Pulse-Oximetry for Respiratory Exercise Testing", *Proc. of the CNVD 97 Frontiers in Computer-Aided Visualization of Vascular Functions*, 1998, pp. 117-24.

[2] A. Sola, L. Chow, M. Rogido, "Pulse Oximetry in Neonatal Care. A Comprehensive State of the Art Review", *Anales of Pediatria*, Vol.62(3), 2005, pp. 266-80.

[3] H.M. Sami, B.S. Kleinman and V.A. Lonchyna, "Central venous pulsations associated with a falsely low oxygen saturation measured by pulse oximetry", *J Clin Monit*, Vol.7, 1991, pp. 309–312.

[4] A. Paunksnis, V. Barzdziukas, D. Jegelevicius, et al. "The use of information technologies for diagnosis in ophthalmology", *Journal of telemedicine and telecare*, Vol. 12, Suppl. 1, 2006, pp: 37-40.

[5] Y. Yamaya, H.J. Bogaard, P.D. Wagner, K. Niizeki, S.R. Hopkins, "Validity of pulse oximetry during maximal exercise in normoxia, hypoxia, and hyperoxia", *Journal of Applied Physiology*, Vol. 92, 2002, pp.162–168.

[6] H. Asada, P. Shaltis, A. Reisner, S. Rhee, R. Hutchinson, "Mobile Monitoring with Wearable Photoplethysmographic Biosensors", *IEEE Engineering in Medicine and Biology Magazine*, Vol. 22 (3), 2003, pp.28-40.

[7] Ph. Renevey, R. Vetter, P. Celka, J. Krauss, "Activity Classification Using HMM For Improvement Of Wrist Located Pulse Detection", *BioSignal 2002*, Brno, Czech Republic, June 26 - 28, 2002, pp. 192-196.

[8] R. Kazys, L. Svilainis, "Analysis of adaptive imaging algorithms for ultrasonic non-destructive testing", *Ultrasonics*, Vol 33(1), 1995, pp. 19-30.

[9] V. Marozas, A. Janusauskas, A. Lukosevicius, et al. "Multiscale detection of transient evoked otoacoustic emissions", *IEEE transactions on biomedical engineering*, Vol: 53(8), 2006, pp. 1586-1593.

MEASUREMENT OF IR TEMPERATURE DEVIATION IN BIO-MEDICINE

Andrew Andreev
Anna Andonova
Ivo Iliev

Centre of Biomedical Engineering "Prof. Ivan Daskalov",
Bulgarian Academy of Sciences Acad.G.Bonchev str. Bl.105, 1113, Sofia, Bulgaria
+359 88 7526408;
andrew.andreev@binnetix.com,
ava@ecad.tu-sofia.bg,
izi@tu-sofia.bg

Abstract

The modern thermographs converts the information gathered during the scanning of the infrared spectrum into true colour graphical images. Temperature levels are represented by different colour palette in accordance to the practical needs.

The current research and development is software engine for colour graphical analyzes of the IR images, optimized for parallel execution in grid environment. The analyzes of IR images covers: the automatic colour palette recognition including determination of temperature deviations, generation of thermo-histogram for measuring the temperature levels, comparison of temperature deviation between two or more images within a range without geometrical parameters dependency and generation of 3D temperature deviation model.

This approach allows effectively and continuously to process different bio-medical objects including the workload monitoring of specialized micro electrical schemes in medical devices.

1. INTRODUCTION

Infrared (IR) thermography is a technique for remotely measuring the surface temperature. IR thermography exploits the correlation between the surface temperature and the infrared energy emitted by the surface. This relationship is described by Stefan-Boltzmann's Law as follows:

(1)

$$R(T) = \sigma . T^4$$

where *T* is the temperature of the surface and $\sigma = 5.67 \times 10^{-8}\ W/(m^2.K)$. The IR light is described in physics by Planck's law as a spectral radiance of electromagnetic radiation of black body at temperature *T*. As a function of wavelength λ = (speed of light *c* vs. Frequency *v*) the Planck's law representation is:

(2)

$$I(\lambda, T) = \frac{2hc^2}{\lambda^5} \frac{1}{e^{\frac{hc}{\lambda kT}} - 1}$$

where *h* is Plank's constant, *k* is Boltzmann's constant. For the purposes of IR measurements the light must be described in terms of the *spectral energy density* and have to be digitized in wavelength units . After appropriate conversion the spectral energy density $u(\lambda,$ can be expressed as a function of wavelength, as follows:

(3)

$$u(\lambda, T).d\lambda = \frac{8\pi hc}{\lambda^5} \frac{1}{e^{\frac{hc}{\lambda kT}} - 1} d\lambda$$

In practice the IR measurement precision is acceptable when the radiation from the surface can be fully detected by the camera sensors. However, with the increasing of the distance between the surface and the sensor, the atmosphere has strong detrimental and perceptible impact on the accuracy. Taking in consideration additional factors like high humidity, rain, fog, the absorption effects due to water vapour and

CO_2, the thermographs could report temperatures with significant error deviation.

In addition, the result of modern thermograph cameras is saved and compressed in popular graphical image formats like JPEG. However, in such file format we are observing loss of graphical information and increased noise of the images.

The current implementation allows the graphical information from thermographs to be analyzed from scratch using only external parameters, providing good precision and high performance image processing.

2. BACKGROUND

[1] The calculation of object temperature from the calibrated camera output depends on the received radiation power W from a black body source of temperature T_{source}. On short distance the thermograph generates output signal U_{source} that is proportional to the camera power input:

(4)

$$U_{source} = C.W(T_{source})$$

where C is a constant value. If the source is gray body with emittance ε, than the received radiation would consequently be εW_{source}. The total received power radiation W_{total} depends on three terms:

- Object emission
- Reflected emission
- Atmosphere emission

(5)

$$W_{total} = \varepsilon\tau W_{obj} + (1-\varepsilon)\tau W_{refl} + (1-\tau)W_{atm}$$

where:

- $\varepsilon\tau W_{obj}$ is the emission from the object, ε is the object emittance; τ is the transmittance of the atmosphere. The object temperature is T_{obj}.
- $(1-\varepsilon)\tau W_{r}$ is the reflected emission from ambient sources, (1-ε) represents the reflectance of the object. The ambient sources have the temperature T_{refl}.
- $(1-\tau)W_{a}$ is the emission of the atmosphere. (1-τ) represents the emittance of the atmosphere.

In accordance with the Law of heat transmittance, the radiation power and temperature dependency can be represented by the fallowing formula:

(6)

$$W = \frac{S\gamma}{D}.T$$

where S is the heated surface, D is the transmitted distance from the object, γ is the specific temperature coefficient of transmittance, T is the temperature deviation. It can be considered that in the moment of thermal measurement for a short period of time the environment parameters remain unchanged. In that condition the fraction has a constant behaviour. It is obvious that the relationship between W and T is direct proportional – increasing T the value of W is increased also.

(7)

$$W = C_{source}.T_{source}$$

In accordance with above conditions and after appropriate substitutions in formula (4) and (5) we could represent the object temperature in terms of thermograph output signal as follows:

(7)

$$T_{obj} = \frac{1}{\varepsilon\tau}.T_{total} - \frac{(1-\varepsilon)}{\varepsilon}.T_{refl} - \frac{(1-\tau)}{\varepsilon\tau}.T_{atm}$$

The coefficients of object emittance ε and atmosphere transmittance τ may vary in diapason (0, 1].

The influence of the reflected emission is removed when ε = 1 (100% absorption of pure black body).

The influence of the atmosphere emission is removed when τ = 1 (vacuum).

The perfect conditions when measuring black body in vacuum the object temperature can be represented by:

(8)

$$T_{obj} = T_{total}$$

3. IMPLEMENTATION

The IR images temperature measurement is a complex procedure that solves the following five general tasks:

- Colour palette identification
- Colour transition approximation
- Colour pollution detection
- Temperature Range Calculation
- Statistical Aggregation

The above tasks are producing a result which could be summarised as follows:

- HSL (hue, saturation and luminance) image levels for each pixel
- Occurrence for each unique colour in the IR image
- Relative temperature levels

By combining the above information the current software engine generates:

A. Thermal histogram of the whole IR image.
B. Automatic generation of raw statistical data.
C. Comparison of temperature intensity between two or more temperature sub ranges.
D. Comparison of thermal histograms between two or more IR images

3.1. Colour Palette Identification

The colour palette identification is required in order to classify the full set of colour transitions that are necessary for the IR image analyses and temperature calculations. Normally the identification task looks simple and should be solved by applying one or more predefined standard palettes by choosing the most applicable one.

There are many colour systems that are measuring the distinction between the so called warm and cool colours. Such systems are: CIE 1931 Chromaticity Space, Geothe's Colour Wheel, Munsell's Colour System etc. Most certainly, the clearest and fully related to the energy density representation of Plank's law $u(\lambda,$ is Wien's Displacement Colour Temperature System [2]:

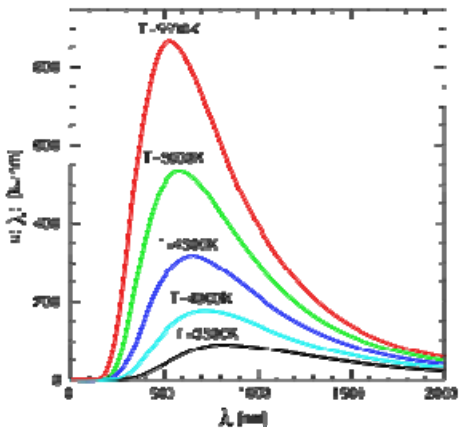

Figure 1. Black Body Spectrum

However in the practice, the thermographs are using custom defined colour palettes in order to generate IR images. For example in the Medicine it is accepted the coolest areas to be marked in black and most warm areas in white. In the heavy industry this selection is the opposite. However, even the intermediate colour transitions could be different.

Despite of the existence of several colour systems, it is obvious that direct comparison will take long time to process the entire image and would not cover cases when none of the standard palettes is applicable.

In order to avoid this weakness, the current implementation completely inverts the approach – what if the most applicable palette is hidden inside the IR image and can be generated directly from the source?

Such reverse-engineering is possible and it is a matter of appropriate colour selection and colour transition approximations. It is described in details in section 0.

3.2. Colour Transitions Engine

Because of the purposes of bio-medicine the current implementation accepts the Black colour to represent the coolest areas and the White colour to represent the warmest areas. In terms of thermographs this also means that any image information below the minimum temperature will be marked also in black. Respectively, anything above the maximum temperature will be marked in white.

The general concept of thermographs, in accordance with the Theory of Three Primary Colours, is to represent the temperature by colorizing the image in the visible spectrum [2].

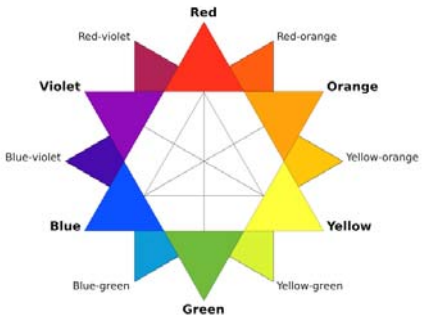

Figure 2. RGB Colour Star

The following colour chain can be identified: Black, Blue, Green, Yellow, Orange, Red, Violet and White. Therefore the possible colour transitions are 6. The algorithm preliminary accepts that any of those transitions are possible. It follows the rule of sequential natural colour transitions described in *Figure 2*.

The IR image is with 24-bit colour dept. Each of the colours is represented by 3 separate, 8-bit channels. The fluent transition from one colour to another is possible by reproducing the missing values by increasing or decreasing in range of 0 to 255 for each channel. The comparison of the colour is different for each transition because of the 3-channel digital encoding. Therefore it requires different logical approach. For example the comparison for the Black-Blue transition is represented by the following Boolean expression:

(9)

$$Res = \frac{C1.G + C1.R}{2} < \frac{C2.G + C2.R}{2}$$

Where *Res* is TRUE when *C1* (Colour 1) < *C2* (Colour 2). The green and red channels are represented as *G* and *R*. Comparison (9) is simple because Blue channel is always raising and because the digital representation of the Left transition colour (Black) is very simple – 0 (zero for each channel).

The complexity of comparisons for the rest of the transitions becomes polynomial.

The *Colour Transition Engine (CTE)* is a three pass algorithm:

- *Pass 1*: The pixels in the image are sorted in *transition groups*. Special evaluation function calculates the relative weight for each pixel in the groups;
- *Pass 2*: Groups are optimized by removing the duplicated colours;
- *Pass 3*: QuickSort algorithm is executed for each group using the calculated relative weight from Pass 1. Depending on the transition group this modification of QuickSort is working in ascending or descending mode.

The process speed is significant: 500 000 pixels are fully analyzed for 1-5 seconds. The speed varies because of the number of the discovered duplications.

The purpose of CTE is to create a colour palette from the source image. But one problem remains – the *colour pollution*.

3.3. Colour Pollution

The colour pollution is natural part of image encoding. It can be produced by the thermograph sensor sensitivity, by the image colour compression, by previous image optimizations or modifications, by applying additional information on the image like titles, labels etc.

The pollution is a relative quantity. It measures those colours which should not be included in the image palette. It is based on the fluctuation of the colour values which are outside the "normal" transition function scope.

The CTE controls the pollution levels by managing separately the colour channels for each pixel. The pollution detection algorithm is a logical part of evaluation function used during the Pass 1. This means that for each *transition group* the pollution criteria is calculated individually, as follows:

- The pollution detection affects only those colour channels in the current transition group which define the *colour deviation*. For example in the Black-Blue transition group the pollution affects only Green and Red channels;
- The pollution affects only the variable part of the channel within the current transition group. This part represents 100% of values that could be removed from the palette;
- The pollution removal algorithm works only between 1% and 50% of the selected for removal values. Once selected it affects as percentage all respective colour channels simultaneously.

Example:

The Black-Blue transition group allows Green channel to be blended between 0 to 255 and Red to be blended in range from 0 to 128. If the pollution removal is set to 50% it will remove all colours with containing values of Green and Blue more than 128 for Green and 64 for Red.

The colour pollution removal value is set in CTE to 50% by default.

3.4. Temperature Calculation

Once created, the IR image palette contains two sequential ranges of unique colours:

- temperature operational range
- garbage colours range (all colours removed during the pollution detection)

Because of *CTE*, the temperature range is already sorted. The sub-ranges are set correctly one after another – the first unique colour from the IR palette is the coolest one, the last from the operational range is the warmest.

The temperature values are distributed for each *operational* colour from the palette by calculating a relative offset $C_{offset}(T)$:

(10)

$$C_{offset}(T) = \sum_{0}^{C_T - 1} \frac{abs(T_{max} - T_{min})}{C_T - 1}$$

Where $C_T = C -$, C is the count of all unique colour from the palette, C_G is the count of the garbage colours, T_{min} and T_{max} identify the absolute global temperature range for the selected IR image. The colour temperature C(T) is represented as follows:

(11)

$$C(T) = T_{min} + C_{offset}$$

There are three density modes of temperature calculation:

- High: per each pixel
- Medium: average temp. using aperture size 3x3
- Low: average temp. using aperture size 5x5

Medium and Low approximations automatically excludes any garbage colours detected inside the apertures.

3.5. Statistical Aggregation

During the Pass 2 of *CTE* the algorithm calculates the occurrence of each unique palette colour.

4. EXAMPLE

Using the mathematical model described in Chapter 2 and implementation approach described in Chapter 3, the following software development creates measurement technology for IR images in bio-medicine field:

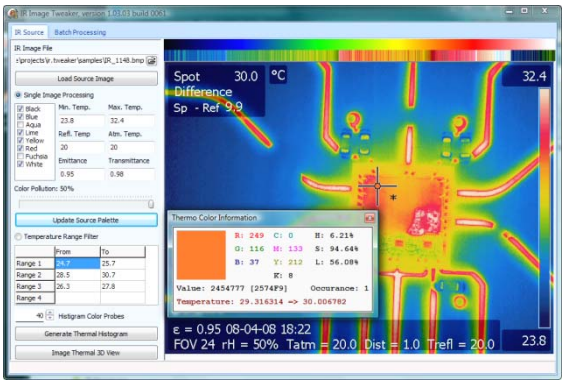

Figure 3. Colour Information provided by CTE

The IR image in *Figure 3* is captured with a standard thermo camera. Initially it was saved in JPEG file format and it was distributed as a raw BMP file format losing all camera information from the manufacturer. Taking in consideration the influence of the reflection power and the atmosphere transmittance, the image is processed with *CTE*. The calculated temperature of 29.31 °C is automatically corrected to 30.0 °C. This fully complies with the original temperature level captured by the thermograph.

The *CTE* helps to generate the image thermal histogram as it is shown in *Figure 4*. The occurrence of coldest and warmest colours is represented for the selected temperature range between 23.8 °C and 32.4 °C.

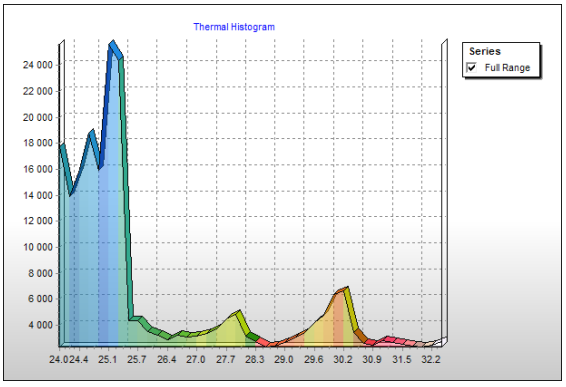

Figure 4. Example thermal histogram generated by *CTE*

5. CONCLUSION

The Colour Transition Engine works fast and very flexible with wide IR types of images. It allows being fully tuned-up by managing only few physical parameters. The CTE controls fluently the colour pollution and provides a great opportunity for direct processing of commercial images derived from thermographs produced by different manufacturers.

The CTE is designed as a thread-safe software library ready to be used in cell modules as a part of the parallel grid environments.

6. ACKNOWLEDGMENTS

The authors would like to thank for the support of Bulgarian Ministry of Education – Scientific Investigations Fond under which contract 1-854/2007 "Thermal Management of Microelectronic Systems (MC) – TEMC", the present work was conducted.

References

[1] FLIR Systems, *"Technical specification Issue"*, 1558550 Rev. a174, p. 243-244, 2005

[2] Robert Fisher, Simon Perkins, Ashley Walker, Erik Wolfart. "*Digital Image Processing",* HIPR2, John Wiley, 2004

SPACE CONFIGURATION OF LOW FREQUENCY MAGNETIC FIELD, GENERATED BY APPARATUS FOR MAGNETO-THERAPY USING GIRDLE COIL

Dimiter Tz. Dimitrov*, Miglena D. Dontshewa**

**Faculty of Telecommunications, Technical University of Sofia,*
8, Kliment Ohridsky str. 1000 Sofia, Bulgaria, phone: +359 2 9652278,
e-mail:dcd@tu-sofia.bg
*** Research Center for User-Centered Technologies , University of Applied Sciences*
Hochschulstr.1, A-6850-Dornbirn, Austria, phone +43 5572 7927303, e-mail: don@fhv.at

Abstract

An experimental investigation of space configuration of low frequency magnetic field generated by girdle coil is described in the paper.

The results of preliminary mathematical calculation and computer simulation of low frequency magnetic field of girdle coil are compared with the results of experimental measurements of module of magnetic induction in the girdle coils. The differences between results of calculation and results of experimental measurements are very small. Experimental histograms of space distribution of module of magnetic induction in the girdle coil in the case of static activation and in the case of "moved" magnetic field are given in the paper.

INTRODUCTION

It's well known that the space configuration of low frequency magnetic field in the patient's area is very important in the process of magnetotherapy[1,2]. Therefore the precise calculation of low frequency magnetic field as well as an easy-to-understand visualization of field distribution over the patient's area are of great importance for the reliability and predictability in the process of experimental measurement of magnetic induction of the constructed electromagnetic device. An electromagnetic device (girdle coil) has been constructed for use as a therapeutic tool in magnetotherapy (Fig. 1).

The calculation exposes a low frequency magnetic field solver that allows to evaluate the field strength throughout the volume influenced by the coil.

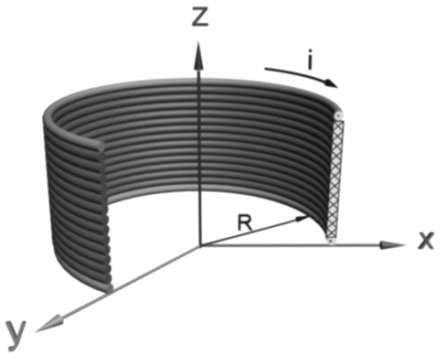

Fig. 1. Girdle coil

DESIGN STAGE

The evaluation of the low frequency magnetic field distribution and its visualization is a difficult task and usually requires a lot of time depend on the environment geometry and applied visualization techniques [1,2]. Additionally fields are often represented as large sums of field contributions of individual current turns. The calculation of field in space (off-axis form) requires field formulas that involve elliptic integrals or other complicated expressions that have to be approximated somehow. [3,4]

In the particular case the task is to evaluate the values of magnetic field induction at each point of the area of space enclosed into the coil with sizes according to the above Fig. 1. For the axial symmetry of the generated low frequency magnetic field the calculations can be performed only for the section perpendicular to the coil

plain and going through the center of the coil. To achieve better effectiveness of the calculations as well as to decrease the memory necessary to store the results, the values of magnetic induction are evaluated only for one half of this section (right half). Magnetic induction B is stored together with its two ingredients – radial component Bρ and axial component Bz for a future use to obtain vector form of accumulated field data.The magnetic induction B generated by a separate turn with radius R at an arbitrary point M in the girdle coil (Fig.2) is calculated using a method based on magnetic vector-potential .

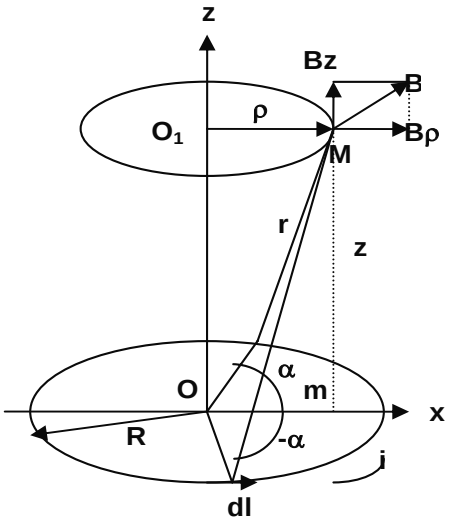

Fig. 2

The key equations used to calculate the two components components Bρ and Bz of magnetic induction B in a arbitrary point in the girdle coil:

$$B_\rho = \frac{\mu_0 i}{2\pi} \frac{z}{\rho\sqrt{(R+\rho)^2+z^2}}\left[\frac{R^2+\rho^2+z^2}{(R-\rho)^2+z^2}L - K\right] \quad (1)$$

$$B_z = \frac{\mu_0 i}{2\pi} \frac{1}{\sqrt{(R+\rho)^2+z^2}}\left[\frac{R^2-\rho^2-z^2}{(R-\rho)^2+z^2}L + K\right] \quad (2)$$

$$B = \sqrt{B_\rho^2 + B_z^2} \quad (3)$$

where:

K and *L* are full elliptical integrals;

R is the radius of the girdle coil (Fig.2);

ρ is the radius of an imaginary turn of the arbitrary point M (Fig. 2);

z is the vertical axis (Fig. 2);

i is the value of current in the girdle coil;

μ_0 is the absolutely magnetic permeability.

EXPERIMENTAL RESULTS

The presented article illustrates one approach to calculate and visualize a low frequency magnetic field distribution in 2D. The field is used for therapeutic purposes in magnetotherapy and is generated by a coil with a radius R into the range 200mm – 300mm. The coil consists of a number of current turns with the radius 1 mm. The results of calculation of magnetic induction can be compared with results of experimental measurement of magnetic induction, also. The histogram of experimental measurements of module of magnetic induction in the plane XOZ (Fig.1) can be seen on Fig. 3.

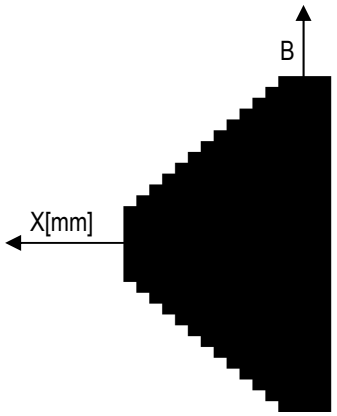

Fig. 3. Experimental histogram of the module of magnetic induction in the case of static activation of the girdle coil

Often the girdle coil consists several separate girdle coils, which can work as independent coils. This construction allow activation of the separate coils one by one and it can provide a "movement" of magnetic wave on the axis Z .A separate girdle coil can be seen on Fig. 4.

EXPERIMENTAL SETUP

A small coil (diameter $d = 8mm$, height $h = 10mm$ and current turns $w = 2x300$) has been used as sensor for measurement of the value of magnetic induction. This coil has been connected with the inputs of differential amplifier in the input of apparatus for measurement of

magnetic induction of low frequency magnetic field. The measurement has been done for the sinusoidal current in the girdle coil with frequency $f = 50Hz$. It's well known that the frequency band $f = 10Hz - 100Hz$ is used in the process of magnetotherapy. The sensor has been putted in different points around the girdle coil. The measurement of the gidle coil's current has been done by ordinary ampermeter. The measurement of module of magnetic induction on the axes X and Z (Fig, 4) has been done. The results of experimental measurements together with the results of calculation of the module of magnetic induction on axis X can be seen on Fig. 5.

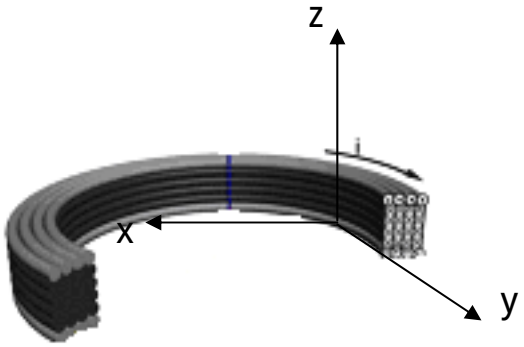

Fig. 4. A separate girdle coil

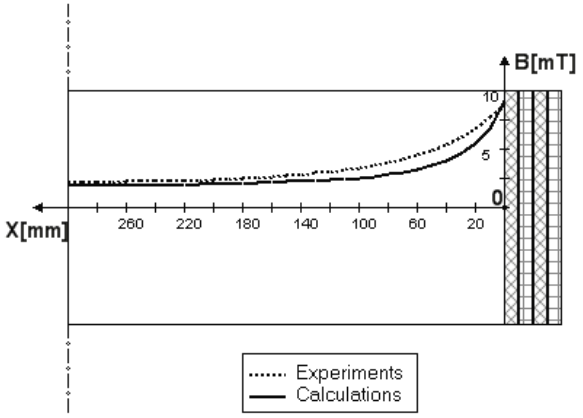

Fig. 5. Module of magnetic induction on the axis X

The results of experimental measurements together with the results of calculation of the module of magnetic induction on axis Z can be seen on Fig. 6.

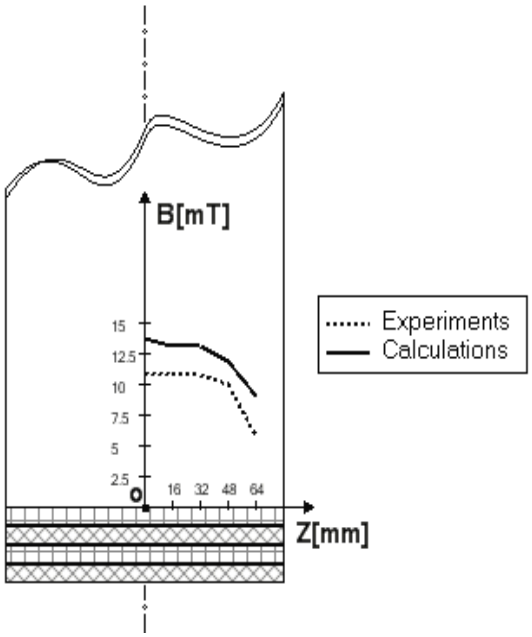

Fig. 6 Module of magnetic induction on the axis Z

LEVEL OF ERRORS

The main causes for errors between calculated and measurement results are: the finite sizes of the sensor, the permanent error of the place of sensors in it's putting in different points and orientation of it's axis (the angle between the vector of magnetic induction and the axis of sensor), the error of the measurement of current in the girdle coil, the influence of other magnetic fields with the same frequency $f = 50Hz$. Some of these errors have been reduced using differential coil as sensors. The results of calculation and results of experimental measurements are similar. It was the main goal of investigation. Of course it's possible to obtain more precise methods and measurement devices, but it's not necessary in the case of magnetotherapy, where usually the values of magnetic induction are 10-30mT and 10% error is acceptable. It's clear that only one small translation of the human body in the girdle coil would be enough for an error of the value of module of magnetic induction in an arbitrary point of the human body ,more than 10%. The value of relative magnetic permeability of live tissue $\mu_r \approx 1$ as in the air.

Therefore computer simulation can be used successfully for future investigation of space configuration of low-frequency magnetic field in the human body, also. This is the main conclusion of the above investigations.

EXPERIMENTAL HISTOGRAMS

Some experimental histograms of space distribution of module of magnetic induction in the coils can be seen on Fig.7a, Fig7b and Fig.7c in the case when the separate coils are activated one by one and the magnetic field "moves" on the axis Z .

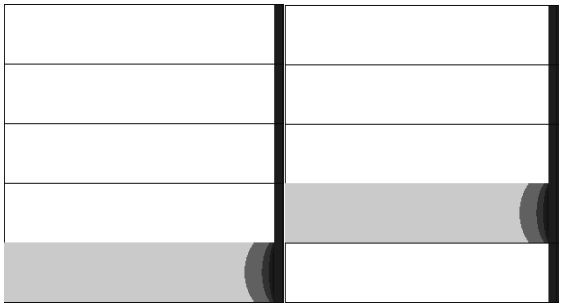

Fig. 7a

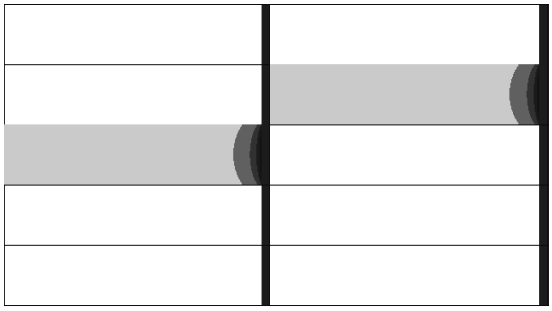

Fig. 7b

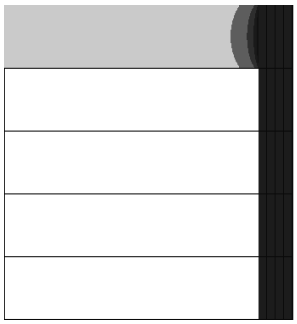

Fig. 7c

Fig. 7. Experimental histogram of the module of magnetic induction in the case of "moved" magnetic field

CONCLUSION

Visualization, calculation and experimental investigation of the space configuration of low frequency magnetic field in the patient's area is of great importance as preliminary result not only for the process of experimental measurement of the value of magnetic induction in magnetotherapy, but for evaluation of the effectiveness of developed electromagnetic devices, also. Additionally these two processes can be used to assist the design of such devices. Into the particular case of therapeutic magnetic field the calculation and visualization are intended to allow the user visually evaluate the strength of the field into the influenced area of space.

The data structures developed for geometric and calculated data representation are designed to store both radial $B\rho$ and axial Bz components of magnetic induction for future visualization of a vector field in 2D and 3D. At the implementation stage the data structures are chosen in such a way to allow data to be shared between different applications.

The experimental measurements of the module of magnetic induction in girdle coil confirms results, obtained by computer calculation.

REFERENCES

[1] Dimitrov, D. Tz. Computer Simulation of Space Configuration of Low Frequency Magnetic Field in Magnetotherapy, Electronics and Electrical Engineering, Nr. 3 (59), 2005, p. 28-32.

[2] Dimitrov, D. Tz. Visualization of a Low Frequency Magnetic Field, Generated by Girdle Coil in Magnetotherapy, Electronics and Electrical Engineering, Nr.3(59), 2005, p.28-32

[3] Foley, J. D., A. van Dam, S. Feiner, J. Hughes, Computer Graphics: Principles and Practice, Addison-Wesley, Reading, MA,1990

[4] Hearn, D., M. P. Baker. Computer Graphics, Prentice-Hall, NJ, 1997

RESEARCH ON THE INFLUENCE OF PERMANENT MAGNETIC FIELD DURING LIVE TISSUE LASER TREATMENT

Viktor V. Mihaylov
Kalin L. Dimitrov
Dimitar C. Dimitrov

Technical University of Sofia
Bulgaria, Sofia, 8 Kl. Ohridski St.
T.+359 2 965 3145; F.+359 2 3095; E. kld@tu-sofia.bg

Abstract

This paper deals with the quickly developing technology of the application of the joint action of laser treatment and permanent magnetic field. Measurements have been made and results have been derived for the case of wide-band receivers. The research has been done using two different sources working in different frequency ranges. The goal is to increase the spectrum researched in order to decrease the probability of error occurrences. The strongly selective characteristics of the tissue at different frequencies have been checked indirectly. The research has taken into account the restrictions defined which are prompted by the in vitro research. The need for controlled environment has been noted, the morphological differences from the live tissue have also been noted, and a plan for future measurements has been devised. The goal is for the gradually derived results to be maximally approximated to the practically applicable ones.

1. INTRODUCTION

For the last years there have been a series of researches on the influence of the permanent magnetic field over laser treatment, and some interesting results have been observed [1].

Two possible reasons for such effects have been observed. The first one is the Faraday effect or, more precisely, the influence over the environment between the laser source and the object treated. In this way one can influence the treatment polarisation. In this way one can influence treatment polarisation. However, no practical use of optical treatment polarisation control has been found yet. This is mainly due to the non-homogenous structure of flesh and the comparatively quick change of molecular level [2]. The second possible reason is the local influence of the magnetic field over the treated area. This is the most perspective way to earn benefit from the joint influence of optical and magnetic fields. In the paper, we have speculated on the second way.

2. THEORY

2.1. Problems with the choice of research method

There are several ways to measure the optical parameters of the tissue [2]. Depending on the experimental approach, one can derive the average coefficient of attenuation and the two coefficients of absorption and diffusion. If the angle dependence between the diffused energy is measured through twisting the respective detector, then the anisothropy coefficient can also be derived.

The simplest method for measuring the attenuation is presented in fig.1.

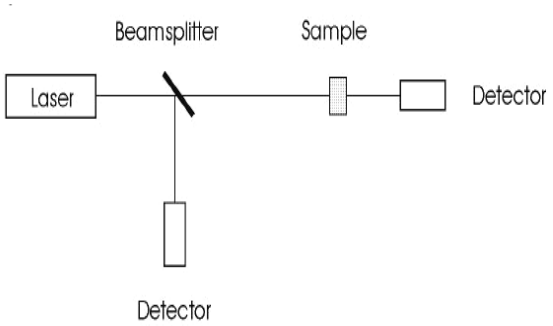

Fig.1. Measurement of the attenuation using a light divider

By using a light divider, half of the energy is directed to a comparative detector. Its other half is directed to the tissue sample. There is also a second detector located on the optical axis, which measures the energy that has passed. By subtracting the derived intensity from the one derived for the comparative detector, the attenuation coefficient can be derived. The problem with this set is that there is no way to differentiate between the absorbed and the diffused light.

Another method through which the absorption can be defined contains one more additional component: integrational sphere. This sphere has a high reflectional internal surface. An integrated detector measures only the light which has not been absorbed from the object inside the sphere.

Another problem with the measuring process is the property of the biological tissue to change its paramaters during the process of irradiation due to heating. That is why it is important that measuring is done simultaneously and with the same model of the set. Another problem is the non-homogenity of biological tissue. This hinders the comparison of experimental results from different test probes. Optical characteristics measured in vitro can differ significantly from the in vivo ones. There are a number of reasons: the tissues have different morphological structures; the tissue changes easily as a consequence of deformations and drying, freezing or dipping in liquids.

2.2. Choice of optical source

In the practical research we will use two different sources working in different wavelengths. The goal is to expand the spectrum researched and reduce errors.

It is known that tissue has very selective characteristics for single wavelegths.

For a first source we will use an infrared LED. Advantages of infrared LEDs are higher emitting power as well as higher effectiveness and optical penetration. The infrared light is absorbed mainly in water molecules: this defines great differences in the results in vivo and in vitro. The research of prof. H. Freedmann [1] also includes infrared LEDs.

For the second source we will use a He-Ne gas laser [3].

The average wavelength is 632.8 nm. With such a wavelength, there is a relatively good absorption, mainly from pigments and proteins.

2.3. Choice of measuring equipment and experimental object

We choose the research media (biological tissue) to be *in vivo*.

In this way the derived results will be maximally approximated to the practically applicable ones.

We also take into account the restrictions defined which are prompted by the in vitro research: a controlled environment is needed, also morphological differences from the live tissue and the lack of available equipment. For the research we choose the surface of the fingers.

The construction of the receiver has to be of such a type, so as to be stably fixed to the tissue.

3. EXPERIMENTAL SETUP

3.1. Basic parameters

Intensity of the optical radiation -10mW/ cm^2, Bandwidth – 600-1000nm; Magnetic Induction - 35mT. Used in the setup infrared LED is L200CIR941,made by Ledtronics Inc. For the second emitter we use He-Ne laser. Maximum output power of the used laser P = 3mW ($\lambda = 632.8nm$); Maximum output radiance of the infrared LED J = 50mW/sr; Radiant angle of the LED d = $\pm 20°$ = 0.35rad; Radiant angle of the He-Ne laser $\leq 0.48mrad;$) Within this wavelength ($\lambda = 632.8nm$), there is relatively good absorption from pigments and proteins.

For the optical flux receiver of infrared light we are going to use a photodiode with integrated transimpedance amplifier TSL260 produced by Texas Advanced Optoelectronic Solutions.

For the optical sensor of the He-Ne laser we are going to use power meter Wilcom FM8510 Power Meter 850/1310/1550 InGaAs. Dynamic range - +5dBm to -70 dBm, respectively with central wavelengths at 850,1310,1550 nm. Resolution – 0.01dB.

For the source of constant magnetic source we chose series of 8 tabular Neodymium magnets - Nd2Fe14B, with measures 1x4x4 cm. Of all know ferromagnetic alloys, this one has the highest remnant static magnetic field Br=2000-3000Gauss, coercitive force H_c=235-270kA/m and maximal magnetic energy $(BxH)_{max}$=27-35kJ/m^3. We chose the Neodymium magnets because of their high magnetic characteristics, relatively small price and compact size. Separate magnets make possible the regulation of the magnetic field by using them in different combinations.

3.2. Calculations

We calculate the intensity I of the laser beam by its given maximum output power:

(1) $$I_0 = \frac{P}{\pi \omega_{1/e}^2} = \frac{3.10^{-3}}{3,14.\omega_{1/e}^2}$$, and

(2) $$\omega_{1/e}^2 = \frac{\omega_{1/e^2}}{\sqrt{2}} = (0,707.0,83)^2,$$

This results in:

(3) $$I_0 = \frac{3.10^{-3}}{3,14.0,344} = \frac{3.10^{-3}}{1,082} = 2,77\ mW/sr$$

Where P is the radiant power in units of W, $\omega_{1/e}$ is the beam radius specified at the 1/e points defined by Gaussian-shaped beam profile. This beam radius is defined as the radius of an aperture that will just accept 63% of the incident power, i.e. 1/e of the incident power is blocked. We calculate roughly the absorption of the media and the absorption length of the laser radiation. The skin is one of the tissues with highest absorption properties. For this we assume the minimal depth of propagation in the turbid media to be 1mm and the maximal 5mm. The absorption coefficient of the medium (skin) is α=268cm^{-1}, we have the proceeding results:

(4)
$$I(x) = I_0 e^{(-\alpha z)} = 2,77.e^{-0,268.0,1} = 2,77.0,973 = 2,696\ \text{mW/sr}$$

(5)
$$I(x) = I_0 e^{(-\alpha z)} = 2,77.e^{-0,268.0,5} = 2,77.0,874 = 2,423\ \text{mW/sr}$$

(6) $$L = \frac{1}{\alpha} = 3,731cm$$ – absorption length.

3.3. Experiments

Measurement of the optical properties of the He-Ne laser, while adding and removing the constant magnetic field. We perform series of measurements with different amplitude of the applied magnetic field. No variations of the measured intensity of the transmitted through the tissue radiation are observed. The only source of alternation of the gathered results in the presence of fluctuations from the displacement of the tissue relatively to the emitter, heat variations due to overexposure of the powermeter's thermal sensor and the received reflection from the surface of the magnet.

By analogy, we perform the same way the measurement of transmitted intensity of the infrared LED. No variations of the measured intensity of the transmitted through the tissue radiation are observed.

There is no apparent change in the dielectric properties of the tissue, side effect of this would be increased or decreased losses. Both magnetic and laser fields can change the morphological structure of the substances.

4. CONCLUSION

4.1. General conclusions

The used methods for measuring tissue parameters can be used for future research with the goal of practical application when solving a particular engineering problem.

The restriction in the number of the different methods of measuring optical parameters leads to a significant decreasing of the problem-solving time for problems of a similar nature.

The comparative wide-band irradiation as well as the weak sensitivity of the measuring equipment are the main reasons for the derived results.Also thus introduced, the investigated medium, consist a lot of unknown parameters. The short duration of the research also restricts the derived results.

4.2. Future development

The application of a spectral analyser for the research. In this way the integration of the field intensity in wide-band detectors will be avoided.

Choice of other tissue samples. Application of Electron paramagnetic resonance analyzer in order to achieve a highly sensitive measuring of the electron transfer and the synthesizing of free radicals in the researched environment, monitoring the spectrum of paramagnetic resonance emitted from the specific object.

References

[1] H. Friedmann, et all, "Towards a Mechanism of Low Energy Phototherapy", Laser Therapy, Vol. 3, No. 1, Jan. Mar, 1991, pp.11-13.

[2] M. Niemz, *Laser-tissue interactions. Fundamentals and Applications*, Springer, 2007.

[3] E. Ferdinandov, *Laser radiation in radio technique*, Sofia, Technika, 1981.

[4] J. Malmivuo and R. Plonsey, *Bioelectromagnetism - Principles and Applications of Bioelectric and Biomagnetic Field*, Oxford University Press, 1995.

[5] J. Vazquez de Aldana, "Magnetic-field effect in atomic ionization by intense laser fields", *Optics Express*, Vol.5, No7, USA, 1999, pp.144-148.

[6] D. Dimitrov, "*Medical Systems for influence of electromagnetic field on the human body*", Publisher of TU-Sofia, 2008.

[7] H. Friedmann, et all, "Basic research Proves efficiency of magnetic and laser field combination in phototherapy",Publisher Bar Ilan University, 2007.

INVESTIGATION OF TRIPLE PLAY SERVICES

Valentin Hristov, Mario Kanchev

South- West University – Blagoevgrad,
66 Ivan Mihajlov Str, Blagoevgrad, Bulgaria
Phone (+359)738889132; E-mail v_hristov@aix.swu.bg .

Abstract

Today there are three main mass communication services- telephony, television and Internet (conditionally, data). In past they were divided technologically and organizing: each was base on the own infrastructure/facilities, accordingly, different operators. For the user this looked as a telephone wire, television cable and Internet wire or wall-plug. Today, multiservice network's operator, which provides its users broadband IP connection (with speed not less than several megabits per second) can provide simultaneously these three the most mass and accustomed services through IP. This way of granting the services is named Triple Play.

The present paper aims at creating model, which simulates processes in the system, build on the principle of Triple Play and getting statistics about: Blocking probability of voice requests; Average time spent in the queueing system of video requests; Average time spent in the queueing system of data request and etc.

1. INTRODUCTION

An important challenge in triple play networks is satisfying the requirements of different types of traffic (voice, video and data) within a single network. Real-time traffic e.g., voice and video require low, predictable delay in transmitting information from one location to another (end-to-end) or the result may be a distorted voice or videos received at the destination. On the other hand, elastic traffic e.g., data transmissions, e-mail, and file transfers not as sensitive to timing constraints, but are usually very sensitive to lost data. In earlier work [3] we find that packet losses in network nodes are very different depending on the ratio of different types of traffic sharing capacity of the network connections.

The problem of capacity sharing in the network was earlier researched for narrowband networks in terms of homogeneous utilizations (See [1] and its references). While VoIP telephony has been extensively studied in [6] and [7], blocking probability and setup time for telephony calls have received relatively less attention. The blocking probability and setup time has a direct impact on the users' satisfaction: The user is used to waiting a maximum of eleven seconds as specified in [8] and expects to experience the same even if the technology is different. Therefore, the blocking probability for telephony calls as well as average time spent in the queueing systems of video and data requests should be estimated and optimized. This is the motivation behind this article.

2. MODEL

In triple play networks the capacity of network is shared between voice, video (video on demands- VoD) and data. Under voice requests are implied telephony calls. Video request present itself inquiries for viewing a television (IPTV) or concrete videomaterial (VoD). Data requests are considered the data from applications, e.g. data transmissions, e-mail, and file transfers (encapsulated in IP packets), which are sent through Internet connection.

For processing these three type requests (named servers) some resources should be used. For each traffic type are dedicated a certain number of servers, i.e. voice server/s, video server/s and data server/s.

On fig. 1 corresponding Q – scheme is depicted. Each voice, video or data channel is approximated as a input buffer (Q1, Q2 or Q3), and server/s (VoS, ViS, and DS) for voice, video and data. The implementation in corresponding

General Purpose Simulation System (GPSS) model is based on the algorithm proposed in [4].

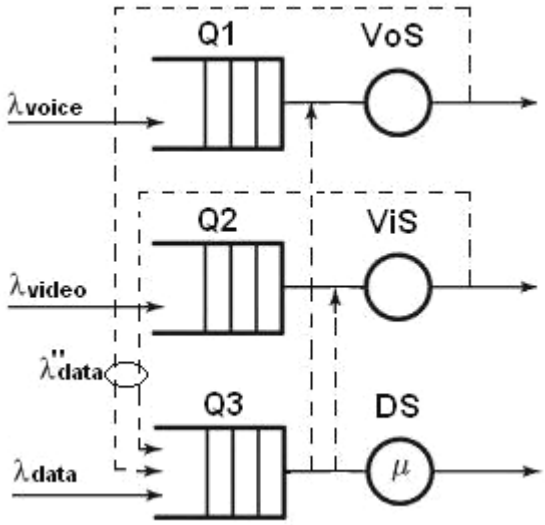

Fig. 1

As can see on fig.1 there are three types servicing in queuing systems which can be classified as follows:

- Priority service for voice and video requests in corresponding servers. The selection of a packet from the voice/video or data queue depends on priorities that are permanently assigned to these packets;

- First come, first served is realized by data server for data requests. Data packets are served by data server in the order they arrive;

- Preemption for data requests in voice and video servers. The data packet currently being serviced can be interrupted and preempted if a higher priority packet arrives in the queue. This is secondary data request (fig. 1).

As mentioned above maximum of session setup time [8] for telephony call (VoIP) is 11 seconds if triple play technology is used. Therefore, the principle of using the voice server(s) for processing the voice requests is following: new voice request is queued if all voice servers are occupied by processing the voice requests (received earlier); Every time when a voice request/transaction departs the queue and tries to enter in voice server, its time spent in the queueing system is checked; If it is less than 11 sec. the voice request enter in this server; Otherwise, this voice request is reported as blocked.

Video request enter in the queue (buffer) when all video servers are occupied by processing the video requests. Data requests can be serviced by data- , voice- and video- servers. If any voice and video server is free, the data request will get up on service. However, this data request will be displace from there in case of arrival voice or video request, corresponding (voice and video request have high priority).

The intervals between arrivals of (data, voice and video) requests are assumed with the exponential law of distribution, as enough realistic. The distribution of servicing times for the all three type requests is assumed with the exponential law, too.

Each one type of requests (data, voice and video) has different average interval between arrivals of requests or intensity, correspondingly, as well as different mean time of servicing.

2.1. Constants and parameters

For voice requests the mean time of servicing by voice server is $1/\mu_{VOICE}$ = 98 seconds. This is average length of occupation of individual phone line in hour of the most load [2]. The mean time of servicing of video requests is $1/\mu_{VIDEO}$ = 13600 seconds (TNS Gallup Media affirms that people looks a television 227 minutes per day). The mean time of data requests is $1/\mu_{DATA}$ = 100 seconds (this value was received as a result of statistical investigation of traffic from Bulgarian news sites).

The other parameter in model is servers' utilization (loads), $\rho = \lambda / \mu$ or the intensity of input flows or correspond to average interval between arrivals of requests. In order to achieve desired load in the model following formula is used to calculate average interval between arrivals of requests (transactions):

(1) $$\rho = \lambda / \mu \Leftrightarrow 1/\lambda = \rho / \mu$$

where

μ - mean time of servicing of corresponding type request;

ρ - value of initial load, is defined on formula;

λ - intensity of input flow requests, or $1/\lambda$ - average interval between transactions' arrivals.

In model is used a certain constants for number and states of servers: The amount of

servers dedicated for voice, video and data requests are described with Num_of_VoS, Num_of_ViS, and Num_of_DS; The states of servers are described with following constants: 0 - is free, 1 - is occupy by processing a voice request, 2 - is occupy by processing a video request, 3 - is occupy by a data request.

In model a transaction parameter identifies type of the request: 1 - a voice, 2 - video, 3 - data. Another transaction parameter (at the secondary data requests)- P$residual_time is used for writing the time that remains to be service this transaction corresponding to data request.

2.2. Data requests

After data transaction is generated, the modeling system is examined for presence of free servers starting with data servers: If amongst them there is free, the request will be serviced by the found free data server. If there is not, the voice and video servers are examined. If after checking all servers free server was not found, the request enters in the queue and waits, while a server will not be free. After the completion of processing the request is removed from the system. Note, the role of secondary data requests and P$residual_time parameter when processing such request: If the value of this parameter is more than zero, this signifies that this request/ transaction has been displaced (while it is serviced by a voice or video server/s) and its remaining time of servicing is this value.

2.3. Voice requests

After voice transaction is generated, the system is examined for free voice server/s. If amongst them there is free, the request will be serviced by the found free server. If there is not free server, the system is examined for voice server which services a data transaction. If there is at least one server satisfying this condition, the processing of this data request is displace (it is moved in the queue) and voice transactions enters to be serviced in already freed server. The voice request is reported as blocked, if this waiting for server more than 11 seconds (and its corresponding GPSS transaction is terminated).

2.4. Video requests

Processing of the video requests is similarly as processing of voice requests. The only one exception is when free video server absences the request is not blocked (corresponding to this request transaction enters in the queue).

The statistical results received by modeling are written in the CSV-file which format is compatible with MS Excel.

3. VERIFICATION AND SIMULATION RESULTS

Verification is made as results from simulation model for three voice servers (Simulation of VoS and ViS servers is similar but more simple) are compared with these for M/M/a/a system (a=3).

Ro	Erlang-B	Pb	Error , %
0	-	0	0
0,1	0,003334568	0,00333	0,13
0,2	0,019823789	0,02098	5,83
0,3	0,05007212	0,0494	1,34
0,4	0,089775561	0,08957	0,23
0,5	0,134328358	0,132746	1,18
0,6	0,180267062	0,18091	0,36
0,7	0,22537782	0,224228	0,51
0,8	0,268406337	0,270692	0,85
0,9	0,308738412	0,311504	0,9
1	0,346153846	0,344573	0,46

Table 1

Bellow, for purposes of the verification, estimations of blocking probability are compared with results for blocking probability computed by the Erlang-B formula, as well as corresponding table is fill. Erlang-B formula calculates the probability that an arriving packet finds all servers busy but no waiting line for packets in the M/M/a/a system, or queueless model:

$$(2)\quad P\left[k(t)=a\right]=\rho_a=\frac{\rho_1^a}{a!}\rho_0=\frac{\rho_1^a}{a!\left(\sum_{i=0}^{a}\frac{\rho_1^i}{i!}\right)}$$

where: p_0- the probability of the first state; a – number of servers; ρ_1 - load of each server in the M/M/a/a system ($\rho_1 = a.\rho$).

The difference between the blocking probability and its estimation is shown in last column in tabl.1. Unlike the difference for smaller values of utilization, e.g. ρ=0.2 which is 5.83%, the difference generally is less than 1.4%. So, because the GPSS model for smaller values of utilization is not pure M/M/3/3 system (there are significant number of voice request with queueing time less than 11 seconds, which are serviced, i.e. not blocked), it is useful to verify it with Erlang-C formula. This formula calculates the probability that an arriving packet finds all servers busy in a M/M/a system. This probability is the same as the probability that the waiting time for the packet in the queue is greater than zero, or the probability that the number of packets in the queueing system is greater than or equal to a=3:

(3) P [K(t) ≥ a]= $p_a/(1-\rho)$, where

p_a- the probability that all *a* servers are in use:

$$p_a = \frac{\rho_1^a}{a!} p_0$$

where: p_0- the probability of the first state. For the M/M/3 discipline, ρ = λ/aμ = 0.1 (a = 3 servers are used, thus, ρ_1 = λ/μ = 0.3):

$$(4)\quad P_0 = \frac{1}{\sum_{i=0}^{a-1} \frac{\rho_1^i}{i!} + \frac{\rho_1^i}{a!}\frac{1}{1-\rho}} = \frac{1}{\sum_{i=0}^{2} \frac{\rho_1^i}{i!} + \frac{\rho_1^3}{3!}\frac{1}{1-\rho}} = 0,7407407$$

Consecutively, substituting in (3) p_a=0,0033333, and P [K(t) ≥ 3] = p_a / (1 - ρ) = =0,003333/0.9=0,0037037.

The estimation of blocking probability (from simulation) is Pb= 0,0033333. The difference between the blocking probability and its estimation is less than 10%, which is acceptable for engineering purposes. Increasing system load leads to higher difference between these values, e.g. for ρ=0.3 (ρ_1=0.9) the blocking probability computed by the Erlang-C formula is P [K(t) ≥ 3]= 0,0700288, but the blocking probability from simulation is Pb=0,0494. Thus, the difference is 29%, which is acceptable keeping in mind that (about simulation) a voice requests is blocked if its queuing time is greater than 11 sec. and we can conclude that proposed model is adequate [1].

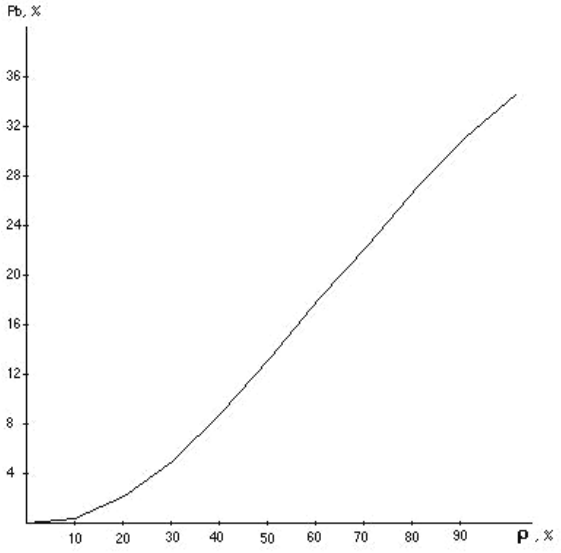

Fig. 2

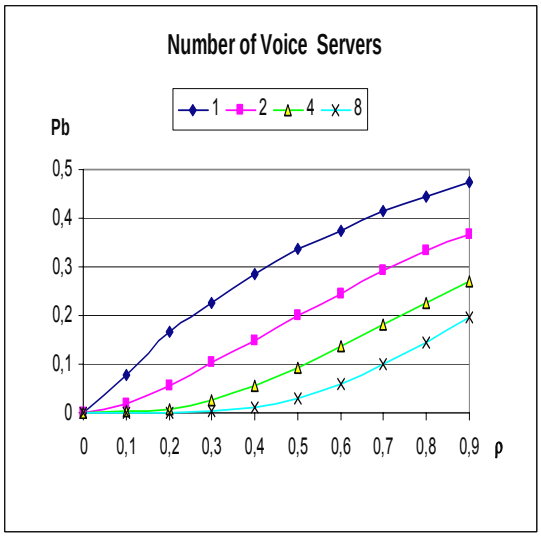

Fig. 3

On fig. 2 is depicted the blocking probability of voice requests- Pb vs. load of each voice server for three voice servers. Increasing the system load in voice channel leads to higher blocking probability of voice requests.

On fig. 3 is depicted the blocking probability of voice requests vs. load of each voice server for different number of voice servers. Increasing

the number of voice servers for all system loads leads to lower blocking probability of voice requests (fig. 3).

Analogically, increasing the number of video servers leads to lower average queueing time of video requests- E[Tq] (fig. 4).

The results from figures 3 and 4 are logical due to statistical multiplexing at processing of voice/video requests from voice/video servers

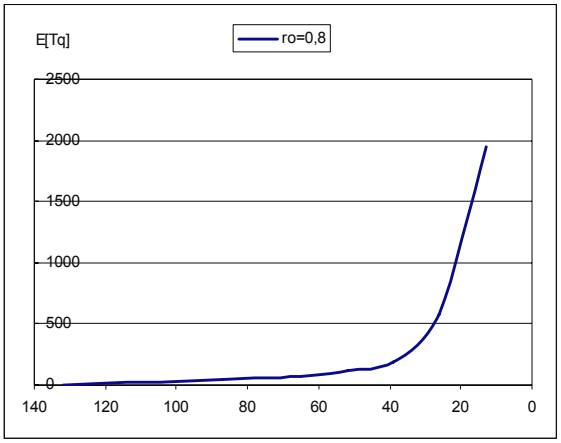

Fig. 4

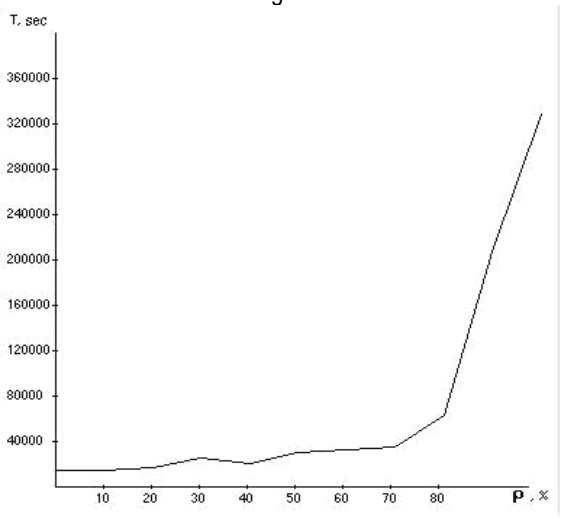

Fig. 5

On fig. 5 is depicted the average time spent in the queueing system of video requests vs. load of video server (the number of video servers is fixed to one). Increasing system loads in video channel leads to higher average time spent in the queueing system of video requests (fig. 5).

4. CONCLUSION

As this example shows, the proposed model gives us the opportunity of quickly comparing different situations corresponding to different values of the system parameters, for engineering purposes.

Keeping in mind simulation results depicted on fig. 2 and 3, we can conclude that it is useful to increase the number of voice servers in triple play networks.

References

[1] Сурихин П. Л., Пономарев Д. Ю, Исследование вероятностно-временнных характеристик однофазных систем массового обслуживания с ограниченной очередью с помощью имитационного моделирования // Сборник научных трудов. Красноярск ИПФ – 2003., с. 420-425.

[2] Шелухин О.И. и др. Фрактальные процессы в телекоммуникациях. - М.: Радиотехника, 2003.

[3] Hristov V., et al. Efficient Sharing of the Capacity for Different Types Traffic in Multiservice Networks. Proc. of the Conference ELEKTRONIKA'-2008, Sofia, ISBN 954-90209-3-2

[4] Hristov V. , GPSS Simulator of Multiservice Networks, on-line available on: ice.prohosting.com/vhristov/smn.gps

[5] Panagiev, O. B. Nonlinear systems modeling in broadband communications. ICEST, Proc. of Papers, vol.1, Ohrid, 24-27 June 2007, pp. 321-324

[6] B. Goode, "Voice over Internet Protocol (VoIP)," Proc. IEEE, vol. 90, no. 9, 2002.

[7] A. Valko, A. Racz, and G. Fodor, "VoIP QoS in Third-Generation Mobile Systems," IEEE J. Selected Areas in Comm., vol. 17, no. 1, Jan. 1999.

[8] T.S.S. of ITU, "ITU-T Recommendation E. 721—Network Grade of Service Parameters and Target Values for Circuit-Switched Services in the Evolving ISDN," 1991.

INVESTIGATION OF 802.11 N WLAN THROUGHPUT

Valentin Panchev Hristov, Ivaylo Veselinov Petrov

South- West University- Blagoevgrad,
66 Ivan Mihajlov Str, Blagoevgrad, Bulgaria
Phone (+359) 886271831; E-mail: ivaylo_veselinov@mail.bg

Abstract

The latest generation of high-speed wireless LAN solutions, based on the Institute of Electrical and Electronics Engineers (IEEE) Draft 802.11n standard, are available for more than a year.

The 802.11n standard offers several advantages over previous wireless LAN technologies. The most notable advantages are substantially improved reliability and greater application data throughput.

The aim of this paper is to analyze the WLAN throughput through measurements based on real wireless network with 11N devices and special monitoring and measurement software.

1. INTRODUCTION

IEEE 802.11 n offers dramatic improvements in speed, range, and reliability. However, understanding its design and configuration requirements is crucial if organizations are to take advantage of its full potential. Current wireless solutions operate in the 2.4-GHz radio frequency band (802.11g and 802.11b) or the 5-GHz radio band (802.11a). Solutions based on the 802.11n standard will operate in the 2.4-GHz, the 5-GHz radio band, or both bands, offering backward compatibility with preexisting 802.11a/b/g deployments. The 802.11n standard is expected to deliver data rates of up to 300 Mbps per radio in 2.4 Ghz spectrum and up to 600 Mbps in 5Ghz spectrum. The industry is working aggressively to try to ensure that existing 802.11n draft 2.0 products will be able to be software upgraded to the final 802.11n standard. Now, the prestandart 802.11 n is in Draft 4.0, the official TGn workgroup is not expected to finalize the amendment until December 2009.

The important characteristics of the 802.11 n are: Orthogonal Frequency Division Multiplexing; Multiple Input Multiple Output technology; packet aggregation; channel bonding; wider coverage and backward compatibility with existing platforms.

Unlike the highest encoder rate in 802.11a/g is 3/4, this is increased to 5/6 in 802.11n, i. e. 11 percent increase in data rate. With the improvement in radio frequency technology, it was demonstrated that two extra frequency subcarriers could be squeezed into the guard band on each side of the spectral waveform and still meet the transmit spectral mask. This increased the data rate by 8 percent over 802.11a/g. Lastly, the waveform in 802.11a/g and mandatory operation in 802.11n contains an 800 ns guard interval between each orthogonal frequency-division multiplexing (OFDM) symbol. An optional mode was defined with a 400 ns guard interval between each OFDM symbol to increase the data.

Multiple Input Multiple Output- MIMO enabled access points use spatial multiplexing to transmit different bits of a message over separate antennas, providing much greater data throughput and allowing for more robust, resilient wireless LANs. Whereas previous wireless technologies had problems dealing with signal reflections, MIMO actually uses these reflections to increase the range and reduce “dead spots” in the wireless coverage area. This performance gain is a result of MIMO smart antenna technology, which allows wireless access points to receive signals more reliably over greater distances (and allows clients to operate at higher data rates) than with standard diversity antennas. Multipath scenario, or multiple transmission paths of the same data in a wireless broadcast

begin to interfere with each other, degrading network performance and shrinking the coverage area of the network. MIMO aims to change all that by using multipath to its advantage. The smart antennas on a MIMO AP can hand off reception and transmission dynamically to each other, adjusting for the clearest data path on the fly. This increases both range and throughput at any given distance in an indoor setting, especially in multipath or interference-phone environments.

In conventional wireless transmission methods, the amount of channel access overhead required to transmit each packet is fixed, regardless of the size of the packet itself. As data rates increase, the time required to transmit each packet shrinks, but the overhead cost remains the same, potentially becoming much greater than the packet itself at the high speeds delivered with 802.11n.

802.11n technologies increase efficiency by aggregating multiple packets of application data into a single transmission frame. In this way, 802.11n networks can send multiple data packets with the fixed overhead cost of just a single frame. *Packet aggregation* is more beneficial for certain types of applications such as file transfers due to the ability to aggregate packet content.

The most straightforward way to increase the capacity of a network is to increase the operating bandwidth. However, conventional wireless technologies are limited to transmitting over one of several 20-MHz channels. 802.11n networks employ a technique called *channel bonding* to combine two adjacent 20-MHz channels into a single 40-MHz channel. The technique more than doubles the channel bandwidth. Channel bonding is most effective in the 5-GHz frequency given the far greater number of available channels. The 2.4-GHz frequency has only 3 non overlapping 20-MHz channels. Therefore, bonding two 20-MHz channels uses two thirds of the total frequency capacity. Therefore, the IEEE has defined rules on when a device can operate in 40MHz channels in the 2.4GHz space to ensure optimal performance.

The aim of this paper is to analyze the WLAN throughput through measurements based on real wireless network with 11N devices and special monitoring and measurement software.

This paper is divided into two parts, the first part describes the experiments in 802.11n WLAN infrastructure mode, and the second – the generalized results.

2. 802.11N THROUGHPUT TESTING AND MEASURMENT

All tests and measurements are accomplished in laboratories in South-West University – Bulgaria. The wireless network equipment which is used is D-Link and Trendnet 802.11 n Draft 1.0 devices as follows [7]:

D-link	DIR-655 Extreme Wireless N Router
	DIR-635 Rangebooster Wireless N router
	DAP-1353 Wireless N Access Point
	DWA-547 Wireless N Desktop Adapter - PCI
	DWA-140 Wireless N USB Mini Adapter
	DWA-643 Wireless N Express Card Notebook Adapter
	DWA-650 Wireless Rangebooster Cardbus Notebook Adapter
	ANT24-600 – 2.4GHz 6dBi Directional Indoor Antenna
	DWL-R60AT – 2,4 GHz 6 dBi Directional Patch Indoor Antenna
	DWL-50AT -2.4 GHz 5 dBi Gain Dipole Indoor Antenna
	ANT-24 -2.4 GHz 5 dBi Omni-directional Indoor Antenna
Trendnet	TEW-621PC – 300 Mbps Wireless N-Draft PC Card

Table 1. WLAN hardware

All N devices work in 2.4 GHz (2.4-2.4835 GHz) spectrum, compatible with IEEE 802.11 b/g/n , max EIRP Power – 100 mW, theoretical data rate -300 Mbps.

The PC-s used in tests are full compatible with the minimum system requirements of the WLAN devices. The operation system is MS Windows XP Professional SP2.

Software used for measurements, monitoring and site survey is shown in tabl. 2.

AirMagnet Laptop Analyzer Pro	Ver.7.6 Build10264
Passmark Performance Test	Ver. 6.1
Celetrio Covera Zone	Ver. 2.1
DU Meter	Ver.4.0Build R3009

Table 2. WLAN software

Configurated test wireless network in infrastructure mode – Independent Extended Service Set (IESS) with two access points and wireless hosts (clients) is shown in fig. 1.

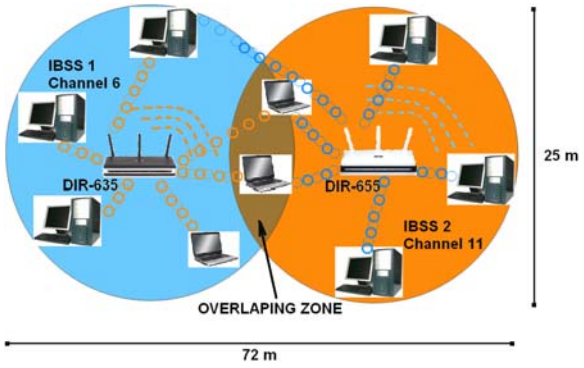

Figure1. Block diagram of tested IESS

The 2.4 GHz band is broken down into 11 channels for North America and 13 channels for Europe. These channels have a center frequency separation of only 5 MHz and an overall channel bandwidth (or frequency occupation) of 22 MHz. The 22 MHz channel bandwidth combined with the 5 MHz separation between center frequencies means there is an overlap between successive channels. Best practices for WLANs that require multiple access points are set to use non-overlapping channels. If there are three adjacent access points, use channels 1, 6, and 11.We use in our test 6 (2427MHz) and 11(2452MHz) channels.

The channel bonding is 40 MHz. The distance between APs is 45 m. Between IBSS1 and IBSS2 is important to have a 15% (or more) overlapping zone for best communication and data transfer.

Overhead is the major fundamental issue for WLAN inefficient, and it includes MAC and PHY headers, frame check sequence- FCS, interframespaces- IFSs, backoff time, and ACKs. Define normalized overhead as overhead divided by data rate. Let T_{slot}, T_{SIFS}, T_{DIFS}, and $CW_{\min}$ denote a slot time, a short IFS (SIFS) time, a differentiated IFS (DIFS) time, and the minimum backoff contention window size, respectively. Let T_P and T_{PHY} denote transmission times of a physical preamble and a PHY (Physical Layer) header, respectively.Let T_{DATA} and T_{ACK} denote transmission times of a data frame and an ACK, respectively. Assume that all data frames are the same size, and at all times frames are concatenated. The Maximum Throughput [1] is given as:

$$MT_a = \frac{8k * L_{DATA}}{kT_{DATA} + T_{ACK} + T_{DIFS} + T_{SIFS} + (CW_{\min} - 1)T_{slot}/2} \quad (1)$$

With Airmagnet Laptop Analyzer Pro [10] are measured throughput, utilization, signal strength on MAC sublayer on the base of the network traffic (downlink and uplink) passing through special full compitable WLAN adapter TEW-621PC installed on notebook. The test duration is 3 hours. Performance Test [11] measures the average and maximum throughput on TCP ports: 80 (HTTP), 21 (FTP), 23 (Telnet), 25 (SMTP), 53 (DNS) and on UDP ports: 53(DNS), 69 (TFTP), 161 (SNMP), 520 (RIP).Each test duration is 200 s. The transmitted frames can be with fixed or variable block size. Unlike Transmission Control Protocol- TCP which is a connection-oriented and reliable transfer protocol, User Datagram Protocol- UDP is a connectionless protocol, which means it is an unreliable means of data transfer. UDP provides no checking of the transferred or received data.

In tests are used different types of antennas and different distances between the transmitter and the receiver (see bellow).

3. RESULTS

Summary of the results are presented at this section. The highest throughput that is measured is 293,7 *MBps* for interval of 11,2 sec., but this data rate is not constant, and the transmission of this rate is still impossible in Draft 1.0 on 2.4 GHz. The throughput is strongly dependent of the building infrastructure, walls material, signal fading, SNR, RF interference and antennas gain and diversity.

Having a standard configuration of WLAN devices, at the same distance of 52m between transmitter (DWA-140) and the receiver (DWA-547), at 2.4 GHz, on 11 channel is measured with Performance Test 6.1 the following throughput:

Port Number	Throughput , Kbps
TCP	
80	2638,9
21	1703,5
23	1575,4
25	1298,9
53	1586,8
UDP	
53	5290,9
69	5354,8
161	5243,2
520	4408,8

Table 3. TCP and UDP Throughput

It is used variable block size of data frames (from 20÷100 Bytes). Each test transmission lasts 200 sec.

In the same conditions, but with changed gain antennas of the router DIR-655 and the receiver DWA-547 is measured the throughput. On the DIR-655 are installed one directional antenna DWL-R60AT and two omni-directional antennas DWL-50AT. The receiver DWA-547 is with one ANT24-600 and two ANT-24. The achievable throughput on UDP is about 10 times higher than devices with standard antennas (2 dBi).The directional antennas are on the same line, one opposite another. The gain of the directional antennas is 6 dBi. The results are shown in the Table 4.

UDP	Throughput, Kbps	
Port Number	Variable Block Size	Fixed Block Size - 16384 B
53	42183,0	51306,0
69	53726,0	50777,0
161	54177,0	52087,0
520	53851,0	51342,3
1040	54696,9	22749,1

Table 4. UDP Throughput at 5 dBi Antennas Gain

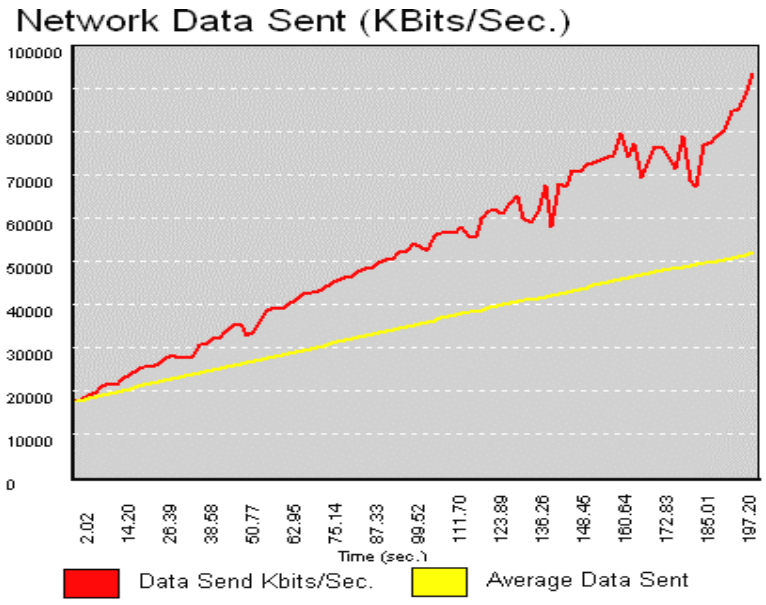

Figure 2. UDP Throughput (Port 161).

The values shown in Table 3 and 4 are average. The highest throughput measured with Performance Test 6.1 is 94 Mbps (fig. 2).

On Figure 3. is shown the percentage distribution of the transmitted frames between the transmitter and the receiver at different data rates. The distance between them is 52m. Most of the all frames - 14,4% are transmitted on 24,0Mbps.But it is important to mark that 20,82% of all data is transmitted on data rates 127.0÷263.7 Mbps. – 802.11 n.

On the application layer of the TCP/IP model, is realised file transfer (on FTP) of 6,58 GB (7070469411 bytes). The transferred data contains different by size and type files (mpeq, avi, mp3, cda, doc, html pages, jpeg, ets.).The distance is 20 m between the transmitter and the receiver and the radio signal is transmitted through one brick-built wall.

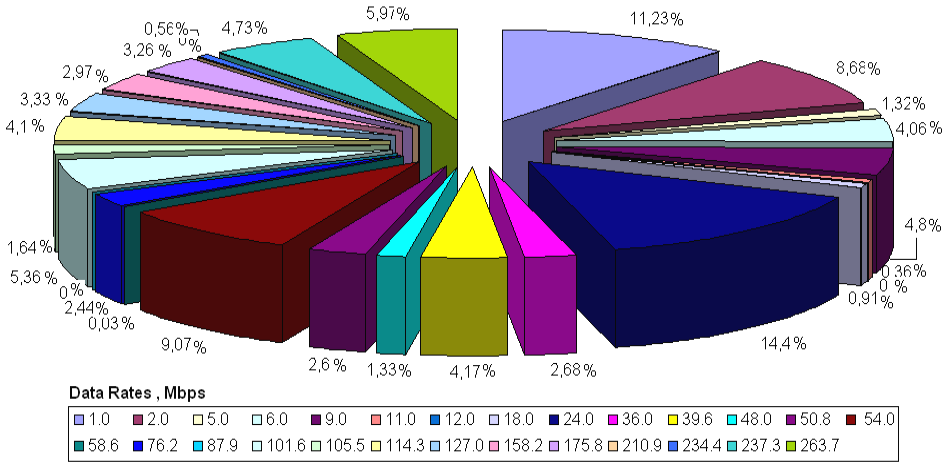

Figure 3. Percentage distribution of transmitted data

Figure 4. FTP Downlink

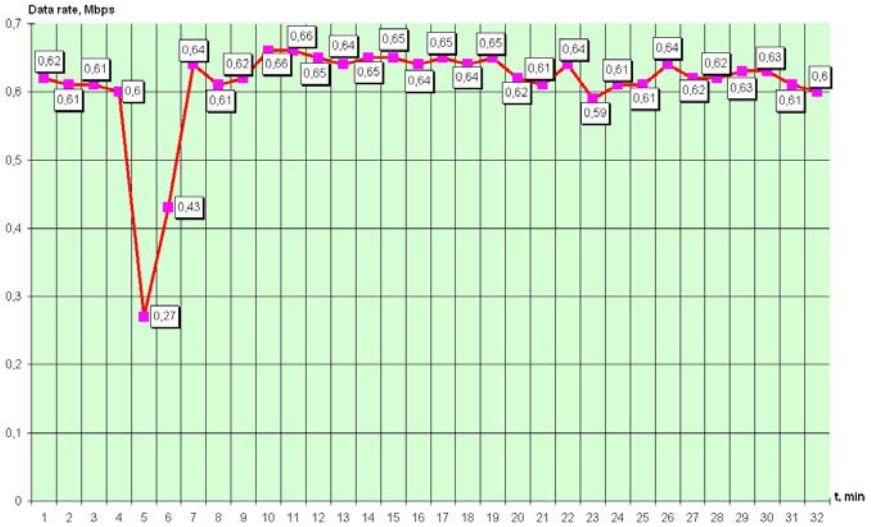

Figure 5. FTP Uplink

The average downlink and uplink data rate of the file transfer are 29,22 Mbps and 0,61 Mbps. The total time of transfer is 32.10 min. The utilization of the wireless network at the time of transfer was very low – 6.83%.There is no fluctuation in the data rate except one drop. FTP is often used from the users of the WLANs and this test shows real data rates between two nodes.

As can see from experimental results the throughput is not very high. Based on analysis of many proposals [1-8] for 802.11n enhancements we can conclude to break the 100 Mbps throughput barrier:

– Frame aggregation must be added to the 802.11n MAC as the key method of increasing efficiency. The issue is that as the data rate increases, the time on air of the data portion of the packet decreases. However, the PHY and MAC overhead remain constant. This results in diminishing returns from the increase in PHY data rate. Frame aggregation increases the length of the data portion of the packet to increase overall efficiency;

– Using of the reverse direction protocol, which allows a station to share its transmit opportunity (TXOP) with another station. This increases throughput with traffic patterns that are highly asymmetric, for example, when transferring a large file with FTP operating over TCP. Time is borrowed during the TXOP to send the short TCP Acknowledgment in the reserve direction. Depending on the usage model, TCP traffic throughput may improve up to 40 percent [1];

– Using of the greenfield format- By eliminating the components of the preamble that support backward compatibility, the greenfield format preamble is shorter than the mixed format preamble. This difference in efficiency becomes more pronounced when the packet length is short, as in the case of VoIP traffic.

4. CONCLUSION

This paper presents some experimental results and analyze of throughput of 802.11n network. The achievable throughput in test is fine for many applications, interconnection devices with higher data rates, particularly HDTV and streaming video and audio in short indoor distance not more then 50 m. The MIMO technology and multiple antennas extends the network coverage and is one of the main factors of higher throughput. The 802.11 n network devices are full compatible of 802.11 a/b/g devices and it is possible to work in a mixed mode.

References

[1] E. Perahia and R. Stacey, Next Generation Wireless LANs: Throughput, Robustness, and Reliability in 802.11n, Cambridge Univ. Press, 2008

[2] Lee J.H., Beak M.S., Song H.K., Efficient MIMO Receiving Technique in IEEE 802.11 N System for Enhanced Services, IEEE Transactions on Consumer Electronics, Vol.53, No 2 , MAY 2007

[3] Nanda S., Walton R., Ketchen J., Wallace M., Howard S., A High-Performance MIMO OFDM Wireless LAN, IEEE Communication Magazine, February 2005

[4] Sarris I., Doufexi A., Nix A.R., High-Performance WLAN Architectures Using MIMO Technology in Line-of-Sight, CNF-IST Mobile Summit, Jun 2006

[5] Cisco Systems, 802.11n Wireless Technology Overview, White Paper, August 2007

[6] Panagiev, O. B. Performance comparison of OFDM and 8-VSB transmission systems for terrestrial digital television broadcasting. Info Tech'2007, Proc. of Papers, vol.2,Varna, 21-22 Sept. 2007, pp. 133-138

[7] Litwin L.,Pugel M. The principles of OFDM, January 2001

[8] http://en.wikipedia.org/wiki/802.11#802.11n

[9] www.d-link.biz

[10] www.airmagnet.com

[11] www.passmark.com

[12] www.80211n-bg.com

HALL SENSOR FOR THE STEPPING CONTACT FORCE

Dimitar Diakov, Mladen Milushev, Vania Georgieva

Technical University – Sofia, Bulgaria
St. Kliment Ohridski, 8
Tel.: +359 965 3428; E-mail: milushev@tu-sofia.bg

Abstract

Walking robots are meant for application on rough, unstructured surfaces. Their adaptation to different terrains is achievable through securing a high adhesion capacity. This paper shows the process of designing a sensor capable of integration into the robot's leg. In this paper, we consider.

1. INTRODUCTION

A walking robot's control entails a continuous flow of tangible information about the complete system's status. Basic sources are the joint's angles, the contact with surfaces reached through adhesion forces and moments and the body's orientation [1], [2]. Sensor signals from audio and video sensors [4] and also each leg's pressure on the floor have different scopes and require independent interpretation [5]. The need comes from the different possible supporting-phase-combinations in the case of six, four, three etc. legs [3]. Depending on the given support phase the body's mass is cast upon the legs with different adhesion force values.

The accessible sensor types, which have been studied and analyzed do not meet the specific requirements for the basic gear of a six-legged walking robot (Aschenbeck et al, 2006) and (Weidemann et al, 2004) driven by artificial pneumatic muscles (Kepplin et al, 1999) [6]. Hence, the paper suggests a force sensor based on magnetic-sensitive reducer.

2. PRINCIPLE OF THE SENSOR

The sensor embedded within the leg's construction is shown in Fig. 1. The principal element is the flat spring, which allows displacement between magnet 2 with respect to the Hall's sensor 3. Depending on the friction force the distance between the magnet and the Hall's sensor is not constant.

The pressure varies from 4 to 10 kg depending on the number of the supporting legs. The design parameters are chosen in such way that, for example, 10 kg pressure corresponds to 0.5 mm, while 4 kg pressure corresponds to 1,6 mm.

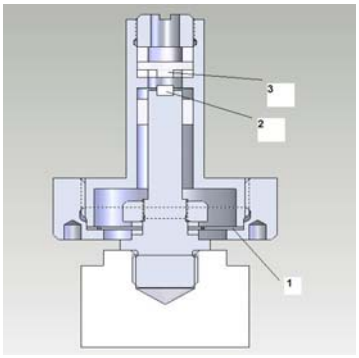

Fig. 1 Construction of the foot force sensor.

3. EXPERIMENTAL WORK

To determine the optimal parameters of the sensor, the transfer characteristic was investigated for a 5, 7 and a 9V supply, and a step of 0.1mm. The measured values of the sensor output voltage are shown in Fig. 2. It is evident that in the interval from 0.5mm to 1.6mm, the sensitivity corresponding to 5V and obtained by (1) can be considered as being satisfactory linear. The measured average square value of the noise voltage equals σ_u e 2 mV. This interval excludes nonlinearities of the characteristics,

which is also valid for the two terminal positions of spring where nonlinear changes are also to be expected:

$$\delta = \frac{\Delta Dist}{\Delta Uout} \qquad (1)$$

The higher sensitivity (Fig. 3) obtained for smaller loads is an advantage, which can be used for different gaits and curvilinear motion of the robot.

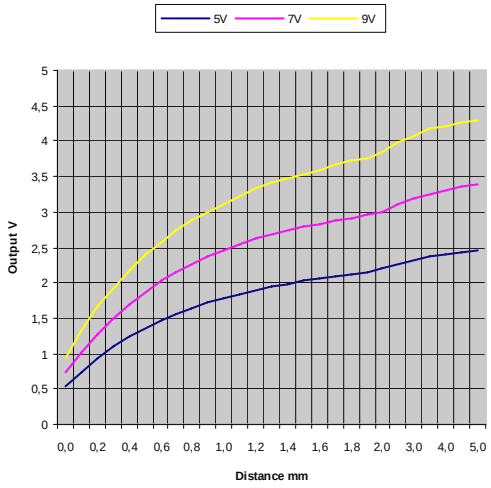

Fig. 2. Measured value of the sensor output voltage

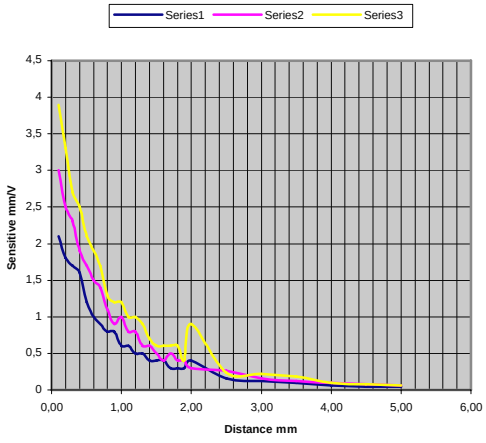

Fig. 3. The sensor sensitivity

4. RESULTS OF THE MODELLING AND DISCUSSION

The suggested sensor variant for integrating the leg into the robot is shown in Fig. 1. It has been developed under implementation of SolidWorks. The whole setting is aimed at simulating the loads, which are to be expected in the final construction variant. The entire unit has been computed using the software program „CosmosWorks". A basic element of the sensor, i. e. initial transducer, is the spring (Fig. 4). The material used to simulate the spring is steel 60C2 with diverse physical features presented in Table 1.The load and displacement simulation was made first for the spring alone and upon that – for the whole unit. The spring was wedged and loaded with a force varying from 5 N to 100 N along the Y- axis (Fig. 3). The spring's stroke was measured (along the Y-axis). The dependence characteristic is linear.

Property	Description	Value	Units	Temp Dependency
EX	Elastic modulus	2.100000005e+011	N/m^2	Constant
NUXY	Poisson's ratio	0.28	NA	Constant
GXY	Shear modulus	7.899999806e+010	N/m^2	Constant
DENS	Mass density	7700.000118	kg/m^3	Constant
SIGXT	Tensile strength	1400000000	N/m^2	Constant
SIGXC	Compressive strength		N/m^2	Constant
SIGYLD	Yield strength	1200000000	N/m^2	Constant
ALPX	Thermal expansion co	1.3e-005	/Kelvin	Constant
KX	Thermal conductivity	50	W/(m.K)	Constant
C	Specific heat	460	J/(kg.K)	Constant

Table 1. Characteristics of the applied steel

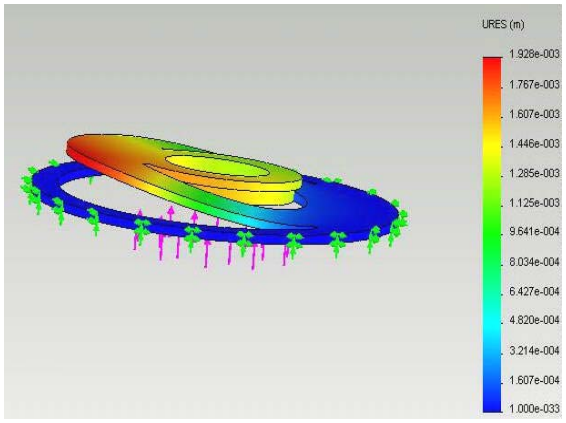

Fig. 4. Simulation displacement graphics

Fig. 5 visualizes the displacement result for the unit as a whole. In this case the system carries once again the maximum load of 100N. The obtained displacement values along the Y axis are shown on diagram Fig.6. As a function of the load the displacement is strictly linear for the entire given scope.

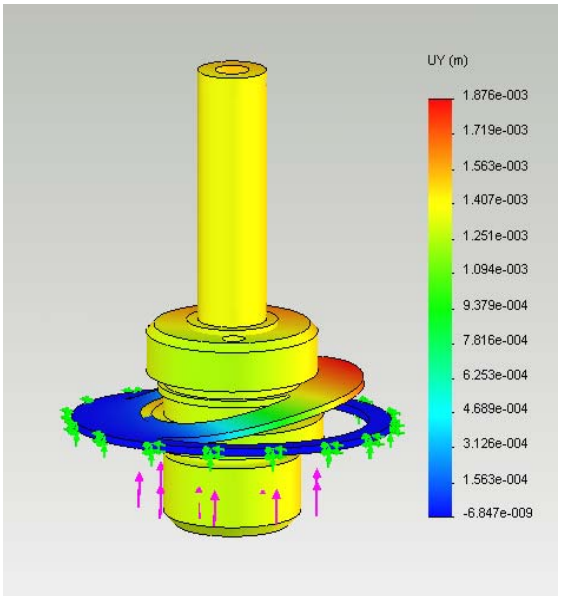

Fig. 5. Simulation displacement graphics

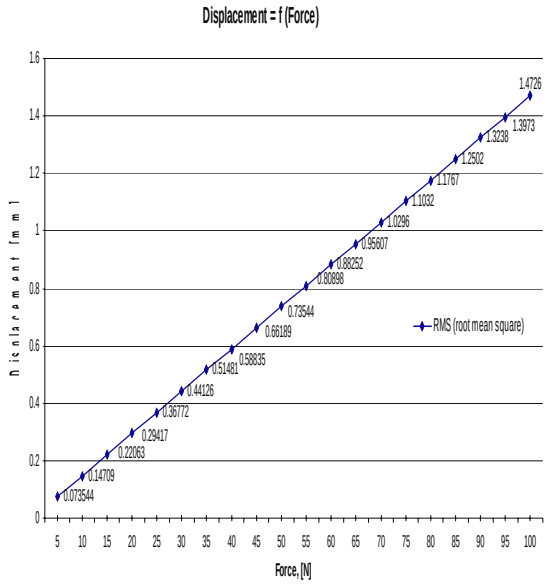

Fig. 6. Displacement of the spring as a function of the load

5. CONCLUSION

The resulting linear characteristics for both the spring and the Hall's element are premises for realization of a linear feature for the sensor as a whole.

Because of the bigger scope of the Hall's element the linearity of displacements in the range 0,5мм - 4,5мм the combining of springs with various scopes gets possible.

Following the obtained parameters the dynamic behavior of the whole sensor could be practically achieved as well as experimentally tested.

The suggested sensor type sets an alternative to the often applied for similar cases potential metric and tens metric ones.

ACKNOWLEDGEMENT

This work was supported by National Ministry of Science and Education of Bulgaria under Contract BY-I-302/2007: "Audio-video information and communication system for active surveillance cooperating with a Mobile Security Robot".

References

[1] Aschenbeck, K.S., N.I. Kern, R.J. Bachmann, and R.D. Quinn (2006). "Design of a Quadruped Robot Driven by Air Muscles," *IEEE/RAS-EMBS Int. Conference on Biomedical Robotics and Biomechatronics (BioRob'06)* Proceedings, Pisa, Italy, February 20-22, 2006.

[2] Weidemann, H.-J.; Pfeiffer, F. & Eltze, J. (2004) The six-legged TUM walking robot. *Intelligent Robots and Systems (IROS*), Volume 2, 2004, p.p. 1026-1033.

[3] Milushev M., Petrov P., Kostadinov K., Zerbe V. (2007). Mechanical Hardware and Kinematic Model of a Six-Legged Robot Driven by Fluidic Muscles*. 8th Magdeburg days of mecanical engineering & 7th MAHREG innovations forum,* Magdeburg, 10-11 October, 2007, pp.118-125, ISBN 978-3-929757-12.

[4] Bekiarski A., Sn.Pleshkova, Speech Localization and Video Control for Audio and Visual Robot Systems, International Scientific Conference Computer Science, Kavala, Greece, 2008

[5] Gonzalez de Santos P., Garcia E., Estremera J. and Armada A.(2000), SILO06: Design and configuration of a legged robot for humanitarian demining, *Int. Workshop on Robots for Humanitarian* Demining, 2002

[6] Kepplin V., Berns K. (1999) Clawar 99: A concept for walking behavior in rough terrain. *In Climbing and Walking Robots and the Support Technologies for Mobile Machines*, pp. 509-516

MOVEMENT OF CHARGED PARTICLE IN ALIVE TISSUES UNDER EXTERNAL ELECTRICAL FIELD

Nikola Dimitrov Ralev

Technical University of Sofia,Bulgaria,Tel.+359 887 306 947;
E-mail nikola.ralev@gmail.com.

Abstract

This article treats the motion of charged particles, mainly electrons or protons, composed of a uniform axial component, in an external electric field. These equations can be the basis of computer programs to calculate particle trajectories in the general case, a valuable resource, but such calculations do not give a general understanding of particle motion. This article is intended to foster such an understanding as an aid to reasoning about natural phenomena.

INTRODUCTION

In this article certain aspects are considered of the motion in a vacuum of a point charge under the influence of on electric field.

MAIN TEXT

The classical motion of the particle in such a field is determined by Newton's equation of motion, where the force is given by:

$$a = \frac{F}{m} = \frac{q}{m}(E + vXB) \qquad (1)$$

The problem that presents itself is that of solving the equations of motion given in relativistic from

$$\frac{d}{dt}\left\{\frac{m_o v}{\sqrt{(1-v^2/c^2}}\right\} = e(E + vXB) \quad (2)$$

The problem becomes, in principle, straightforward if it be assumed that E,B appearing in the right-hand side of (2) is a given field; the difficulties are then of the purely technical kind that can also arise in traditional particle mechanics with mechanical forces. The assumption is often a legitimate approximation, and most of the work presented here is in this context. In fact, however, the charge itself also contributes to the electromagnetic field, and its contribution depends on its motion. The inclusion of this "self-force" presents quite fundamental difficulties because of the infinities associated with the concept of a point charge. Attempts to describe the motion of an electron can perhaps be classified in terms of the following alternatives: (I) abandon the idea that the electron is a point charge, and give it some internal structure; (II) introduce into the classical mathematical framework some formalism that succeeds in discarding the infinities. The (II) has led to an equation of motion which at least in certain contexts is acceptable theoretically an is in general agreement with practice.

In attempting to solve (1) it may be helpful to make use of the associated energy equation

$$\frac{d}{dt}\left\{\frac{m_o c^2}{\sqrt{(1-v^2/c^2}}\right\} = e(E.v) \qquad (3)$$

If the electric field is purely static, so that E =- grad φ, this gives

$$\frac{m_o c^2}{\sqrt{(1-v^2/c^2}} + e\phi = const \qquad (4)$$

If we have an uniform electrostatic field (E,0,0), If the motion is confined to the x-axis the equation of motion integrates at once to

$$\frac{m_o v}{\sqrt{(1-v^2/c^2}} = eEt \qquad (5)$$

with appropriate choice of time zero. The equation can easily be solved for v in terms of t and integrated again. But it is even quicker to use also the energy equation (4), which here is

$$\frac{m_o c^2}{\sqrt{(1-v^2/c^2}} = eEx \qquad (6)$$

with appropriate choice of origin. For the elimination of v between (5) and (6) gives immediately

$$x = c\sqrt{\left(\frac{m_0{}^2 c^2}{e^2 E^2} + t^2\right)} \qquad (7)$$

In the motion specified by (7) the speed tends to the limit c as t->±∞. As t comes up zero the particle moves toward the origin along the positive x –axis with a deceleration which brings it to rest at t=0; it then accelerates back on the return journey with a speed that approaches c asymptotically. The motion is, in fact, that sometimes called *hyperbolic,* in which the space part of the relativistic four-acceleration is constant.

The general motion in the electrostatic field (E,0,0) can be found in the such same way. Choose the x-axis in the direction of the electric field, and the y-axis so that the xy-plane contains both the electric field and the initial velocity. Since the acceleration normal to this plane is zero, and the initial velocity normal to it is zero, the motion remains in this plane, say z=0. Then, with appropriate choice of time zero, the x- and y-components of the equation of motion integrate to

$$\frac{m_o x}{\sqrt{(1-v^2/c^2}} = eEt \qquad (8)$$

$$\frac{m_o y}{\sqrt{(1-v^2/c^2}} = p_0 \qquad (9)$$

where the constant p0 is the initial value of the relativistic momentum, and $v^2 = x^2 + y^2$. By squaring and adding

$$\frac{m^2{}_o v^2}{1-v^2/c^2} = e^2 E^2 t^2 + p_0{}^2 \qquad (10)$$

and the elimination of v^2 between (10) and the energy equation (6) gives

$$x = c\sqrt{\left(\frac{p^2 + m_0{}^2 c^2}{e^2 E^2} + t^2\right)} \qquad (11)$$

Also from (9) an (6)

$$y = \frac{c^2 p_0}{eE} x$$

And substitution for x from (11) followed by integration results in

$$y = \frac{cp_0}{eE} \sinh^{-1}\left\{\frac{eEt}{\sqrt{(p_0{}^2 + m_0{}^2 c^2)}}\right\} \qquad (12)$$

The equation of the path is obtained by elimination t between (11) and (12). It can be written

$$x = \frac{c\sqrt{(p_0{}^2 + m_0{}^2 c^2)}}{eE} \cosh\left(\frac{eEy}{cp_0}\right) \qquad (13)$$

The solution of this equation, subject appropriate initial conditions, give the path of particle resulting from action of the electric forces. It should be remarked that the motion (11) and (12) is not hyperbolic. General hyperbolic motion, an a plane rather than along a line, could be derived from (7) by a Lorenz transformation; and such motion would be that particle was acted on by the field twat was the transformation of (E,0,0), a filed which would, in fact, be partly magnetic.

CONCLUSION

A solution is proposed of tracing the path of a charged particle resulting from action of the electric forces.

References

[1] T. G. Northrop, The Adiabatic Motion of Charged Particles (Intense Tracts on Physics and Astronomy, No. 21), Interscience 1963.

[2] J. D. Jackson, Classical Electrodynamics, Wiley (1962)

[3] S. E. Koonin, *Computational Physics,* Addison-Wesley, Redwood City, 1986.

[4] D. J. Griffiths, *IntToduction to Electro-Dynamics,* Prentice Hall of India, 1999.

TRANSCUTANEOUS ELECTRICAL STIMULATION

Nikola Dimitrov Ralev

Technical University of Sofia,Bulgaria,Tel.+359 887 306 947;
E-mail nikola.ralev@gmail.com.

Abstract

Transcutaneous electrical stimulation as one of several ways to provide relief for patients with chronic neuropathic or neuromuscular pain. It will be sufficient as the only therapy for some and a useful adjunct for pain relief in many others. The key to successfuluse is an appropriate diagnosis. Pain is a common complaint that is frequently modified by ecological. Behavioral and socioeconomic factors. It is unlikely that trans-ptaneous stimulation or any other form of pain relief will affect these aspects of the pain sindrome. Pain is a common complaint that is frequently modified by ecological. Behavioral and socioeconomic factors. It is unlikely that trans-ptaneous stimulation or any other form of pain relief will affect these aspects of the pain sindrome.

INTRODUCTION

There have been several studies which demonstrate increase in pain threshold to experimental induced pain following transcutaneous electrical stimulation. Why these changes in pain threshold occur is less clear. There is additional information that determines that changes in parameters of stimulation can modify the effects. Much more has been done with parameter change with internal stimulators than with transcutaneous stimulation. The original stimulators provided a range of 60-100 Hz. Short bursts appear to be as effective as prolonged stimulation and square waves are usually employed. However, many different wave forms have been tested and seem to be effective. Effects are not parameter specific.

There is also controversy about whether the effects of TENS are reversible by naloxone. In our own work, we were unable to determine any effect of naloxone. Other investigators have shown that low-frequency stimulation pain relief is reversible by naloxone

MAIN TEXT

Transcutaneous electrical stimulation was originally based upon the general concept enunciated by Melzak and Wall in their gate-control theory. The hypothesis was that the stimulation of peripheral receptors would block or modify pain transmission from nociceptors probably at the spinal cord level and thus reduce pain. Several variations of this theme have been presented. It has been suggested that the block may be local at the receptor level or involve peripheral nerves. The stimulation may activate an inhibitory system at the level of the dorsal horn, or it may activate a descending inhibitory tract originating principally from thalamus and brainstem.

A placebo response have also been invoked. There are enough controlled studies that compare TENS with sham simulation, subliminal stimulation, and other kinds of sham therapies to demonstrate that the effect of stimulation is beyond what can be explained by placebo.

While very little direct research has been done on the possible effects of TENS, there is much material from pain in literature that provides additional information about possible bodes of action. There are accepted causes of pain, which include acute tissue injury, peripheral nerve injury, peripheral nerve compression, or spinal instability. All activate nociceptors. There are theoretical causes of pain for which there is strong experimental evidence. Nociceptors may be activated by chemical agents, such as might be derived from a degenerated disk. Nociceptors sensitization after injury is a well-accepted event, and associated mechanosensi-

tivity, such as occurs in types 2 and 3 neurons, has also been demonstrated. There is definite evidence that sensitization of a c-fiber nociceptors, which is usually confined at the site of the injury, is a first event in pain perception. Central sensitization of A nociceptors, which occurs in the site of injury and the surround, is also known to occur and sensitization of AB non-nociceptors, which produces allodynia, has also been demonstrated. The possibility that electrical stimulation modifies the sensitization

Process either through its local effects or at the level of the dorsal horn is a reasonable supposition. An experimental model that is used to investigate peripheral nerve injury also indicates that much of the perceived pain is mediated through adjacent uninjured nerves. A blocking effect preventing this spread of the pain signal is certainly possible.

Central facilitation of the reduction of pain threshold is known to occur. This central facilitation is reduced by pain-relieving procedures, and this is another possible explanation of the effects of electrical stimulation of the nervous system. The central inhibition may also be an important phenomenon. The central inhibition is impaired when pain is continuous and reappears when pain is controlled. Increasing the effectiveness of central inhibition is another possible explanation.

CONCLUSION

The use of electrical stimulation for pain control has a long history over the last 40 years or more. In the early 1970s, well-engineered controllable devices were developed and since that time, many well-controlled studies have indicated the value of the technique. There are many applications for which stimulation is a reasonable alternative to other symptomatic methods of pain control. Many other poorly designed and critical reports are in the literature describing transcutaneous electrical stimulation which fast been inexpertly applied to patients. When an appropriate diagnosis has been made and fe patient educated in the use of the technique, it remains a valuable adjunct in pain management that will provide satisfactory relief to many.

References

[1] Augustinsson L-E, Bohlin P, Bundscn P, Carlsson CA, Forssman I. Pain relief during delivery by transcutaneous electrical nerve stimulation. Pain 1977

[2] Callaghan M. Siernback R A, Nyquist JK, Timmermans G. Changes in somatic sensitivity during transcutaneous electrical analgesia. Pain 1978

[3] Campbell JN, Taub A. Local analgesia from percutaneous electrical stimulation: A peripheral mechanism. Arch Neurol 1973

SOME RESULTS ON CLINICAL APPLICATION OF LOW FREQUENCY MAGNETIC FIELD CREATED BY APPARATUS FOR MAGNETOTHERAPY

Hristo Damianov, Matei Gavrilov, Borislav Tonev

Medical University of Sofia, G. Sofiisky str. 30, 1000 Sofia,Bulgaria

Abstract

The experimental and clinical data demonstrate that exogenous magnetic field (MF) and electromagnetic field (EMF) of surprisingly low amplitudes can have a profound effect in healing of a wide variety of pain, injuries, and pathologies. Perhaps the greatest challenge for what it may term electromagnetic biology and medicine is to establish the proper dosimetry for modulation of the desired biochemical cascade.

The final results of magneto-therapy depends to the space-temporal configuration of applied magnetic field. Therefore the basic requirements in the process of design of apparatus for magneto-therapy is connected with optimization of parameters of applied low frequency magnetic field.

1. INTRODUCTION

Usually the low frequency magnetic field in physiotherapy is provided by apparatus for magneto-therapy. This apparatus can provide low frequency magnetic pulses with different parameters.

There is a large body of experimental and clinical data that suggest that various exogenous low frequency magnetic field (MF) at surprisingly low levels can affect a large variety of tissues and processes, most of which are of critical importance for diagnostics and therapy. The longest clinical applications of magnetic fields are related to bone unification and the reduction of pain and edema in soft tissues.

During the past 25 years more than 2 million patients have been treated worldwide for a large variety of injuries, pathologies and diseases. This large number of patients exhibited a success rate of approximately 80%, with virtually no reported complications .

Low-frequency sine waves and low-frequency pulsed electromagnetic fields were used for treatment of pain associated with rotator cuff tendinitis, multiple sclerosis, carpal tunnel syndrome, and periathritis. With the exception of pcriathritis, which reported no difference between treatment and control groups, all other targeted sources of pain received a reduction in visual analog scale (VAS) pain scores. More importantly, the improvement was observed in 93% of patents suffering carpal tunnel pain, and 83% in rotator cuff tendinitis. It was also reported that 65% of the patient who received daily treatment over 8 weeks for rotator cuff tendinitis were pain free at the end of the study, as well as 70% of the multiple sclerosis patients who received 15 treatments with low-frequency sine wave MF reported a reduction in spasticity, improvement of bladder control, and improvement in endurance.

A number of clinical studies, in vivo animal experiments and in vitro cellular and membrane research suggest that magnetic and electromagnetic field stimulation may accelerate the healing processes .It is now clear that endogenous electromagnetic and magnetic interactions are associated with many basic physiological processes ranging from ion binding and molecular conformation in the cell membrane to macroscopic 'terations in tissues. The investigations of the mechanisms of action of MF on biological ystems that are in a state different than their normal physiological one represent the next ontier in electromagnetic biology and medicine. Space does not permit more than a superficial presentation of evidence here to support the statement that "different MF reduces different effects in different biotargets under differing conditions of exposure."

Basic science studies suggest that nearly all participants in the healing process (such as brinogen, leukocytes, fibrin, platelets, cytokines, growth factors, fibroblasts, collagen, lastin, kera-

tinocytes, osteoblasts, and free radicals) exhibit alterations in their functions as a results of exposure to MF. Magnetic fields were also shown to affect vasoconstriction and vasodilation, phagocytosis, cell proliferation, formation of the cellular network, epithelization, and scar formation. Alteration of the basic cellular activities that occur at any one of the distinct stages of tissue repair. The interactions of MF with any structure in the human organism could initiate biophysical and biochemical changes that in turn modify the physiological pathways *u:i* accelerate the healing process.

A question arises: how can this "heating" signal are applied for reduction of pain and edema. The answer is that the pulsed version of this signal (65-us pulse bursts, 100-600 pulses/s, peak magnetic field of 2G) allows the target tissue to be exposed to MF and to elicit a non thermal biological effect.

Therapeutic efficacy depends on the status of the patient (age, general health, and gender) as well as on the stage of pathology and/or disease. It has also been found that there is a distinct relationship between specific diseases and MF parameters that initiate optimal response for these particular pathologies.

2. TIME-VARYING MAGNETIC FIELD FOR PAIN CONTROL

Low-frequency sine waves and low-frequency pulsed magnetic fields were used for treatment of pain associated with rotator cuff tendinitis, multiple sclerosis, carpal tunnel 1 syndrome, and periathritis. For example, an improvement was observed in 93% of I patients suffering carpal tunnel pain and 83% in rotator cuff tendinitis. It was also reported that 65% of the patients who received daily treatment over 8 weeks for rotator cuff tendinitis were pain free at the end of the study, as well as 70% of the multiple sclerosis patients who received 15 treatments with low frequency sine wave MF reported a reduction in spasticity, improvement of bladder control, and improvement in endurance.

Pulsed radio frequency (PRF) modality was used for treatment of migraine, chronic pelvic pain, neck pain, and whiplash injuries. In parallel with improvement after the injury a reduction in the pain of 35% for patients having migraine, accompanied by a significant reduction in occurrence off headaches was reported.Pulsed signal therapy (PST) has been used for relief of pain and other ostheoai thrilis symptoms mainly. The system includes a bed, a circular coil of either 11 or 22 in. in diameter that delivers pulses of variable frequencies (in the range of 0,5-2 pulses/s), and magnetic fields of up to 2 mT. Several double-blind studies report a 88% decrease in pain from knee osteoarthritis after 18 sessions 30 min daily and the pain relief was present during the next month of follow-up.

3. PERMANENT MAGNETS FOR PAIN CONTROL

Since the middle of the 1990s, permanent magnets have become widely used for pain relief. Several recent studies report reduction of pain in postpolio patients (up to 76%). Fibromyalgia (up to 32%), peripheral neuropathy (up to 33%), and postsurgical Bunds (37-65%).

I these recent studies reported pain management for different etiologies and sites of pain. They demonstrate the potential of a static magnetic field to provide significant pain relief in different disorders. In a double-blind study it was shown that a static magnetic field of 300500 G significantly decreases the pain score in postpolio pain syndrome patients when compared with a placebo group. Another double-blind study demonstrated that sleeping on mattresses in which ceramic permanent magnets are embedded (with magnetic field at the target in the range 200-600 G) provided significant benefits to pain, fatigue, and sleep in patients suffering from fibromyalgia .The status of the patients in the real treatment group was improved by more than 30%. In a pilot study a significant improvement in 75% of patients with diabetic neuropathy who used permanent magnetic field stimulation on the soles of their feet was found.It appears that the proper choice of magnetic field strength, application site, duration, and frequency of application are of importance for the success of the therapy.

It should be noted that several studies failed to obtain any effects when so-called bipolar magnets were used. Reviewing the diverse ef-

fects reported recently, we conclude that the failure to find any effect is an obvious result of inaccurate dosimetry and poor planning of the studies.

4. MECHANISMS OF ACTION

The main reasons that MF and EMF are still not widely accepted as treatment modalities could be the absence of agreement about a common mechanism of action for EMF bioeffects and insufficient number of publications in medical journals. MF are recognized as capable of inducing selective changes in the microenvironment around and within the cell, as well as in the cell membrane which in turn may correct selected pathological states. However, the biophysical mechanism(s) of interaction of weak electric and magnetic fields with biological tissues as well as the biological transductive mechanism) remain to be elucidated. The analysis of reported specific reactions to MF and EMF indifferent biological systems suggests that most of the observed bioeffects strongly depend on the parameters of the applied electromagnetic fields.

To study the biophysical mechanisms of MF interactions one should begin with identification of the desired target to MF action. Then the nature of the initial physico-chemical interaction of EMF with biological systems and the expression of these phys-icochemical changes as a biological response should be investigated. The cell memhrane is most often considered the main target for EMF signals. Due to the fact that most of the cellular structures are electrically charged and that the biochemical reactions involve ion transfers, it is easy to assume that MF and EMF possess the potential to influence both the structure and function of the most important biochemical-biophysical processes. Starting from cell size and shape, going through the composition and architecture of the cellular membrane, one can also take into account the different sensitivity of cells based on the above described characteristics. Any change in the electrochemical microenvironment of the cell can cause modifications in the structure of its electrified surface regions by changing the concentration of a specifically bound ion or dipole, which may be accompanied by alterations in the conformation of moiecular entities (such as lipids, proteins, and enzymes) in the membrane structure. The role ofions as transducers of information in the regulation of cell structure and function is widely accepted. When cells are organized in a tissue, thel expected response should include cell-cell communications. In addition for in vivo experiments the complexity of the animal and human organism and theexislence of compensatory mechanisms that work on the organism level must be considered.

From a clinical point of view it is also difficult to believe that each of these mechanisms might be useful in explaining the beneficial effects of magnetotherapy, especially the significant and rapid pain relief observed in several different studies such as postpolio patients, diabetic neuropathy, postsurgical wounds, and fibromyalgia.

A series of studies of EMF influence on various biological systems demonstrated the appearance of windows effects. The windows represent combinations of amplitude and frequency within which the optimal response is observed; outside this range the response is significantly smaller. In other words, this demonstrates the principle "more does not necessarily mean better."

CONCLUSION

The correct choice of effective electromagnetic stimulation to accelerate healing requires measurement and computation of a variety of parameters, such as amplitude, field frequency and shape, duration of exposure, and site of application. Not only the precise characteristics of the applied or driving field and/or current but also the exact diagnosis and all other clinical data should be considered. Further research in the area of magnetic stimulation should clarify and optimize the choice of the appropriate magnetic field that are optimal for modulation of defined structures and processes that are involved in tissue healing and pain relief. A precise evaluation of electromagnetic field initiated bioeffects becomes increasingly important since the number of electromagnetic technologies and j devices used in clinical practice continues to grow.

References

[1] Abraham SE. Reynolds AC, Cusick JF. Failure to naloxonee to reverse analgesia from I transcutaneous electrical stimulation in patients with chronic pain. Anesth Analg 1981; 60:81-

[2] Anderson SA, Holmgren E. Pain threshold effects of peripheral conditioning stimulation. In Bonica JJ. Albe-Fesard DG, eds. Advances in Pain Research and Therapy. Proc. First World CongrPain. Vol 1. New York: Raven Press, 1976:761-768. :

[3] Arendt-Nielsen L, Bjerring P. Long-term effect of low and high frequency TNS on pain related cortical responses. Pain 1987; 4(suppl):S366.

[4] Augustinsson L-E, Bohlin P, Bundscn P, Carlsson CA, Forssman I. Pain relief during delivery by transcutaneous electrical nerve stimulation. Pain 1977; 4:59-65.

[5] Callaghan M. Siernback R A, Nyquist J. K, Timmermans G. Changes in somatic sensitivity during transcutaneous electrical analgesia. Pain 1978; 5:115-128.

ULTRASOUND MEDICAL IMAGES ENHANCEMENT ON THE BASE OF MORPHOLOGICAL PROCESSING

Veska M. Georgieva

Faculty of Telecommunication, Technical University of Sofia, Bulgaria
1000 Sofia, "Kl. Ohridsky" str.8
T. (+359 2) 965-3998; E-mail: vesg@tu-sofia.bg

Abstract

In the paper is presented an approach for ultrasound (US) medical images enhancement. The purpose is to demonstrate some techniques that enhance the appearance of US Images, including the nonlinear morphological filtering of single images to reduce noise and to solve complex problems with shape and contours of objects.

The post-processing of US images consists the following basic stages: changing the brightness of the image by equalization of the global histogram and contrast increasing by gamma correction of the obtained image. This increases the contrast of the small details in the investigated object. As next step is proposed selecting the region of interest (ROI) in the object and morphological processing of the selected ROI. The aim of algorithms, based on morphological operators, is noise suppression and detail preservation abilities of the selected ROI of US image. Some results of the experiments are presented, which are made by computer simulation in MATLAB environment.

1. INTRODUCTION

Due to its non-invasive nature and easily portable devices, ultrasound imaging is nowadays used for the diagnostic and clinical studies of many diseases. The quality of US images is very important by detection of some pathological modifications in a body structures and tissues.

The paper presents an approach for post processing of US image with the aim to improve its quality. For this is performed contrast preprocessing and detail preservation. The problem is solved changing the brightness of the image by equalization of its global histogram, following by gamma correction. For make best diagnosis is possible to select a region of interest of the object and detail preservation abilities on the base of morphological processing of the selected ROI [1], [2]. By properly choosing of dilatation, motion blur filtration and top & bottom hat filtration and suitable form of structuring element, local structures can be eliminated or local geometry of the investigated object can be modified. In the paper are analyzed some quantitative estimation parameters: Coefficient of noise reduction (CNR), Signal to noise ratio in the noised image (SNR_Y), Signal to noise ratio in the filtered image (SNR_F), Effectiveness of filtration (E_{FF}), Peak signal to noise ratio (PSNR) [3].

2. BASIC STAGES FOR US IMAGES ENHANCEMENT

The proposed image enhancement techniques are applied to real digital US images of the heart and abdominal tissues. US images processing consists of three basic stages, used to improve the image quality.

The first stage is increasing the contrast. For that step is necessary to increase the brightness of the image by equalization of its global histogram. The original images are presented in RGB system. The US apparatus work in this system. It is proposed with this approach to make the processing in YUV system for more effectiveness. So the procedure can be applied to Y decomposed component of the image. In addition the contrast can be adjusted by gamma correction of the processed Y component [3]. These operations increase the contrast of the small details in the investigated object.

The second stage in the processing is to define a ROI from the image. It can be selected in

interactive procedure from the operator (physician). The result of ROI image is written in file format that can be used in next processing.

Stage three includes morphological filtering by mean of three different morphological operators: dilation, motion blur filtration and top & bottom hat filtration. The morphological operators are compared together and one of them is estimated as a most effective method [5]. The top & bottom hat method is a well-suited. It increased the contrast of the object by means of increasing the details in the dark regions and near by contours. The top & bottom hat filtering extracts the original image from the morphologically closed version of the image. For this operation is studying the influence of three different flat structuring elements: line, disk and diamond. On the base of some quantitative estimations as: coefficient of noise reduction (CNR) signal to noise ratio in the noised image (SNR_Y), signal to noise ratio in the filtered image (SNR_F), effectiveness of filtration (E_{FF}), peak signal to noise ratio (PSNR) is selected a well-suited structuring element for US images. This algorithm includes following steps:

- Reading the ROI image and displaying it;
- Creating a flat structuring element, needed for morphological processing;
- Adding the original selected image to the top-hat filtered image, and than subtracting the bottom hat filtered image;
- Displaying the visual result of filtration;
- Determination of the quantitative estimations;
- Estimating the well-suited structuring element by minimum value for CNR and maximum values for PSNR and E_{FF} ;
- Writing the processed image in file format for next processing or data base preservation.

3. EXPERIMENTAL RESULTS

The formulated stages of processing are realized by computer simulation in MATLAB 7.2 environment by using of IMAGE PROCESSING TOOLBOX. IN experiments are used 20 real US images different file format: jpeg, tiff and bmp, but all of them are converted into bmp.

The obtained average results from the simulation are presented in Table 1.

Table1. Simulations results

Morphological Operations	PSNR [dB]	CNR	SNR_Y [dB]	SNR_F [dB]	E_{FF} [dB]
Top & Bottom Hat	26,3918	0,3617	15,5875	16,7779	1,1904
Dilatation	20,6402	0,8826	13,6167	14,3440	0,7273
Motion Blur	11,2418	0,1268	5,3170	6,2205	0,9035

The best results are obtained with the line structuring element in morphological processing. The values of PSNR and Effectiveness of filtration (E_{FF}) are maximum by use of top & bottom hat morphological operation. The value of CNR is 0.3 and shows that the noise is three times reduced. The graphical presentation of the PSNR-results for the three different morphological operations is shown in Figure 1. Figure 2 illustrates the diagram of E_{FF} and Figure 3 presents the diagram of CNR. On Figure 4 are illustrated the original (left) and brightness increased US image (right). Figure 5 presents original selected ROI of the image. In Figure 6, Figure 7 and Figure 8 are illustrated its morphological modifications by means of the three methods. It is shown the visible difference between the original and processed ROI, which is a result of the most effective morphological operation, applied to the image.

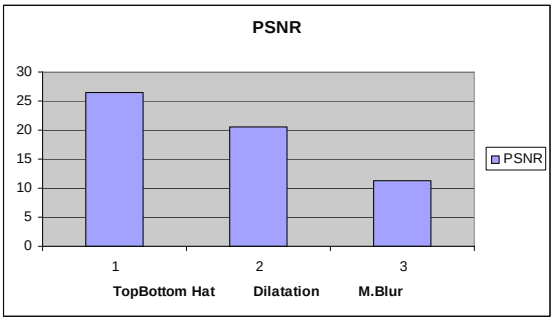

Figure 1. Diagram of PSNR in dB

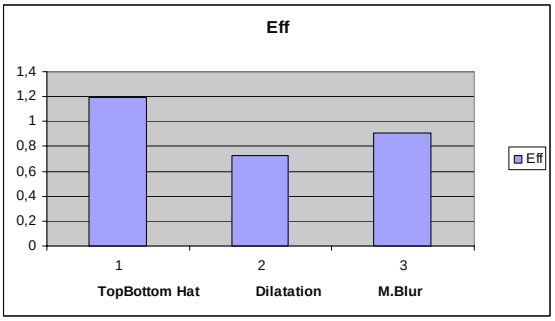

Figure 2. Diagram of E_{FF} in dB

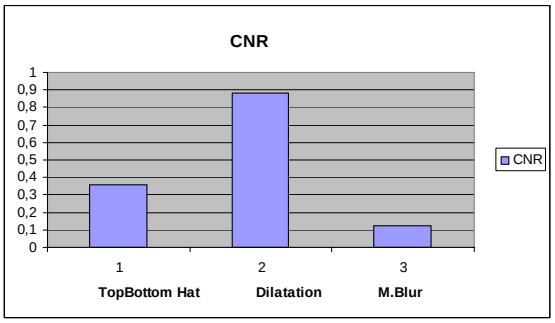

Figure 3. Diagram of CNR

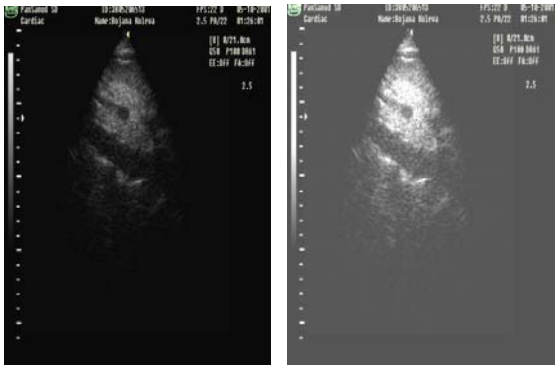

Figure 4. The original and the brightness increased US image

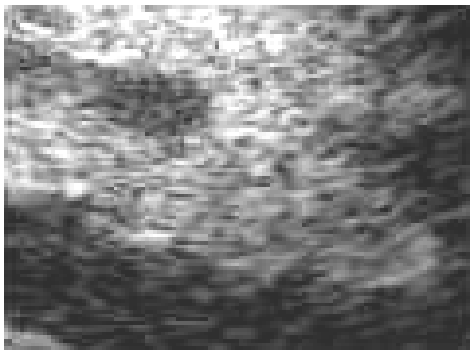

Figure 5. Selected ROI image

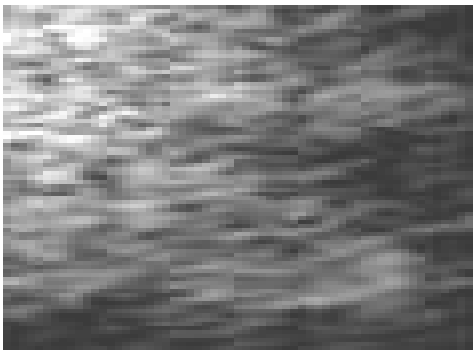

Figure 6. Processed ROI image by motion blur operation

Figure 7. Processed ROI image by dilatation

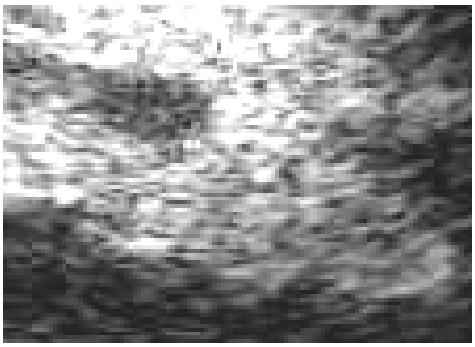

Figure 8. Processed ROI image by top & bottom hat operation

4. CONCLUSION

In the paper is proposed a new and effective approach for US image enhancement. The complex processing has an effect of brightness and contrast enhancement, and contours determination of objects for selected ROI of different parts of medical diagnostic US images. The implemented studying and obtained results by using of real images attempt to make diagnostic more obvious.

5. ACKNOWLEDGMENTS

I acknowledge to physicians from the Medical Center PanSanus, Sofia for providing of all ultrasound image data used in experiments and shown also in Figure 1.

References

[1] H. Kramer, J. Bruckner, "Iteration of nonlinear transformation for enhancement of digital images", Pattern Recognition, 7, 1997.

[2] M. Schulze, "Biomedical Image Processing with Morphology-based nonlinear Filter", PH.D. Dissertation, University of Texas, USA, 1994.

[3] R. Gonzalez, R. Woods, "Digital Image Processing", Addisson Wesly Publishing, 1992.

[4] V. Georgieva, "An Application of Wavelet Transforms for Ultrasound Images Enhancement", Journal of Electrical Engineering and electronics, Vol. 42, №3-4, Bulgaria, 2007, pp.78-83

[5] V. Georgieva, A. Genova "MRI Enhancement on the base of Morphological Processing", Proceedings of International Scientific Conference on Information, Communication and Energy Systems and Technologies, Vol.2, Nish, Serbia, 2008, pp. 558-561.

MOVEMENT OF IONS IN ALIVE TISSUES UNDER UNIFORM MAGFNETIC FIELD OF APPARATUS FOR MAGNETOTHERAPY AND UNIFORM ELECTRICAL FIELDS

Boncho A. Bonchev

Technical University of Sofia, Kl. Ohridsky str.8, 1000 Sofia

Abstract

Usually in physiotherapy application of magnetic or electrical field is the main reason for movement of ions in alive tissues. The trajectories of movement of ions depend to the space-temporal configuration of electromagnetic field. Therefore the first step in the process of investigation of movement of ions should be determination of space-temporal configuration of electromagnetic field. This is one complicated mathematical task, but it can be solved more easy in the case of uniform electrical and magnetic field. This method can be used for mathematical description of space-temporal configuration of electromagnetic field for one enough small volume as part of alive tissues.

1. MOVEMENTS OF IONS IN UNIFORM MAGNETIC FIELD

$$\vec{E} = 0 \ \wedge \vec{B}(x,y,z) = const \qquad (1)$$

Because of that, a charged particle has a simple cyclotron gyration. The equation of motion is:

$$m\frac{dv}{dt} = qv \times B \qquad (2)$$

Where:

m is the masse of charged particle;

v is the velocity charged particle;

q is the electrical charge of particle;

$\vec{B}$ is the magnetic induction in the point were is situated the charged particle;

Taking $\hat{z}$ to be the direction of B (B=B $\hat{z}$):

$$m\dot{v}_x = qBv_y \ ; \ \ m\dot{v}_y = -qBv_x$$
$$m\dot{v}_z = 0$$

$$\ddot{v}_x = \frac{qB}{m}\dot{v}_y = -\left(\frac{qB}{m}\right)^2 v_x \qquad (3)$$
$$\ddot{v}_y = \frac{qB}{m}\dot{v}_x = -\left(\frac{qB}{m}\right)^2 v_y$$

This describes a simple harmonic oscillator at the cyclotron frequency ω_c.

Where:

$$\omega_c \equiv \frac{|q|B}{m} \qquad (4)$$

By the convention ω_c can be always non-negative. Then the solution of equations (3) is:

$$v_{x,y} = v_\perp \exp\left(\pm i\omega_c t + i\delta_{x,y}\right) \qquad (5)$$

the $\pm$ denoting the sign of electrical charge q.The phase δ can be choose, so that:

$$v_x = v_\perp e^{i\omega_c t} = \dot{x} \qquad (6)$$

Where:

$v_\perp$ is a positive constant denoting the speed in the plane perpendicular to the vector of magnetic induction $\vec{B}$.

Then:

$$v_y = \frac{m}{qB}\dot{v}_x = \pm\frac{1}{\omega_c}\dot{v}_x = \pm i v_\perp e^{i\omega_c t} = \dot{y} \qquad (7)$$

After integration of equation (6) can be obtained:

$$x - x_0 = -i\frac{v_\perp}{\omega_c}e^{i\omega_c t} \qquad (8)$$

$$y - y_0 = \pm \frac{v_\perp}{\omega_c} e^{i\omega_c t}$$

The radius of rotation of charged particle (Larmor radius on fig.1) is:

$$r_L \equiv \frac{v_\perp}{\omega_c} = \frac{m v_\perp}{|q|B} \qquad (9)$$

Taking the real part of equation (7) can be obtained:

$$x - x_0 = r_L \sin \omega_c t$$
$$y - y_0 = \pm r_L \cos \omega_c t \qquad (10)$$

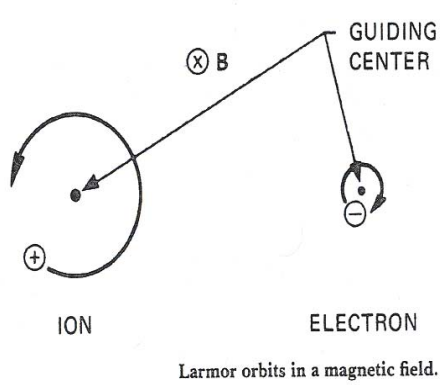

Larmor orbits in a magnetic field.

Fig. 1

It's clear that the equation (8) describes a circular orbit a guiding center (x_0,y_0) which is fixed (Fig.1).The direction of the gyration is always such that the magnetic field generated by the charged particle is opposite to the externally imposed field. The particles in alive tissue, therefore, tend to reuse the magnetic field, and alive tissues are diamagnetic. In addition to this motion, there is an arbitrary velocity v_z along the direction of the vector of magnetic induction B, which is not affected by B. The trajectory of charged particle in alive tissue is, in general, a helix.

2. MOVEMENTS OF IONS IN UNIFORM MAGNETIC FIELD AND UNIFORM ELECTRICAL FIELD

$$E(x,y,z) = const \wedge B(x,y,z) = const \qquad (11)$$

In this case, the motion of charged particle will be found to be the sum of two motions: the usual circular Larmor gyration plus a drift of the guiding center. The vector of intensity of electrical field E can be choose to lie in the x-z plane so that E_y=0. As before, the z component of velocity is unrelated to the transverse components and can be treated separately. The equation of motion of charged particle is:

$$m\frac{dv}{dt} = q(E + v \times B) \qquad (12)$$

Whose z component of the velocity is:

$$\frac{dv_z}{dt} = \frac{q}{m} E_z$$

or (13) $$v_z = \frac{qE_z}{m} t + v_{z0}$$

This is straightforward acceleration along magnetic induction B. The transverse components of equation (12) are:

$$\frac{dv_x}{dt} = \frac{q}{m} E_x \pm \omega_c v_y$$
$$\frac{dv_y}{dt} = 0 \mp \omega_c v_x \qquad (14)$$

If $E(x,y,z,t) = const$:

$$\ddot{v}_x = -\omega_c^2 v_x \qquad (15)$$

$$\ddot{v}_y = \mp\omega_c \left(\frac{q}{m} E_x \pm \omega_c v_y \right) = -\omega_c^2 \left(\frac{E_x}{B} + v_y \right)$$

It can be write as:

$$\frac{d^2}{dt^2}\left(v_y + \frac{E_x}{B} \right) = -\omega_c^2 \left(v_y + \frac{E_x}{B} \right) \qquad (16)$$

Therefore, that equations (15) is reduced to the previous case if replacement of, υ_y by $v_y + (E_x / B)$.

Equations (5) and (6) is therefore replaced by:

$$v_x = v_\perp e^{i\omega_c t}$$
$$v_y = \pm i v_\perp e^{i\omega_c t} - \frac{E_x}{B} \qquad (17)$$

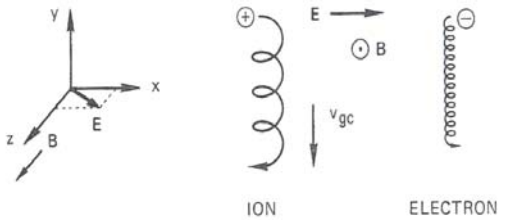

Fig.2. Particle drifts in crossed electric and magnetic fields

The Larmor motion is the same as in the case where $E = 0$, but there is superimposed a drift v_{gc} of the guiding center in the –y direction (for E_x>0), Fig.2

The equation (12) should be solved for obtaining a general formula for the velocity Vgc. The equation (12) can be solved in vector form. It's possible to omit the m dv/dt term in equation (12), since this term gives only the circular motion at wc., which we already know about. Then equation (12) becomes:

$$E + v \times B = 0 \qquad (16)$$

Taking the cross product with magnetic induction B:

$$E \times B = B \times (v \times B) = vB^2 - B(v.B) \qquad (17)$$

The transverse components of this equation are.

$$v_{\perp gc} = E \times B / B^2 \equiv v_E \qquad (18)$$

Where:

v_E is the electric field drift of the guiding center.

In magnitude, this drift is:

$$v_E = \frac{E(V/m)}{B(tesla)} = \left[\frac{m}{\sec}\right] \qquad (19)$$

It is important to note that velocity v_E is independent of electrical charge q, masse m, and velocity $v_\perp$. The reason is obvious from the following physical picture. In the first half cycle of the ion's orbit in Fig. (2), it gains energy from the electric field and increases in velocity $v_\perp$ and hence in radius r_L. In the second half-cycle it losses energy and decreases in radius r_L. This difference in r_L on the left and right sides of the orbit causes the drift with velocity v_E. A negative ion gyrates in the opposite direction but also gains energy in the opposite direction. For particles of the same velocity but different mass, the lighter one will have smaller radius r_L and hence drift less per cycle. However, its gyration frequency is also larger, and the two effects exactly cancel. Two particles of the same mass but different energy would have the same cyclotron frequency ω_c. The slower one will have smaller radius r_L and hence gain less energy from E in a half-cycle. However, for less energetic particles, the fractional change of radius r_L for a given change in energy is larger, and these two effects cancel.

CONCLUSION

1. A mathematical analysis of movement of ions in alive tissues under uniform electrical and magnetic field is described in the paper.
2. The trajectories of movement of ions have been obtained.
3. An analysis of connection between parameters of ion's trajectories and masse of ions, electrical charge of ions, magnetic induction and intensity of electrical field have been obtained.

References

[1] Sabin, M.A. (1985) Contouring - the State of the Art, in *Fundamental Algorithms for Computer Graphics*, R.A. Earnshaw (ed.), Springer Verlag, pp. 411-482

[2] Levoy, M. (1988) Display of Surfaces from Volume Data, *IEEE Computer Graphics and Applications* 8(3), pp. 29-37

[3] Lorensen, W.E., H.E. Cline (1987) Marching Cubes: a High Resolution 3D Surface Construction Algorithm, Proceedings Siggraph '87, *Computer Graphics* 21(4), pp. 163-169

[4] R.M. Kirby, H. Marmanis, and D. Laidlaw, Visualizing multivalues data from 2D incopressible flows using concepts from painting, In *Visualization 99*, pp. 333-340, October 1999.

[5] U. Adamy, J. Giesen, and M. John, New techniques for topolgically correct surface reconstruction, In *Visualization 2000*, pp. 373-380, October 2000.

[6] D.M. Weinstein, G.L. Kindlmann, and E.C. Lundberg, Tensorlines: Advection-diffusion based propagation through diffusion tensor fields, In *Visualization 99*, pp. 249-250, October 1999.

[7] H. Garcke, T. Preußer, M. Rumpf, A. Telea, U. Weikrad, and K. Van Wijk. A continuous clustering method for vector fields, In *Visualization 2000*, pp. 351-358, Oct 2000.

MOVEMENT OF IONS IN ALIVE TISSUES UNDER NONUNIFORM MAGFNETIC FIELDS CREATED BY APPARATUS FOR MAGNETOTHERAPY

Boncho A. Bonchev

Technical University of Sofia, Kl. Ohridsky str.8, 1000 Sofia

Abstract

It's well known that in the case of real application of electromagnetic field in physiotherapy, the electromagnetic field in alive tissues usually is non-uniformed. Therefore it's difficult to provide a precise mathematical descriptions, but it's possible to solve the problem in same cases as movement of ions under magnetic field with curved lines and invariant value of magnetic induction B (curvative drift) or movement of ions under magnetic field of magnetic mirrors. A theoretical investigations on movement of ions in alive tissues in these two cases is described in the paper

1. INTRODUCTION

Now the concept of a guiding center drift is firmly established. It's possible to discuss the motion of particles in inhomogeneous field – E and B fields, which vary in space or time. For uniform fields can be obtained exact expressions for the guiding center drifts. In the case of inhomogeneity, the problem becomes too complicated to solve exactly.

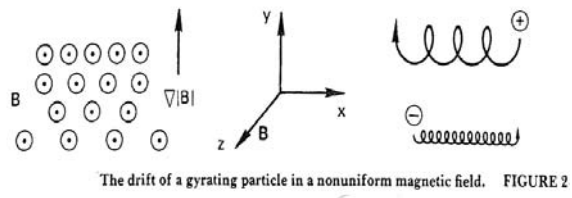

The drift of a gyrating particle in a nonuniform magnetic field. FIGURE 2

Fig. 1

To get an approximate answer, it is customary to expand in the small ratio r_L/L, where L is the scale length of the inhomogeneity. This type of theory, called orbit theory, can become extremely involved. It would be possible to examine only the simplest cases, where only one inhomogeneity occurs at a time $\nabla B \perp B$.

Here the lines of force are straight, but their density increases, say in the y direction (Fig. 1). It would be possible to anticipate the result by using our simple physical picture. The gradient in |B| causes the Larmor radius to be larger at the bottom of the orbit than at the top, and this should lead a drift , in opposite directions for ions and electrons, perpendicular to both B and ∇B. The drift velocity should obviously be proportional to r_L / L and to $v_\perp$. Consider of the Lorenz force $\mathrm{F} = \mathrm{qv} \times \mathrm{B}$ averaged over a gyration. Clearly, $\overline{F}_x = 0$, since the particle spends as much time moving up as down. It's possible to calculate $\overline{F}_y$, in an approximate fashion, by using the undisturbed orbit of the particle to find the average. IIn this case:

$$F_y = -qv_x B_z(y) = \\ = -qv_\perp(\cos\omega_c t)\left[B_0 \pm r_L(\cos\omega_c t)\frac{\partial B}{\partial y} \right] \quad (1)$$

It possible to made a Taylor expansion of B field about the point $x_0 = 0$, $y_0 = 0$:

$$B = B_0 + (r.\nabla)B + ... \\ B_z = B_0 + y(\partial B_z / \partial y) + ... \quad (2)$$

The magnetic field lines are often called "lines of force". They are not lines force. The misnomer is perpetuated here to prepare the student for the treacheries of his profession.This expansion of course requires $r_L/L<<1$, where L is the scale length of $\partial B_z / \partial y$ The first term of equation (1) averages to zero in a gyration, and the average of $\cos^2 \omega_c t$ is 1/2 so that.

$$\overline{F}_y = \mp qv_\perp r_L \frac{1}{2}(\partial B / \partial y) \quad (3)$$

The guiding center drift velocity is then:

$$v_{gc} = \frac{1}{q}\frac{F \times B}{B^2} = \frac{1}{q}\frac{\overline{F}_y}{|B|}\hat{x} = \\ = \mp\frac{v_\perp r_L}{B}\frac{1}{2}\frac{\partial B}{\partial y}\hat{x} \tag{4}$$

Since the choice of the y axis was arbitrary, this can be generalized to:

$$v_{\nabla B} = \pm\frac{1}{2}v_\perp r_L \frac{B \times \nabla B}{B^2} \tag{5}$$

This has all the dependences, which can be expected from the physical picture; only the factor ½ (arising from the averaging) was not predicted. Note that the $\pm$ stands for the sign of the charge, and the lightface B stands for |B|. the quantity is called the grad-B drift; it is in opposite directions for ions and electrons and causes a current transverse to B. An exact calculation of $v_{\nabla B}$ would require using the exact orbit, including the drift, in the averaging process.

2. MOVEMENT OF IONS UNDER MAGNETIC FIELD WITH CURVED LINES AND INVARIANT VALUE OF MAGNETIC INDUCTION B (CURVATIVE DRIFT)

In this case the lines of force to be curved with a constant radius of curvature R_c and

|B| =const (Fig. 2). Such a field does not obey Maxwell's equations in a vacuum, so in practicle the grad- B drift will always be added to the effect derived here. A guiding center drifts aries from the centrifugal force felt by the particles as they move along the field lines in their thermal motion. If $v_\parallel^2$ denotes the average square of the component of random velocity along B, the average centrifugal force is :

$$F_{cf} = \frac{mv_\parallel^2}{R_c}\hat{r} = mv_\parallel^2\frac{R_c}{R_c^2} \tag{6}$$

This gives rise to a drift :

$$v_R = \frac{1}{q}\frac{F_{cf} \times B}{B^2} = \frac{mv_\parallel^2}{qB^2}\frac{R_c \times B}{R_c^2} \tag{7}$$

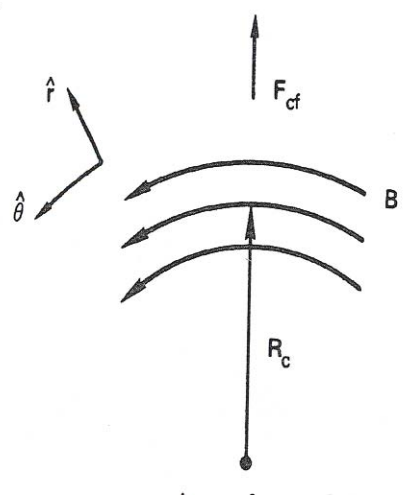

Fig. 2. A curved magnetic field

The drift v_R is called the curvature drift.

It's necessary to complete the grad-B drift which accompanies this when the decrease of |B| with radius is taken into account. In a vacuum $\nabla \times B = 0$ .In the cylindrical coordninates of Fig. 2 has only a z component, since B only a θ component and ∇B only an r component. Therefore:

$$(\nabla \times B)_z = \frac{1}{r}\frac{\partial}{\partial r}(rB_0) = 0$$

$$B_\theta \propto \frac{1}{r} \tag{8}$$

Thus

$$|B| = \propto \frac{1}{R_c} \qquad \frac{\nabla|B|}{|B|} = -\frac{R_c}{R_c^2} \tag{9}$$

Using equation (5):

$$v_{\nabla B} = \mp\frac{1}{2}\frac{v_\perp r_L}{B^2}B \times |B|\frac{R_c}{R_c^2} = \\ = \pm\frac{1}{2}\frac{v_\perp^2}{\omega_c}\frac{R_c \times B}{R_c^2 B} = \frac{1}{2}\frac{m}{q}v_\perp^2\frac{R_c \times B}{R_c^2 B^2} \tag{10}$$

Adding this to v_r , it's possible to obtain the total drift in a curved vacuum field:

$$v_r + v_{\nabla B} = \frac{m}{q}\frac{R_c \times B}{R_c^2 B^2}\left(v_\parallel^2 + \frac{1}{2}v_\perp^2\right) \tag{11}$$

It is unfortunate that these drifts add. For a Maxwellian distributional, indicate that $\bar{v}_{\|}^2$ and $\frac{1}{2}\bar{v}_{\perp}^2$ are each equal to KT/m since v involves two degrees of freedom. Therefore:

$$\bar{v}_R + \nabla B = \pm\frac{v_{th}^2}{R_c\omega_c}\hat{y} = \pm\frac{\bar{r}_L}{R_c}v_{th}\hat{y} \qquad (12)$$

Where: $\hat{y}$ here is the direction $R_c \times B$.

This shows that $\bar{v}_R + \nabla B$ depends on the charge of the species but not on its mass.

3. MOVEMENT OF IONS UNDER MAGNETIC FIELD B||B: MAGNETIC MIRRORS

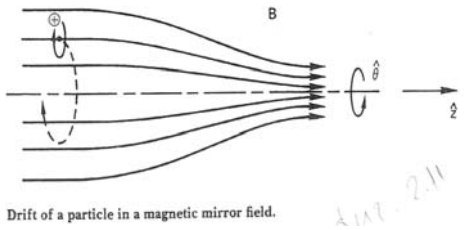

Fig. 3. Drift of a particle in a magnetic mirror field

This is a magnetic field which is pointed primarily in the z direction and whose magnitude varies in the z direction. Let the field be axisymmetric, with $B_\theta = 0$ and $\partial/\partial\theta = 0$. Since the lines of force converge and diverge, there is necessarily a component B_r (Fig. 3). We wish to show that this gives rise to a force, which can trap a particle in a magnetic field. It's possible to obtain B_r from $\nabla.B = 0$:

$$\frac{1}{r}\frac{\partial}{\partial r}\left(rB_r\right) + \frac{\partial B_z}{\partial z} = 0 \qquad (13)$$

If $\partial B_z/\partial_z$ is given at r=0 and does not vary much with r, it's possible to have approximately

$$rB_r = -\int_0^r r\frac{\partial B_z}{\partial z}dr \cong -\frac{1}{2}r^2\left[\frac{\partial B_z}{\partial z}\right]_{r=0} \qquad (14)$$

The various of |B| with r causes a grad- B drift of guiding centers about the axis of symmetry, but there is no radial grad-B drift, because $\partial B/\partial\theta = 0$. The components of the Lorenz force are:

$$\begin{aligned} F_r &= q\left(v_\theta B_z - v_z B_\theta\right) \\ F_\theta &= q\left(-v_r B_z + v_z B_r\right) \\ F_z &= q\left(v_r B_\theta - v_\theta B_r\right) \end{aligned} \qquad (15)$$

Two terms vanish if $B_\theta = 0$ and terms 1 and 2 give rise to the usual Larmor gyration. Term 3 vanishes on the axis; when it does not vanish, the azimuthal force causes a drift in the radial direction. This drift merely makes the guiding centers follow the lines of force. Term 4 is the one we are interested in. Using equation (14), it's possible to obtain:

$$F_z = \frac{1}{2}qv_\theta r\left(\partial B_z/\partial z\right) \qquad (16)$$

It's necessary to average over one gyration. For simplicity, consider a particle whose guiding center lies on the axis. Then v_θ is a constant during a gyration; depending on the sign of q, v_θ is $\mp v_\perp$

Since $r = r_L$ the average force is

$$\begin{aligned} \bar{F}_z &= \mp\frac{1}{2}qv_\perp r_L\frac{\partial B_z}{\partial z} = \\ &= \mp\frac{1}{2}q\frac{v_\perp^2}{\omega_c}\frac{\partial B_z}{\partial z} = -\frac{1}{2}\frac{mv_\perp^2}{B}\frac{\partial B_z}{\partial z} \end{aligned} \qquad (17)$$

The magnetic moment of the gyrating particle to be:

$$\mu \equiv \frac{1}{2}mv_\perp^2/B \qquad (18)$$

CONCLUSION

1. A mathematical analysis of movement of ions in alive tissues under non uniform magnetic field created by apparatus for magnetotherapy is described in the paper.

2. The trajectories of movement of ions have been obtained.

3. An analysis of connection between parameters of ion's trajectories and masse of ions, electrical charge of ions, magnetic induction have been obtained.

References

[1] S.K. Lodha, J.C. Renteria, and K.M. Roskin, Topology preserving compression of 2D vector fields, In *Visualization 2000*, pages 343-350, October 2000, Topology Preserving Compression.

[2] Bronsvoort, W.F., F.W. Jansen, F.H. Post (1991) Design and Display of Solid Models, In *Advances in Computer Graphics VI*, G. Garcia, I. Herman (eds.), Springer Verlag, pp. 1-57

[3] Kaufman, A., R. Yagel, D. Cohen (1990) Intermixing Surface and Volume Rendering, In *3D Imaging in Medicine: Algorithms, Systems, Applications*, K.H. Höhne, H. Fuchs, S.M. Pizer (eds.), Springer Verlag, pp. 217-227

[4] Kroos, K.A.(1984) Computer Graphics Flow Visualization Techniques for Three-Dimensional Flow Visualization, In *Frontiers in Computer Graphics*, T.L. Kunii (ed.), Springer Verlag, pp. 129-145

[5] Wijk, J.J. van (1990b) A Raster Graphics Approach to Flow Visualization, In *Eurographics '90* , C.E. Vandoni, D.A. Duce (eds.), pp. 251-259

[6] Schroeder, W.J., C.R. Volpe, W.E. Lorensen (1991) The Stream Polygon: a Technique for 3D Vector Field Visualization, In *Proceedings Visualization '91*, G.M. Nielson, L. Rosenblum (eds.), IEEE Computer Society Press, pp. 126-132.

AUTHOR INDEX